HELLENIC REPUBLIC
UNIVERSITY OF IOANNINA
SCHOOL OF SCIENCES
DEPARTMENT OF MATERIALS SCIENCE AND ENGINEERING

Ionic Liquid modified porous materials & membranes for gas separation applications

OLGA VANGELI

Ph.D. thesis

Ioannina, 2013

HELLENIC REPUBLIC
UNIVERSITY OF IOANNINA
SCHOOL OF SCIENCES
DEPARTMENT OF MATERIALS SCIENCE AND ENGINEERING

Ionic Liquid modified porous materials & membranes for gas separation applications

OLGA VANGELI

Ph.D. thesis

Ioannina, 2013

<< Η έγκριση της διδακτορικής διατριβής από το Τμήμα Μηχανικών Επιστήμης Υλικών της Σχολής Θετικών Επιστημών του Πανεπιστημίου Ιωαννίνων δεν υποδηλώνει αποδοχή των γνωμών του συγγραφέα Ν. 5343/32, άρθρο 202, παράγραφος 2>>.

Ημερομηνία αίτησης της κ. Όλγας Βαγγέλης: 30.06.2008

Ημερομηνία ορισμού Τριμελούς Συμβουλευτικής Επιτροπής: 26.09.2008

Μέλη Τριμελούς Συμβουλευτικής Επιτροπής:

Επιβλέπων

- Δημοσθένης Φωκάς, Επίκουρος Καθηγητής
  Μηχανικών Επιστήμης Υλικών, της Σ.Θ.Ε., Πανεπιστήμιο Ιωαννίνων

Μέλη

- Κωνσταντίνος Μπέλτσιος, Καθηγητής
  Μηχανικών Επιστήμης Υλικών, της Σ.Θ.Ε., Πανεπιστήμιο Ιωαννίνων
- Γεώργιος Ρωμανός, Ερευνητής Β’
  Ε.Κ.Ε.Φ.Ε Δημόκριτος

Ημερομηνία ορισμού θέματος: 26.09.2008

Ionic Liquid modified porous materials & membranes for gas separation applications

ΔΙΟΡΙΣΜΟΣ ΕΠΤΑΜΕΛΟΥΣ ΕΞΕΤΑΣΤΙΚΗΣ ΕΠΙΤΡΟΠΗΣ: 22.07.2013

- Δημοσθένης Φωκάς, Επίκουρος Καθηγητής
  Μηχανικών Επιστήμης Υλικών, της Σ.Θ.Ε., Πανεπιστήμιο Ιωαννίνων
- Κωνσταντίνος Μπέλτσιος, Καθηγητής
  Μηχανικών Επιστήμης Υλικών, της Σ.Θ.Ε., Πανεπιστήμιο Ιωαννίνων
- Γεώργιος Ρωμανός, Ερευνητής Β’
  Ε.Κ.Ε.Φ.Ε Δημόκριτος
- Μιχαήλ Καρακασίδης, Καθηγητής
  Μηχανικών Επιστήμης Υλικών, της Σ.Θ.Ε., Πανεπιστήμιο Ιωαννίνων
- Δημήτριος Γουρνής, Αναπληρωτής Καθηγητής
  Μηχανικών Επιστήμης Υλικών, της Σ.Θ.Ε., Πανεπιστήμιο Ιωαννίνων
- Δημήτριος Παπαγιάννης, Επίκουρος Καθηγητής
  Μηχανικών Επιστήμης Υλικών, της Σ.Θ.Ε., Πανεπιστήμιο Ιωαννίνων
- Φώτης Κατσαρός, Ερευνητής Β’
  Ε.Κ.Ε.Φ.Ε Δημόκριτος

Έγκριση Διδακτορικής Διατριβής με βαθμό << **ΑΡΙΣΤΑ**>> στις 13.12.2013

Ο Πρόεδρος του Τμήματος	**Η Γραμματέας του Τμήματος**
Καρακασίδης Μιχαήλ **Καθηγητής**	**Ξανθή Τουτουνζόγλου**

Acknowledgment

I would like to express my gratitude to Dr G. Romanos, Ass. Prof. D. Fokas, Prof. K. Beltsios, Dr. N. Kanellopoulos for their contribution to the fulfillment of this thesis.

O. Vangeli

SUMMARY

Ionic liquids (ILs), due to their unique chemical and thermophysical properties, are the subject of a large number of the currently conducted research studies, and embody the potential of several interesting applications. Their unique properties (i.e. the negligible vapor pressure, thermal stability, unique solvation, good ion conductivity, catalytic activity and selectivity performance) have rendered them excellent candidates as extraction media, solvents for organic/organometallic synthesis and catalysis, electrolytes, supports for the immobilization of enzymes and as solvents for gas separation and purification technologies.

Supported ionic liquid phase (SILP) systems have lately attracted a great deal of attention because of their potential to circumvent two major problems, namely:

1) the large quantity of ionic liquid usually needed to render viable a catalytic or separation process, which increases the cost of the application due to the high price of the ionic liquid solvents

2) the high viscosity of ionic liquids inducing mass transfer limitations which are more pronounced in the case of fast chemical reactions. In these cases, the reaction takes place only within the narrow diffusion layer and not in the bulk of the ionic liquid catalyst solution.

Lately, research efforts were focused on the development of supported Ionic Liquid (IL) catalysts and adsorbents as well as on the development of supported IL membranes for gas separation and heterogeneous catalysis applications. In most of these cases, ILs are deposited as thin layers on the external surface of non porous supports or introduced into the pores of porous powders and membranes via a physical imbibition method by just mixing the powder with a solution of the IL or the IL directly with the powder and the membrane. Although these procedures have resulted in the SILP and SILM materials with outstanding gas separation properties, there are not any references concerning their stability and reproducibility according to our knowledge. Especially, there is a lack of investigations related to their application at elevated temperature and pressure conditions that are usually applied in a membrane under Pressure Swing Adsorption technologies. For this reason, our research work was mainly directed towards the elucidation of chemical paths for the

stabilization of the IL into the pore structure via covalent bonding with the active groups of the pore surface.

In this regard, we have extensively studied the case of grafting the IL onto the pore surface of siliceous supports through the use of a silane functionality. First, investigations included the elucidation of the effect of several parameters to the overall material development procedure such as the activity of the pore surface, the polarity and water content of the solvents as well as the pore network structure of the porous support. For this reason, we have initially used a typical and not expensive siliceous support like porous glass (Vycor) in order to address the development of highly CO_2 separating SILPS, utilizing ordered mesoporous silicas like MCM-41 and SBA-15.

More specific hybrid materials were prepared by immobilizing ionic liquid (IL), based on grafting methylimidazolium cation on the internal surface of porous Vycor®. The extent of the initial silane grafting, expressed as the fraction of the occupied Vycor® silanol groups, was determined by the analysis of water vapor adsorption-desorption isotherms. Chloroform was shown to be the most appropriate solvent, giving silanol occupation degree of the order of 80%. Moreover, the pretreatment of Vycor® at 430K under high vacuum conditions, enhanced the monolayer grafting presumably due to the prevention of silane polymerization on the Vycor® surface, thus expanding the degree of chloroform coverage up to 96% . Combination of nitrogen physisorption with SAXS led to the elucidation of the morphology of the internal surface after grafting. It was concluded that the adsorbed water on the Vycor® surface, in combination with the presence of residual water in the solvent, facilitated the formation of bulky but not continuous organosilane entities, which were generated by the silane polymerization. The grafted samples were further treated with 1-methylimidazole at 358K for 48 hours following ion exchange with the PF_6^-. A new methodology was developed aiming at the determination of the w/w % percentage of IL loading on the grafted materials. The method is based on appropriate analysis of the transient data of CO_2 adsorption isotherms and the results were in good agreement with the analysis of the TGA measurements.

Supported ionic liquid phase systems (SILP) of high CO_2 separation performance, were prepared by immobilizing a methylimidazolium cation based ionic liquid onto the pore surface of Vycor® and of two types of MCM-41. The “grafting to” method was applied involving (3-Chloropropyl) trialkoxysilane anchoring on the supports’ silanol groups, followed by treatment with 1-methylimidazole and ion exchange with PF_6^-. Optimum surface pretreatment procedures and reaction conditions for enhanced ionic liquid (IL) loading were properly defined and applied for all modifications. A study on the effect of different pore size on the physical state of the grafted 1-(silylpropyl)-3-methylimidazolium-hexafluorophosphate [spmim][PF_6^-] was also conducted. The [spmim][PF_6^-] crystallinity under extreme confinement into the pores was investigated by modulated Differential Scanning Calorimetry and XRD and was further related to the capacity of the developed SILP to preferentially adsorb CO_2 over CO. On this purpose, CO_2 and CO absorption measurements of the bulk ionic liquid [bmim][PF_6^-] and the synthesized alkoxysilyl-IL were initially performed at several temperatures. The results showed an enhancement of the bulk IL performance to preferentially adsorb CO_2 at 273 K. The DSC analysis of the SILPs revealed transition of the melting point of the grafted alkoxysilyl-IL to higher temperatures when the support pore size was below 4 nm. The 2.3 nm-MCM-41 SILP system, exhibited infinite CO_2/CO separation capacity at temperatures below and above the melting point of the bulk IL phase, adsorbing in parallel significant amounts of CO_2 in a reversible manner. These properties make the developed material an excellent candidate for CO_2/CO separation with pressure swing adsorption (PSA) techniques.

Similar silane functionalised Ionic Liquids were synthesized for the development of the supported IL membranes. The stabilization of a room temperature methylimidazolium cation based ionic liquid (IL) into the pores of ceramic nanofiltration (NF) membranes, was achieved by means of a novel in-situ pressure assisted imbibition/reaction method. The complete coverage of the nanopores void space by the synthesized IL phase, introduced an additional parameter that was pursued in parallel. The purpose was to develop hybrid membranes that will solely exhibit the gas solvation/diffusion properties of the IL. A silane functionalized ionic liquid phase of 1-methyl-3-(1-trialkoxysilylmethyl) imidazolium as cation and hexafluorophosphate as anion, was first synthesized and subsequently grafted onto the pore surface. The CO_2/CO separation performance of the modified membranes was quite significant. The maximum CO_2/CO separation factors achieved were 11 at 30^{o}C, 25 at 50 ^{o}C, 12 at 100 ^{o}C and 5 at 230 ^{o}C. The respective CO_2 permeability values were 226, 520, 715 and 2000 Barrer. The stability of the developed membranes has been verified in 3 sequential cycles of heating/cooling, in temperatures ranging between 25 and 250 ^{o}C and a differential pressure up to 0.5 MPa.

ΠΕΡΙΛΗΨΗ

Τα ιοντικά υγρά είναι οργανικά άλατα που λόγω της ασυμμετρίας του κατιόντος ή του ανιόντος τους παραμένουν σε υγρή κατάσταση σε θερμοκρασία δωματίου. Τα τελευταία χρόνια διεξάγεται συστηματική έρευνα σε θέματα που αφορούν τόσο τη σύνθεση και καθαρότητα των ιοντικών υγρών όσο και την ανάπτυξη τεχνικών για τον χαρακτηρισμό των θερμοφυσικών τους ιδιοτήτων. Αυτό συμβαίνει λόγω των πολύ ενδιαφερουσών ιδιοτήτων τους που τα καθιστά υποψήφια για ευρύ φάσμα σημαντικών εφαρμογών από ενζυματικές και καταλυτικές αντιδράσεις έως ηλεκτρολύτες σε ηλιακές κυψελίδες και ροφητικά μέσα για διαχωρισμό αερίων. Τα ιοντικά υγρά παρουσιάζουν αμελητέα τάση ατμών, πολύ καλές διαλυτικές ικανότητες, υψηλή θερμική αντοχή, αγωγιμότητα, καταλυτικές ιδιότητες ενώ είναι εύκολο να αλλάξουν οι φυσικοχημικές και χημικές τους ιδιότητες προσθέτοντας συγκεκριμένες ομάδες στο κατιόν ή στο ανιόν.

Υβριδικά υλικά ιοντικών υγρών/πορωδών υλικών [Supported ionic liquid phase (SILP) systems] έχουν τραβήξει το ενδιαφέρον τα τελευταία χρόνια για δύο κυρίως λόγους:

Α) την μεγάλη ποσότητα των ιοντικών υγρών που απαιτούνται για καταλυτικές διεργασίες καθώς και για διεργασίες διαχωρισμού σε συνδυασμό με το υψηλό κόστος των ιοντικών υγρών.

Β) το μεγάλο ιξώδες που παρουσιάζουν τα ιοντικά υγρά δημιουργώντας προβλήματα μεταφοράς μάζας κυρίως σε διεργασίες με μεγάλη ταχύτητα αντίδρασης.

Τα υβριδικά αυτά συστήματα αναφέρονται στην βιβλιογραφία ως καταλύτες ή ροφητές υποστηριγμένου ιοντικού υγρού (Supported Ionic Liquid Catalysts and Systems-SILC and SILP) και ως μεμβράνες υποστηριγμένου ιοντικού υγρού (Supported Ionic Liquid Membranes SILM).

Ο συνήθης τρόπος για την ανάπτυξη τέτοιων συστημάτων είναι ο φυσικός εμποτισμός του πορώδους ή μη πορώδους μέσου με την χρήση ενός διαλύματος του ιοντικού υγρού. Μετά την απομάκρυνση του διαλύτη το ιοντικό υγρό είτε παγιδεύεται στους πόρους είτε καλύπτει πλήρως την εξωτερική επιφάνεια μη πορωδών μέσων.

Παρόλο που η διαδικασία αυτή έχει οδηγήσει σε υλικά με σημαντική απόδοση στον διαχωρισμό αερίων η εφαρμογή τους γίνεται εφικτή μόνο υπο συνθήκες, δηλαδή, χαμηλές διαφορές πίεσης και όχι υψηλές θερμοκρασίες. Και οι δύο αυτές προϋποθέσεις αντιβαίνουν στην συνήθη πρακτική εφαρμογής τεχνολογιών διαχωρισμού αερίων όπως οι τεχνολογίες μεμβρανών και η τεχνολογία ρόφησης μέσω ταλάντωσης πίεσης (pressure Swing Adsorption). Για το λόγο αυτό η έρευνα που πραγματοποιήθηκε στα πλαίσια της παρούσης διατριβής εστίασε κυρίως στον προσδιορισμό συνθετικών μονοπατιών για την σταθεροποίηση των ιοντικών υγρών υγρού και της επιφάνειας του πόρου.

Έτσι εξετάστηκε συστηματικά η περίπτωση χημικής πρόσδεσης του ιοντικού υγρού στους πόρους υλικών πυριτίας με την χρήση μιας λειτουργικής ομάδας αλκοξυσιλανίου. Αρχικά ερευνήθηκε η επίδραση παραμέτρων όπως η δραστικότητα της πορώδους επιφάνειας, η πολικότητα και περιεχόμενη υγρασία των διαλυτών σιλανοποίησης και η πολυπλοκότητα του πορώδους δικτύου στην απόδοση στην πορώδη δομή μέσω σχηματισμού ομοιοπολικού δεσμού μεταξύ του ιοντικού εναπόθεσης. Για την προκαταρκτική αυτή έρευνα χρησιμοποιήθηκε ένα σχετικά φτηνό υλικό όπως το πορώδες γυαλί τύπου Vycor. Στην συνέχεια για να αναπτυχθούν τα υλικά υψηλής απόδοσης σε διαχωρισμό αερίων και πιο συγκεκριμένα CO_2/CO, χρησιμοποιήθηκαν πιο προηγμένα πορώδη υποστρώματα όπως οι οργανωμένες μεσοπορώδεις πυριτίες τύπου MCM-41 και SBA-15.

Πιο συγκεκριμένα υβριδικά υλικά ιοντικών υγρών με Vycor® παρασκευάστηκαν με ομοιοπολική σύνδεση του 3-χλωροπροπυλοτριαλκοξυσιλανίου με τις υδροξυλομάδες της επιφάνειας του Vycor®. Το ποσοστό της σιλανοποίησης υπολογίστηκε με τη μέθοδο ρόφησης- εκρόφησης υδρατμών και έδωσε μέγιστη τιμή για τα δείγματα που παρασκευάστηκαν σε χλωροφόρμιο. Δείγματα που είχαν προεργαστεί στους 430K υπό υψηλό κενό έδωσαν μονοστοιβαδική επίστρωση του σιλανίου αποφεύγοντας τον πολυμερισμό και δίνοντας ποσοστό επικάλυψης σε χλωροφόρμιο μέχρι 96%.

Επιπλέον φυσική ρόφηση αζώτου σε συνδυασμό με μικρογωνιακή σκέδαση ακτίνων-X (SAXS) βοήθησαν να διευκρινιστεί η μορφολογία της εσωτερικής επιφάνειας μετά την ομοιοπολική σύνδεση του τριαλκοξυσιλανίου. Έτσι καταλήξαμε στο συμπέρασμα ότι η παρουσία υγρασίας στην επιφάνεια του Vycor® καθώς και στο διαλύτη της αντίδρασης οδηγούσε στη δημιουργία πολυμερισμένων οντοτήτων στην επιφάνεια. Στη συνέχεια τα δείγματα με το ομοιοπολικά συνδεδεμένο χλωροπροπυλοσιλάνιο υποβλήθηκαν σε αντίδραση με 1-μεθυλοιμιδαζόλιο στους 358K και για 48 ώρες ενώ την αντίδραση ακολούθησε ιονοανταλλαγή με το ανιόν PF_6^-.

Μια καινούργια μεθοδολογία αναπτύχθηκε για τον υπολογισμό του ιοντικού υγρού που είναι ομοιοπολικά συνδεδεμένο στην επιφάνεια του υποστρώματος. Η μέθοδος βασίζεται στην ανάλυση δεδομένων μεταβατικού σταδίου της ρόφησης του CO_2 και είναι σε καλή συμφωνία με μετρήσεις θερμοσταθμικής ανάλυσης (TGA).

Επιπλέον παρασκευάστηκαν υβριδικά υλικά ιοντικού υγρού με υπόστρωμα οργανωμένης μεσοπορώδους πυριτίας τύπου MCM-41 και SBA-15. Εφαρμόστηκε η μέθοδος «εναπόθεσης σε» (σταδιακή σύνθεση πάνω στο υπόστρωμα). 3-χλωροπροπυλοτριαλκοξυσιλάνιο συνδέθηκε ομοιοπολικά με τα υδροξύλια της επιφάνειας του υποστρώματος και στην συνέχεια αντέδρασε με 1-μεθυλοιμιδαζόλιο ακολουθούμενο από ιονοανταλλαγή με PF_6^-. Οι βέλτιστες συνθήκες όσον αφορά την επεξεργασία της επιφάνειας του υποστρώματος καθώς και τις συνθήκες αντίδρασης για την ομοιοπολική σύνδεση του ιοντικού υγρού προσδιορίστηκαν με μεθοδολογία αντίστοιχη με αυτή που εφαρμόστηκε στην πορώδη ύαλο. Επίσης έγινε μελέτη της επίδρασης των χαρακτηριστικών της πορώδους δομής στη φυσική κατάσταση του ομοιοπολικά συνδεδεμένου ιοντικού υγρού. Η κρυσταλλική κατάσταση του ιοντικού υγρού [spmim][PF_6^-] όταν βρίσκεται μέσα στην πορώδη δομή μελετήθηκε με θερμιδομετρία διαφορικής σάρωσης και XRD.

CO_2 και CO μετρήσεις ρόφησης του ιοντικού υγρού [bmim][PF_6^-] και του αλκοξυσίλυλο ιοντικού υγρού αρχικά πραγματοποιήθηκαν σε διάφορες θερμοκρασίες. Τα αποτελέσματα έδειξαν ανοδική τάση του ιοντικού υγρού να προσροφά CO_2 στους 273 K. Η ανάλυση θερμιδομετρίας διαφορικής σάρωσης (DSC) των υβριδικών υλικών έδειξε μετάβαση του σημείου τήξης του ομοιοπολικά συνδεδεμένου αλκοξυσίλυλο ιοντικού υγρού σε υψηλότερες θερμοκρασίες όταν το μέγεθος πόρων του υποστρώματος ήταν μικρότερο των 4nm. Τα 2.3nm-MCM-41 υβριδικά υλικά παρουσίασαν άπειρη διαχωριστική ικανότητα CO_2/CO σε θερμοκρασίες κάτω και πάνω από το σημείο τήξης του ομοιοπολικά συνδεδεμένου ιοντικού υγρού, προσροφώντας σημαντικές ποσότητες CO_2 κατά αντιστρεπτό τρόπο.

Αυτές οι ιδιότητες καθιστούν τα υλικά που παρασκευάστηκαν ιδανικά για τεχνικές προσρόφησης υπό πίεση.

Ομοιοπολική σύνδεση ενός ιοντικού υγρού βασιζόμενου σε μεθυλοιμιδαζολικό κατιόν, πραγματοποιήθηκε στους πόρους μεμβράνης νανοδιήθησης με τη μέθοδο εμποτισμού/αντίδρασης σε ατμόσφαιρα αζώτου και υπό υψηλή πίεση.

Παράλληλα με την ομοιοπολική σύνδεση επιδιώχθηκε και το πλήρες κλείσιμο των πόρων από το ιοντικό υγρό ώστε η υβριδική μεμβράνη να αποκτήσει πλήρως τις ιδιότητες διαλυτότητας/διάχυσης αερίου του καθαρού ιοντικού υγρού. Η διαχωριστική ικανότητα σε CO_2/CO της υβριδικής μεμβράνης ήταν αρκετά σημαντική. Η μέγιστη απόδοση διαχωρισμού CO_2/CO που επιτεύχθηκε ήταν 11 στους 30^{o}C, 25 στους 50^{o}C, 12 στους 100^{o}C και 5 στους 230^{o}C. Οι αντίστοιχες διαπερατότητες ήταν 226, 520, 715 και 2000 Barrer. Η σταθερότητα της υβριδικής μεμβράνης διαπιστώθηκε με τρεις διαδοχικούς κύκλους θέρμανσης/ψύξης σε εύρος θερμοκρασιών από 25 μέχρι 250^{o}C και διαφορική πίεση μέχρι 0.5 MPa.

Contents

1 INTRODUCTION

1.1 History of ionic liquids

Room Temperature Ionic Liquids (RTILs) are a unique class of salts with melting points at or below 100 °C. They resemble high-temperature molten metallic salts, such as sodium chloride, but they contain at least one organic ion (cation) that is relatively large and asymmetric compared to metallic ions[1] (Figure 1). The crystallization of ionic liquids is not favorable due to weak interactions between cations and anions, thus resulting in a substance that is in liquid state at room temperatures.[7]

common cations

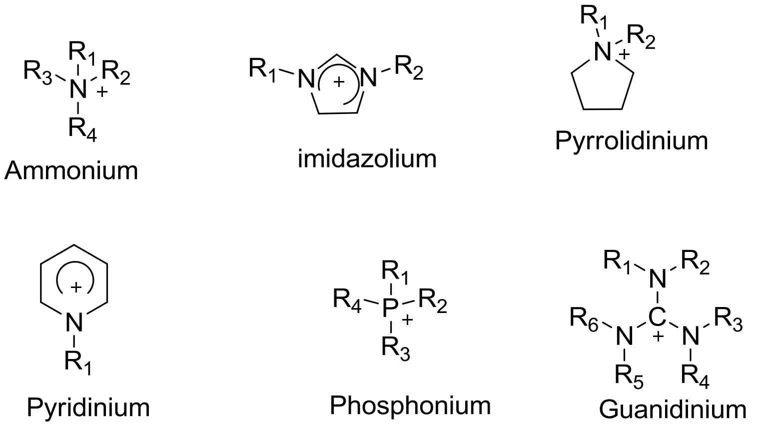

common anions

Chloride: Cl^-
Methylsulfate: $CH_3OSO_3^-$
Triflate: CF_3SO_3-
Trifluoroacete: $CF_3CO_2^-$
Hexafluorophospate: PF_6^-
Tetrafluoroborate: BF_4^-
Bis(trifluoromethanesulfonyl)imide: $N(CF_3SO_2)_2^-$
Dicyanamide: $N(CN)_2^-$

Figure 1. Most common cations and anions

In 1914, Walden[2] reported the first RTIL which was no other than ethylammonium nitrate. Ionic liquid research started in 1940s with the study of eutectic mixtures of N-alkyl-pyridinium halides with aluminum chloride or bromide for low temperature, highly conductive electrolytes in batteries.[3]

Wilkes and co-workers[4,5] reported in the early 1980s the first examples of ionic liquids based on dialkylimidazolium as a cation and chloroaluminate as an anion, exhibiting excellent catalytic properties for Friedel-Craft alkylation and acylation reactions.[5] Unfortunately, the chloroaluminate anion was found to react with water forming hydrogen chloride, thus leading the researchers to investigate for alternative cation-anion pairs where the anion is resistant to hydrolysis. In 1990s, anions such as tetrafluoroborate, hexafluorophoshate, nitrate, sulfate, acetate were introduced in ionic liquids.[6]

1.2 Properties of ionic liquids

One of the most important physical properties of ionic liquids is that they exhibit negligible vapor pressure[8], and do not tend to evaporate even when they are exposed to vacuum. In addition, most of them do not combust even when they are exposed to an open flame. The fact that ionic liquids are non-volatile and non flammable, renders them safer and more environmentally friendly solvents than the traditional volatile organic solvents.

Other properties of ionic liquids include good thermal stability, high ionic conductivity and a wide electrochemical window representing high stability towards oxidation and reduction reactions.[9]

Furthermore, ionic liquids have very good solvency power for both organic and inorganic materials, polar and non-polar, which makes them suitable for catalysis.[10,11] By varying the nature of the cation and anion, it is feasible to fine-tune the physicochemical properties of ionic liquids and generate task-specific ionic liquids.[7]

1.3 Applications of ionic liquids

Due to their properties such as negligible vapor pressure, thermal stability, unique solvation, good ion conductivity, catalytic activity and selectivity performance, ionic liquids exhibit a wide spectrum of applications. They were initially used as low temperature water-free electrolytes showing similar electrochemical windows to the conventional systems possessing an increased safety profile due to their lower toxicity and flammability.[12]

During the last decade, ionic liquids were found to be suitable solvents for chemical reactions since they combine excellent thermal and chemical stability with good and tunable solubility and catalytic properties.[10,11] One of the most studied reactions in ionic liquids is the Pd catalyzed Heck reaction.[13] Other examples of transition metal catalyzed reactions in ionic liquids are hydrogenations, hydroformylations, oxidations and dimerization and oligomerization reactions.[10,11,14-16]

Potential applications of ionic liquids in biotechnology can be divided in two main branches: enzymatic and whole-cell processes. The former applications are the most abundant in the literature,[17] with a wide variety of enzymes being capable of performing catalytic activities. The activities of these enzymes in ionic liquids was found to be comparable to or even higher than those observed in conventional organic solvents. The latter applications are still restricted to microorganisms able to tolerate the presence of ionic liquids. In addition, due to their unique solvation properties, ionic liquids have been studied lately as materials for gas separation and purification technologies.[36-39]

The following schematic (Figure 2) provides detailed information on the current applications of ionic liquids and the state of deployment (research and development, pilot, commercialization) for each application.

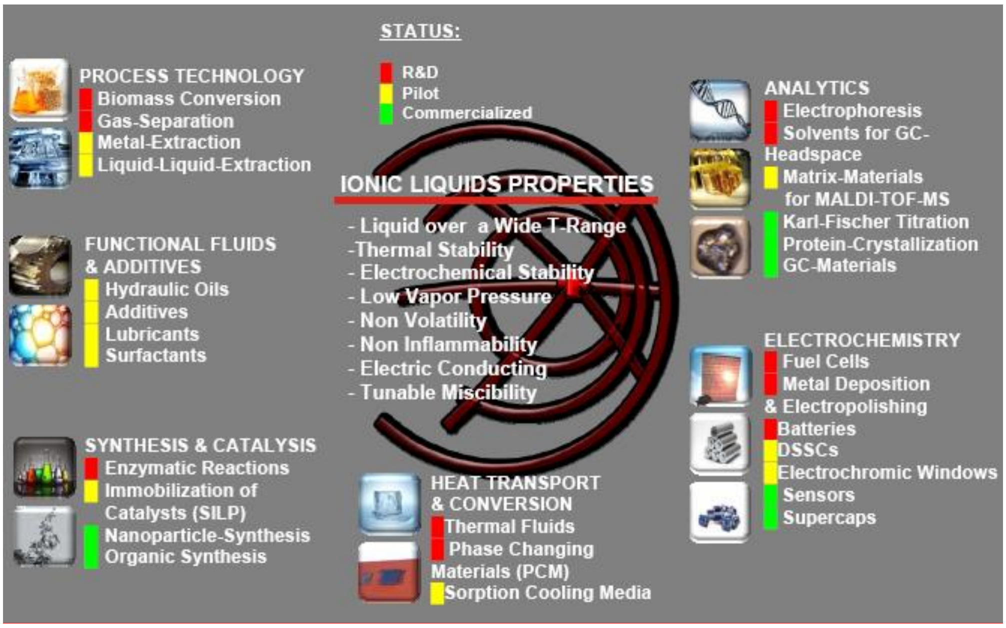

Figure 2. Ionic Liquids: An overview of applications

1.3.1 CO_2 capture/separation

Room Temperature Ionic Liquids (RTILs) have received increasing interest in applications involving CO_2 separations, due to the large solubility of CO_2 in selected

RTILs. In Table 1, Henry's constants for various gases in different solvents are provided.[18] Depending on their selectivity, ILs are stronger candidates for CO_2 capture. The solubility of CO_2, ethylene, ethane, methane, argon, oxygen, carbon monoxide, hydrogen and nitrogen in 1-*n*-butyl-3-methylimidazolium hexafluorophosphate ([bmim][PF_6]) in a temperature range between 10 and 50 ˚C and pressures up to 13 bar, proves the superiority of IL over various organic solvents like heptane, cyclohexane, benzene, ethanol and acetone (see Table1). The relatively higher solubility of CO_2 may be attributed to its quadrapole moment and dispersion forces.

The nature of anion seems to have a stronger influence on gas solubility than that of the cation. Ionic liquids possessing [Tf_2N] anion show higher CO_2 solubility among imidazolium-based RTILs.[19] The equilibrium pressure not only depends on temperature but also on CO_2 concentration. At 60 bar, CO_2 solubility in 1-ethyl-3-methylimidazolium bis[trifluoromethylsulfonyl]imide ([emim][Tf_2N]) is found to be 60 mol% which proves the higher efficiency of this IL for CO_2 capture. When compared with 1-ethyl-3-methylimidazolium hexafluorophosphate ([emim][PF_6]), the gas is found more soluble in the IL with the [Tf_2N]anion. Such data is confirming the effect of anion on CO_2 interaction with IL.[20] The fluoroalkyl group enhances the CO_2 solubility, thus making [emim][Tf_2N] more efficient for CO_2 capture.

Table 1. Henry's constants (bar, at 25 ˚C) for gases in different organic solvents

	[bmim][PF_6^-]	Heptane	Cyclohexane	Benzene	Ethanol	Acetone
CO_2	53.4	84.3	133.3	104.1	159.2	54.7
C_2H_4	173	44.2b	-	82.2	166.0	92.9
C_2H_6	355	31.7	43.0	68.1	148.2	105.2
CH_4	1690	293.4	309.4	487.8	791.6	552.2
O_2	8000	467.8	811.9	1241.0	1734.7	1208.7
Ar	8000	407.4	684.6	1149.5	1626.1	1117.5
CO	Nondetect	587.7	1022.5	1516.8	2092.2	1312.7
N_2	Nondetect	748.3	1331.5	2271.4	2820.1	1878.1
H_2	Nondetect	1477.3	2446.3	3927.3	4902.0	3382.0

A number of factors like free volume, size of the counterion, and strength of cation–anion interactions within the ionic liquid structure seem to govern CO_2 solubility in RTILs.

The CO_2 capture ability can be enhanced by introducing basic functional groups, like amino-groups, in the ILs. The functionalized in this way ILs are called Task Specific Ionic Liquids (TSILs). CO_2 absorption ability of TSILs can reach up to three fold of the corresponding RTILs. The enhanced effect of pressure in the case of TSILs was observed due to a steady increase in gas load with rise in pressure, providing evidence for both chemical as well as physical sorption.[21] Drawbacks for the use of TSILs in CO_2 capture, is their extremely high viscosity ($\geq$2000 mPa s) which causes mass transfer problems, the much longer equilibrium time required and the exceptionally long regeneration time ($\geq$ 24h).[22-24a] The general practice of tethering an alkylamine group on the imidazolium ring is lately avoided due to the formation of hydrogen bonding between the imidazolium C2-hydrogen and the anions of the IL that may lead to increased viscosity.

Lately, amine group tethering on the anion, especially through the use of amino acids as anions, has been proved a feasible way to overcome the problem of high viscosity.[24b] Amino acid anions combined with the phosphonium and alkylammonium based families of cations, exhibit low viscosities (below the 400 mPa s level) and very high CO_2 capture capacities (close to 1 mol/mol) at room temperature and pressures below 1 bar. However, the chemical capture mechanism and the formation of carbamic acid or carbamates leads to tremendous increase of the viscosity (250 fold) during the CO_2 capture, constituting unfeasible the application of these ILs in industrial scale CO_2 scrubbing processes. Dilution in water and the use of ILs in mixtures with amines are the possibilities currently investigated in order to confront this problem. Moreover, the development of supported ionic liquid phase systems is an alternative strategy to overcome the problems of high viscosity and slow diffusivity.

In this regard, a number of studies have been performed to explore the prospects of supported ionic liquid membranes (SILMs) involving RTILs or TSILs or both in CO_2 capture. The RTIL [bmim][Tf_2N], supported on porous alumina membrane, revealed very optimistic results in favor of CO_2 capture ability.[25] The SILM with [bmim][Tf_2N] showed higher selectivity of 127 (CO_2/N_2) than 72 with [C_8F_{13}mim][Tf_2N]. Also, the fluorinated ionic liquid is much more viscous than [bmim][Tf_2N] causing a decrease in CO_2 diffusivity.

In an other study,[26,27] [bmim][BF_4] was adsorbed on to polyvinylidene fluoride (PVDF) polymeric membrane. With the increase of IL content, the permeability coefficient was seen to increase abruptly. Through optimization of operating conditions, a selectivity of 25–45 (CO_2/CH_4) was achieved.

One of the negative aspects of SILMs is the leaching of the liquid through membrane pores as the pressure drops, surpassing the liquid stabilizing forces within the matrix. Polymerized ionic liquid membranes have been lately under study where CO_2 absorption experiments demonstrate their superiority over RTILs.[28] In contrast to RTILs, the poly(ionic liquids) with PF_6^- show higher efficiency as compared to BF_4^- or Tf_2N^- anions. Unfortunately, like polymeric membranes they suffer of plasticization induced selectivity losses, thus limiting their performances to low pressures.[29] In membrane studies, plasticization is generally defined as an increase in the segmental motion of polymer chains, due to the presence of one or more sorbates, such that the permeability of both components increases and the selectivity decreases.[30] Permeation of strongly plasticizing penetrant molecules (e.g. CO_2) through the polymer cause changes in the packing of the polymer chains in the polymer matrix due to swelling. This can induce significant polymer network dilation resulting in increased permeability values for the other components in the feed mixture. Studies for CO_2/CH_4 separation[29] with poly(RTILs) showed that CO_2 is an equally strong plasticizer in single gas as well as mixed gas experiments: the permeability of CO_2 increases by more than 60% over a pressure range of 40 bar. Methane does not plasticize the poly(RTIL) by itself in single gas experiments, however the presence of CO_2 accelerates its transport by more than 250%.

1.3.1.1 State of the art

At present, there are a number of absorption solvents commercially available for CO_2 capture. They are classified into two categories, chemical and physical solvents. The chemical solvents are commonly used for treating gas streams with low and moderate CO_2 partial pressure, while the physical solvents are suitable for high-pressure gas streams. The typical chemical solvents are alkanolamines, which are commonly used in the form of aqueous solutions. These chemical solvents include monoethanolamine (MEA), diethanolamine (DEA), N-methyldietha-nolamine (MDEA), diglycolamine

(DGA), diisopropanolamine (DIPA), and 2-amino-2-methyl-1-propanol (AMP). Today, the main implications in using the chemical sorption technology with amines arise because of the volatile character of amines and their corrosiveness and fast degradation rates by impurities present in the flue gas such as SO_x and O_2. It is estimated that the amount of degraded amine that is replaced per year for a 400 MW plant, can be up to 690 tones. Given the current price of 2 €/kg of MEA, a total cost of 1.4 M € is calculated. On the other hand, the annual emission of amines to the air (due to slippage) for a 400 MW plant can vary from 40-160 tones. Also, some of the emitted amines are proved to be toxic for the air and marine environment and even carcinogenic, especially the degradation byproducts like nitrosamines. Finally, the corrosiveness of amines requires high dilution in water and consequently enormous scrubbing/stripping towers to increase the gas/liquid contact time. This further leads to high capital costs and the need of high amount of water vapor to the stripper (for regeneration). Thus, the parasitic energy loss is enhanced constituting the overall process economically infeasible.

A promising alternative to chemical absorption using solvents such as MEA is the use of physical solvents in which the solvent selectively binds CO_2 at high partial pressures and low temperatures Physical absorbents such as Selexol (a mix of dimethylethers of polyethylene glycol) and Rectisol (methanol chilled to -40 ^{o}C), for example, have been used industrially for 40 years for natural gas purification and the treatment of synthesis gas.[31] The advantage in this case is the lower heat consumption in the solvent regeneration step.

Metal oxides (such as CaO and MgO) are promising capture materials given their ability to retain high adsorption capacities at temperatures above 300 ^{o}C.[32] The operation of the materials can be defined by a carbonation–calcinations cycle: the carbonation reaction of CO_2 with solid CaO at 600–650 ^{o}C precipitates calcium carbonate ($CaCO_3$), while the reverse calcination reaction regenerates the oxide at 800–850 ^{o}C.

On the other hand, Zeolites are amongst the most widely reported physical adsorbents for CO_2 capture in the patent and journal literature.[33] They constitute the primary adsorption material for commercial hydrogen production (involving H_2/CO_2

separation) using pressure swing adsorption, with the most popular of these based on zeolite 13X.[34] Zeolites are typically employed at elevated pressures (above 2 bar), and their adsorption capacity has been shown to be greatly reduced by the presence of moisture in the gas, thereby necessitating very high regeneration temperatures (often in excess of 300 ^{o}C).[35] Therefore these additional recovery costs for their regeneration pose a significant disadvantage.

1.4 Scope of the thesis

The aim of this thesis was to synthesize with the “grafting to” and “grafting from” method Supported Ionic Liquid Phases (SILP) and membranes (SILM) respectively for CO_2 capture and separation applications. Hybrid materials were fully characterized by means of pore morphology, their physicochemical and thermodynamic properties as well as gas adsorption capacity. Furthermore, an effort was made to relate the physicochemical and thermophysical properties of the deposited IL phase to the surface properties and pore structure characteristics of the several supports applied.

The performance of the developed materials was investigated with regards to their gas diffusion rates and permeability factors as well as their CO_2/CO separation capacity, which is of great importance in the production of synthesis gas. CO_2 is a desirable feed to the reformer (or gasifier) reducing methane consumption and producing syngas with an optimum H_2/CO ratio. However it can also be found in the reformer/gasifier discharge stream where it is undesirable and must be separated and recycled back to the feed.

1.4.1 Beyond the state of the art

As concluded from sections 1.3.1 and 1.3.1.1, RTILs can play a crucial role in replacing amines in the CO_2 capture and separation processes. For this reason Task Specific Ionic Liquids (TSIL) should be modeled and checked concerning their captured ability for CO_2 and their separation efficiency to various gases including CO.

Supported Ionic Liquid Phases (SILP) and Membranes (SILM) have been prepared so far by impregnation of the ILs into the pores of the inorganic supports, thus limiting their applications to moderate pressures.

Moreover, Supported Ionic Liquid Membranes (SILM) can be prepared by covalent bonding of the ILs on the inorganic supports (preferably on ceramic nanofiltration membranes in order to avoid plasticizing that occurs in polymeric membranes), thus increasing the surface area of interaction as well as obtaining a broad spectrum of operations in high trans-membrane pressures.

2 THEORETICAL PART

2.1 Porous materials - Classification of Pore Sizes

Porous solids are classified according to their pore size distribution, as proposed by Dubinin, in three classes:

a) microporous for pore widths below ~ 20 Å
b) transitional (or intermediate) for pore widths between ~20 Å and ~ 200 Å
c) macroporous for pore widths above ~ 200 Å

2.1.1 MCM-41

The most striking fact about the material MCM-41 is that, although composed of amorphous silica, it displays an ordered structure with uniform mesopores arranged into a hexagonal, honeycomb-like lattice.[40-43] A nice example of this structure can be seen in Figure 3. In this figure, one looks directly inside the uniform mesopores which are separated from each other by thin walls of amorphous silica, approximately 1 - 1.5 nm thick. MCM-41 displays a very large specific surface area of approximately 1,000 $m^2 g^{-1}$.

MCM-41 can be synthesized following a wide variety of preparation procedures. However, there is one thing all these procedures have in common next to the obvious presence of a source of silica, a templating agent. A *template* is a structure-directing agent which is usually a relatively simple molecule or ion, around which a framework is built up. The most common templates are quaternary ammonium ions with short alkyl chains, which are used for the synthesis of a large number of zeolites. For the synthesis of MCM-41, similar quaternary ammonium ions are frequently used with one important modification: at least one of the short alkyl chains is replaced by a long alkyl chain, generally a hexadecyl group.

This slight modification has an enormous impact on the behavior of the template in aqueous solutions. Due to the large hydrophobic alkyl chain, the template ions will aggregate together in order to minimize energetically unfavorable interactions of the non-polar alkyl chains with the very polar water solvent molecules. Although unfavorable from an entropic point of view, this is exactly the same behavior as displayed by soaps upon dissolution in water. The resulting aggregates of ions are denoted as *micelles*. It follows that these micelles have a hydrophobic core, containing the large alkyl chains, and a hydrophilic surface due to the ionic character of the ammonium head groups.

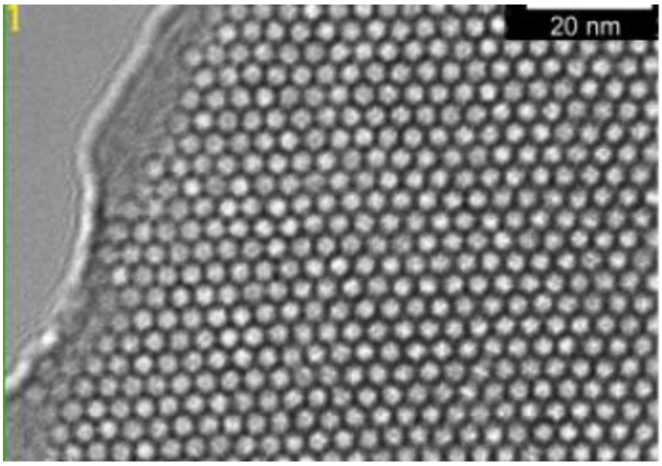

Figure 3. TEM micrograph of MCM-41, allowing the viewer to look directly inside the mesopores. The mesopores are arranged in a honeycomb-like structure, separated by thin, amorphous silica pore walls (black). The pore size of this MCM-41 material is approximately 3nm in diameter.

It is observed that at increasing amounts of template in water, different micelle geometry evolves: the spherical micelles gradually transform into long tubes, often denoted as rod-like micelles. Increasing the template concentration even further, results in aggregation of the rod-like micelles into a hexagonal *liquid crystalline structure*, resembling the MCM-41 structure. If the template concentration is increased further, this hexagonal liquid crystalline phase first transforms into a cubic liquid crystalline phase and eventually, at the highest template concentrations, into a lamellar liquid crystalline phase. The cubic liquid crystalline phase resembles the structure of mesoporous MCM-48, whereas the lamellar phase is the structural analogue of MCM-50 (an unstable material which consists of platelets of amorphous silica). During the synthesis of MCM-41, the electrostatic repulsions decrease as a result of the formation of a monolayer of silica around the micelles, thereby facilitating the subsequent aggregation of the micelles into close-packed hexagonal structures.

Next to a structure-directing agent and water as a solvent, two more ingredients are required for the synthesis of MCM-41: a source of silica and a mineralizing agent. Various sources of silica can be used for synthesis, water glass, amorphous silica and Kanemite (a layered silicate structure consisting of anionic silica sheets with chargecompensating sodium ions present in the interlayers). Furthermore, organic silicon alcoxides are also used frequently. For the dissolution of the various silica sources, a so-called "mineralizing agent" is used. For this purpose, sodium hydroxide or a concentrated ammonia solution are frequently employed, in addition to HF which can also find application despite the hazards associated with its use. Upon dissolution of silica by the mineralizing agent, small silicon oxy-anions are produced. In the presence of the rod-like template micelles, the silicate anions diffuse towards the surfaces of the micelles as a result of electrostatic attractions. Therefore, the concentration of silicate anions at the surface of the micelles rapidly increases with an increase of the electrostatic repulsions between the individual silicate ions. In order to alleviate these repulsive interactions, the silicate ions start to condense with each other, thereby forming a monolayer of amorphous silica around the micelles. Charge compensation of the ionic headgroups of the template is still brought about by deprotonated silanol groups of the silica monolayer. At this stage, the silica "coated" micelles can start to cluster together by condensation reactions between the silica layers of individual micelles, thus generating the MCM-41 framework. As a result of these processes, the pore walls of MCM-41 are amorphous and only 2-3 monolayers thick.[44] The processes described above can take place over a wide range of synthesis conditions, including gel composition, pH, timescale, temperature and pressure. However, once MCM-41 has been formed, its pores are filled with template and the micelles must be removed in order to obtain a completely mesoporous support material. The most elegant solution to this task, is removal by means of repeated washing with slightly acidified mixtures of an organic solvent and water, resulting in extraction of the template. The resulting solutions containing the template, can be evaporated to dryness and lead to the recovery of the template. Mild synthesis conditions may enable the recycling of the template and subsequently its use in a next synthesis cycle. A simpler method for template removal is calcination. During this process, the template is decomposed into CO_2, some NO_x and water vapors. Although MCM-41 is unstable with respect to steam, the quantities of steam produced during this process are too small to do any damage to the MCM-41 framework structure. Some modifications to the synthesis procedure described above are possible. The first possibility is the incorporation of hetero-elements inside the pore walls of the MCM-41 structure. The most frequently incorporated elements are aluminium and titanium. The presence of aluminium inside the pore walls generates an excess negative framework charge (as in zeolites and amorphous silica-aluminas). When protons compensate this charge, the resulting material is weakly Brønsted acidic. Compared to all-silica MCM-41, the physical properties of materials containing aluminium are generally a bit less well developed and dealumination can take place during template removal (especially in the presence of steam during calcination). Incorporation of titanium inside the pore walls, results in materials displaying interesting oxidation properties. A second adaptation that can be made to MCM-41 is "engineering" of the pore size. The most frequently used template for the synthesis of MCM-41 is hexadecyl (cetyl) trimethyl ammonium bromide (or chloride), *i.e.* a template with an alkyl chain containing sixteen - CH_2- moieties. This template yields MCM-41 with a uniform pore size of approximately 2.7 nm (*vide infra*). Using templates with longer or shorter alkyl chains, the pore size can be influenced. Nevertheless, due to the limited range of alkylammonium ions suitable for the preparation of MCM-41, the pore size can be adjusted to a small extent only. A more dramatic increase of pore size can be accomplished by the addition of so-called "auxiliary organics" to the synthesis gel, *e.g.* 1,3,5-trimethylbenzene (mesitylene). These organic molecules, which must be nonpolar, do not dissolve in water but instead they are absorbed in the hydrophobic core of the template micelles. Due to this absorption, the micelles swell and increase the average size of the mesopores in MCM-41 up to values of approximately 8-10 nm in diameter. Finally, it should be mentioned that a wide variety of preparation methods for MCM-41 have been reported, where details of the presented methods often dictate reproducibility and stability of the prepared MCM-41 material to a large extent.

2.1.2 SBA-15

SBA-15 is an ordered mesoporous silica material (OMS) like MCM materials. OMS were employed in preparation of advanced materials[44] applied as catalysts, chemical sensors, optical and magnetic devices. Also, these OMS based advanced materials performed as hard templates for the preparation of other ordered mesoporous solids and for drug release. SBA-15 silica displayed significantly higher stability under various conditions (steaming, high temperature) compared with MCM-41 silica. Therefore, it is frequently used for the synthesis of various advanced materials. SBA-15, unlike MCM-41, contains micropores within the walls of primary mesopores forming 3-D connected pore network with connections between mesopores. First, increasing microporosity enhanced hydrothermal stability in steam. The porosity of the walls may also promote molecular transport in catalysis and adsorption. SBA-15 preparation includes four main steps: (1) synthesis of silica–organic polymer nanocomposite using silica source (for example TEOS) and amphiphilic triblock copolymers as a structure-directing agent (template), (2) ageing of the composite at elevated temperatures, (3) filtration (and optionally washing) of the obtained solid, and (4) removing the copolymer by extraction and/or calcination.

2.1.3 Vycor glass

Vycor glass is prepared from a quaternary glass mixture,[45] of typical composition 62.7% SiO_2, 26.9% B_2O_3, 6.6% Na_2O, and 3.5% Al_2O_3. This glass is melted and formed into the desired shape, and then held at a temperature above the annealing point but below that which it would cause deformation. The material phase separates (on a microscopic scale) into two continuous phases, one rich in silica and the other in borosilicate and alkali. It is then treated with a hot dilute acid solution, which dissolves away the borate, leaving some (small) colloidal silica particles inside the pores of the other phase. The finished glass is 96% silica. Vycors have a porosity of 28%, an average internal pore diameter somewhere between 4 and 6 nanometers, and a surface area of between 90 and 200 m^2/g, as calculated from BET analysis of nitrogen adsorption isotherms.

.

2.2 Membrane technology

2.2.1 Classification of membranes

A membrane can be natural or synthetic, thick or thin, where its structure can be homogeneous or heterogeneous and transport across membrane can be active or passive. Passive transport can be driven by various means (e.g. pressure, concentration, electrical difference), neutral or charged. As such, membranes can be classified according to different viewpoints. The first classification is by nature, i.e. biological or synthetic membranes. This is the clearest distinction possible. Synthetic membranes can be subdivided into organic (polymeric or liquid) and inorganic (e.g. ceramic, metal) membranes. Another means of classifying membranes is by morphology or structure. For the case of solid synthetic membranes, the two types of membrane structures are the symmetric and asymmetric (anisotropic) membranes.

In general we have the following **Types of Membranes:**

A. Isotropic Membrane

I. **Microporous Membranes**
II. **Nonporous, Dense Membranes**
III. **Electrically Charged Membranes**

B. Anisotropic Membranes

C. Ceramic, Metal and Liquid Membranes

The principal types of polymeric membranes are classified as shown in Fig. 4.

Ceramic membranes are a type of artificial membranes made from inorganic materials (such as alumina, titania, zirconia oxides or some glassy materials). They are used in membrane operations. By contrast with polymeric membranes, they can be used in separations where aggressive media (acids, strong solvents) are present. They also have excellent thermal stability, which makes them usable in high temperature membrane operations. Like polymeric membranes, they are either dense (non porous) or porous.

Ceramic membranes generally consist of permselective material as disks or tubes or as thin films on porous supports. Thin membrane films can be applied on porous supports (Fig. 5) by particulate, wet-chemical or vapor phase deposition techniques. Examples of permselective inorganic membrane compositions are *dense* Pd alloys and various perovskites, *micro-porous* (< 2 nm) amorphous silica and zeolites and *meso-porous* (2 < Ø < 50 nm) alumina, silica and titania. The latter membranes may act as intermediate supporting layers for micro-porous membranes.

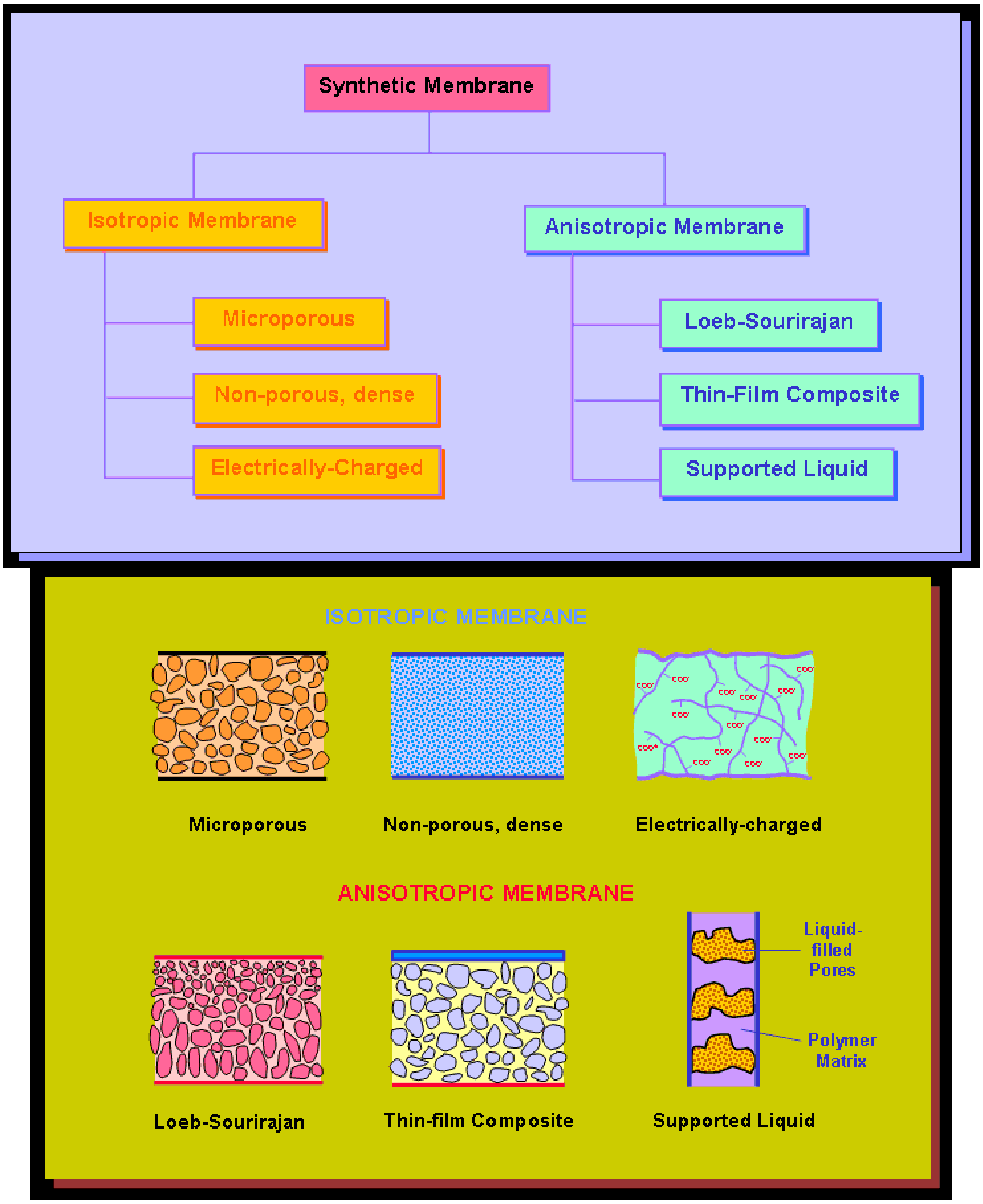

Figure 4. Classification of polymeric membranes

2.2.2 Gas separation with ceramic membranes

- Dense inorganic membranes

These membranes are prepared as unsupported ones as well as thin films on porous supports. They are made of polycrystalline ceramic material, in particular perovskites ($CaTiO_3$) or metal (palladium), which allows specific gas species to permeate the dense material. Depending on the nature of the dense membrane material, hydrogen selectively permeates in atomic (Pd alloys), molecular (dense SiO_2) or protonic (proton-conductive solid electrolytes) form. Both hydrogen and oxygen can permeate selectively through various types of dense membranes. Dense membranes are impermeable to all gases except for a very limited number of gases that can permeate the material (i.e. H_2 through Pd) or can be incorporated into the structure of the membrane and transported through the material (i.e. O_2 through perovskites $CaTiO_3$).

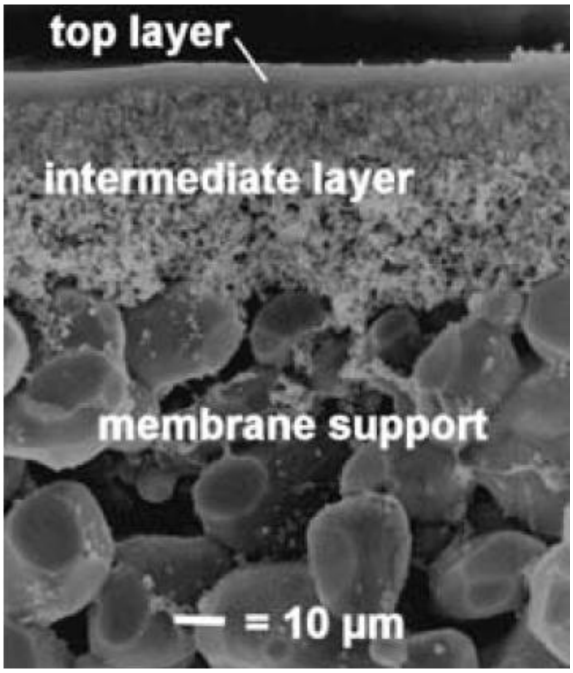

Figure 5. Meso-porous γ -alumina membrane (top layer) on top of a macroporous α- Al_2O_3 “intermediate layer”. The intermediate layer, in turn, is supported by a 2 mm thick macroporous membrane support.

-Amorphous silica membranes

Amorphous silica membranes are produced by sol-gel or chemical vapor deposition (CVD) techniques. The micropore structure of the silica layers is determined by both the reactivity and the size of the precursors. Microporous silica membranes have a high potential for gas separation and pervaporation at high-temperatures in chemically aggressive environments. Such membranes are of particular interest for high-temperature industrial hydrogen separation and purification. Ultra thin microporous silica membranes have been prepared and they offer significantly improved gas permeation compared with earlier types. Such membranes can separate H_2 from N_2

with an H_2/N_2 selectivity of up to ~100 and a permeation of the order of 1×10^{-6} $mol/m^2 \cdot Pa \cdot s$ at 400 °C.

-Carbon membranes

Carbon membranes are produced by pyrolysis (carbonisation at 500–900 °C) of polymeric precursor films (e.g. polyimide, polyfurfuryl alcohol, polyvinylidene chloride or phenolic resin) on a macroporous carbon substrate or an alumina support tube. Alternatively, carbon membranes are produced by CVD of methane at 1000 °C on multilayered porous ceramic tubes. Microporous carbon membranes are classified into activated carbons with pore size 0.8–2 nm and ultra microporous carbons or carbon molecular sieves with pores 0.3–0.6 nm. At present the most important large scale application of carbon membranes is in the production of low cost and high purity N_2 from air, although they are also used for the separation of other mixtures, i.e. H_2 from gas and purification of CH_4.

-Zeolite membranes

Zeolite membranes are generally formed on porous supports by hydrothermal synthesis. The pores in zeolite membranes are part of the crystal structure and, hence, have uniform dimensions. The size of the micropores, with molecular dimensions generally less than 1 nm, can be varied by the crystal structure. Zeolites can separate molecules based on size, shape, polarity and degree of unsaturation, amongst other things. They offer good separation properties for gas molecules. At low temperatures the permeation rate increases with molecular weight, being essentially zero for H_2. At high temperatures (about 500 °C), however, the trend is reversed, and permeation decreases with increasing molecular weight. At high temperatures the permeation rate for H_2 is higher than for hydrocarbons, making the membrane particularly useful for H_2 separation, e.g. in dehydrogenation reactions. The majority of zeolite membranes are of an MFI zeolite-type and show a CO_2/N_2 selectivity of the order of 10, CO_2 permeations being around 10^{-7} $mol/m^2 \cdot Pa \cdot s$ in the temperature range of 30-150 °C. With a potassium-ion exchanged Y-type zeolite, a CO_2/N_2 selectivity of the order of 30, with CO_2 permeations being around 10^{-6} $mol/ m^2 \cdot Pa \cdot s$, has been achieved. Table 2 summarizes the separation properties of different types of ceramic membranes and for a variety of gas mixtures.

Table 2. Gas transport results obtained with different types of microporous and dense inorganic membranes

Membrane type	**Permselectivity**	**H_2 permeation mol/m^{2}· Pa · s**	**T / °C**
Microporous silica	561 (H_2/CH_4)	185×10^{-8}	200
	844 (H_2/CH_4)	73×10^{-8}	25
	10-400 (H_2O/H_2)	10^{-7}–10^{-5}(H_2O)	<150
	188 (He/CH_4)	75×10^{-8}(He)	145
	125 (He/N_2)		145
Zeolite		330×10^{-8}	27
Microporous carbon	31 (He/N_2)	0.31×10^{-8}	150
	127 (He/N_2)	0.27×10^{-8}	25
Perovskite (H+)		16×10^{-8}	950
Pd (supported)		1×10^{-8}	300

2.2.3 Catalytic membrane reactors

Membrane reactors are most commonly used when a reaction involves some form of catalyst, and there are two main types of these membrane reactors: the inert membrane reactor and the catalytic membrane reactor. The inert membrane reactor allows catalyst pellets to flow with the reactants on the feed side (usually the inside of the membrane). It is known as an **IMRCF**, which stands for Inert Membrane Reactor with Catalyst on the Feed side. In this kind of membrane reactor, the membrane does not participate in the reaction directly; it simply acts as a barrier to the reactants and some products.

A catalytic membrane reactor (**CMR**) has a membrane that has either been coated with or is made of a material that contains catalyst, which means that the membrane itself participates in the reaction. Some of the reaction products (those that are small enough) pass through the membrane and exit the reactor on the permeate side. An example of a CMR is given bellow (Figure 6). In literature there is a variety of catalytic membrane reactors for applications such as production of ethylene using oxidative coupling of methane, conversion of syngas to liquid hydrocarbons, direct hydroxylation of aromatic compounds, dehydrogenation reactions etc.

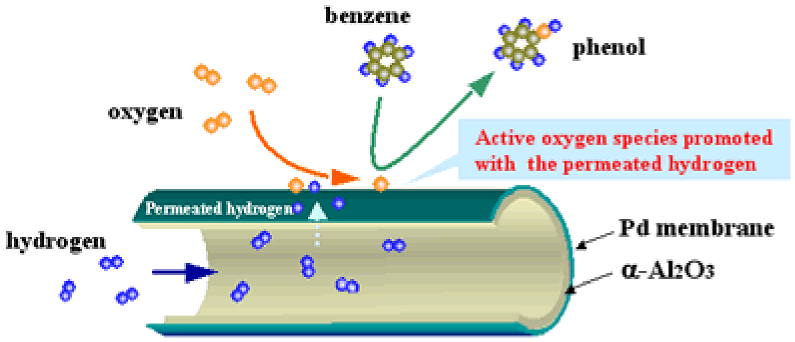

Figure 6. Direct hydroxylation of aromatic compounds by using a Pd membrane reactor

2.3 Adsorption of Gases by Solids – Adsorption isotherms

Before proceeding to the insides of this part, it would be wise to make the distinction between the terms of “adsorption” and “absorption”. As introduced by Kayser in 1881 the term *adsorption* refers to condensation of gases on free surfaces, in contradiction to the gaseous *absorption* where the molecules of gas penetrate into the mass of the absorbent.

The adsorption now is a consequence of the field force present at the surface of the solid (the adsorbent), which attracts the molecules of the gas (adsorbate). The attraction forces may be physical [Van der Waals interactions accompanied by low heats of adsorption (2 to 3 times smaller than heat of evaporation)] or chemical [creation of bonding accompanied by high heats of adsorption (2 to 3 times bigger than heat of evaporation)], thus giving rise to physical adsorption and chemisorption respectively. Adsorption is described by the *adsorption isotherms*, equations that relate the amount of gas absorbed per gram of solid *(x)* with the pressure (*p)* of the gas for a given adsorbate on a given solid and at a fixed temperature.

$$x=f(p)_{T,\mathrm{gas,solid}} \qquad \text{Eq.1}$$

If the gas is below its critical temperature, i.e. if it is vapor, then the alternative form is used where p_o is the saturation vapor pressure of the adsorbate

$x=f(p/p_o)_{T,gas,solid}$ Eq.2

For physical adsorption isotherms measured on a wide variety of solids were grouped in five classes – the five types of the classification nowadays referred as the Brunauer, Emmett and Teller (BET) classification.[46] These types are shown in Fig. 7.

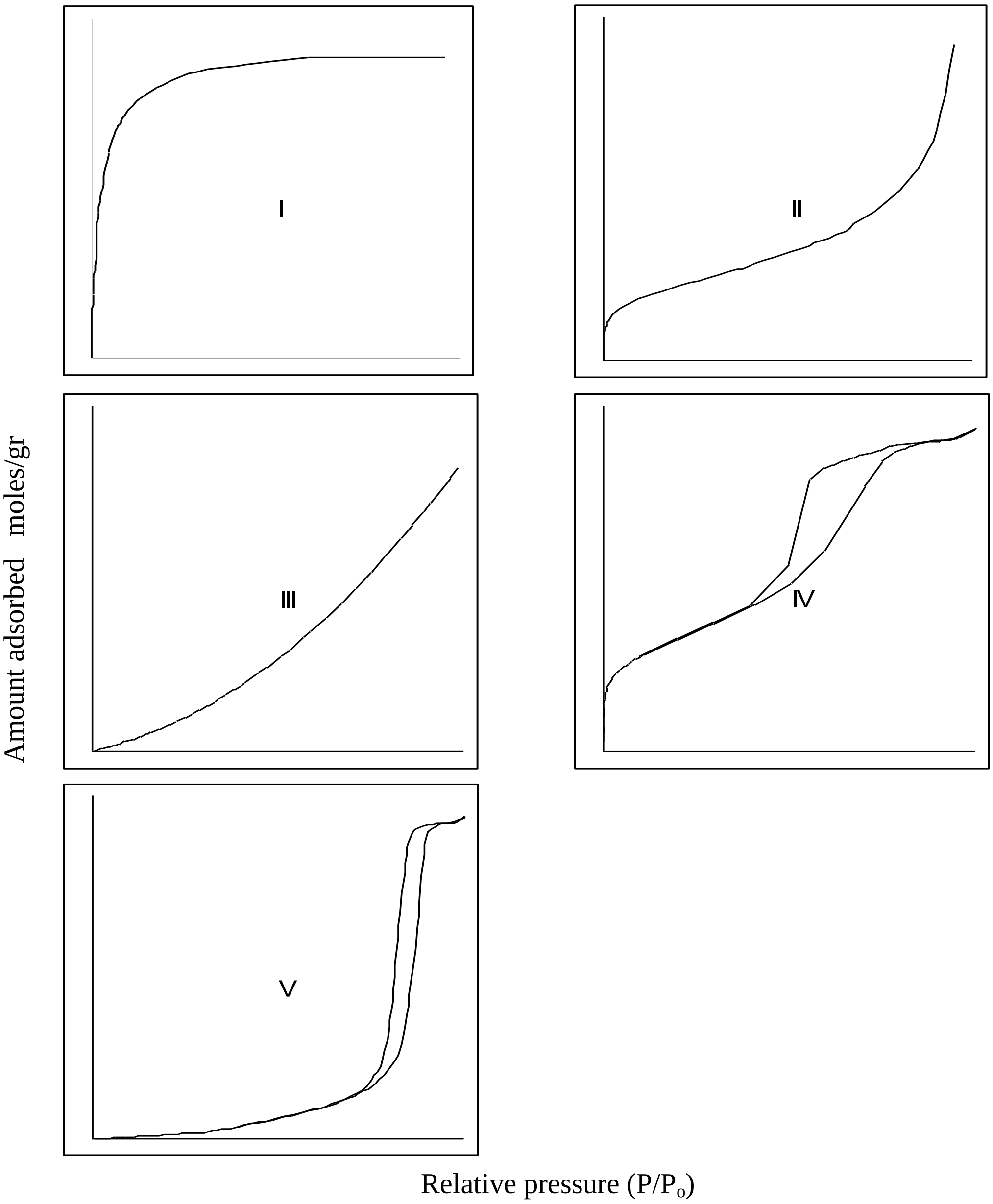

Figure 7. The five types of adsorption isotherm in the BET classification

Type I isotherm is now generally agreed that is obtained by solids of predominately microporous nature. They were first noticed with charcoal as absorbent but recently they have been found with other adsorbents such as silica, ammonium phosphomolybdate, “molecular sieves” such as Linde 13X. The classical interpretation of Type I isotherms proceeds from the assumptions that the adsorbed layer on the walls is only one molecule thick and that the plateau of the isotherm corresponds to the completion of this monolayer.

Types II and III are obtained by Non-porous Solids. In type II isotherm, the point which at low relative pressures the linear portion begins , was taken by Emmett and Brunauer to indicate the completion of the monolayer. In this type of adsorption, the interactions between the adsorbent-adsorbate are stronger than those of adsorbate-adsorbate. Type III isotherms are characterized by being convex to the pressure axis, suggesting that the adsorption is co-operative in nature: the more molecules that are already adsorbed, the easier it is for further molecules to become adsorbed. In this type of adsorption, the interactions between adsorbent-adsorbate are weaker than the adsorbate-adsorbate interactions. Adsorbate-adsorbate interactions will tend to be enhanced if the adsorbate molecule is capable of strong hydrogen bonding. This occurs with water, and to a lesser extent with ammonia.

Type IV isotherms result from adsorption on porous solids containing pores in the intermediate or macroporous range, and is generally accepted to appear in a solid which possesses pores in the “transitional” range of Dubinin. Along the low pressure branch, monolayer adsorption is assumed to take place on the walls of the pores, followed by “capillary condensation” of the adsorbate to a liquid at higher pressures. They possess also a hysteresis loop where the amount adsorbed is greater at any given relative pressure along the “desorption” branch than along the “adsorption” branch.

Type V isotherms are rather rare. They usually result from adsorption on mesoporous solids were interaction forces between adsorbate-adsorbate are strong. The isotherm relates to Type III in a manner that instead of approaching the saturated vapor pressure line asymptotically, the curve bends over giving a branch which becomes almost horizontal.

2.4 The BET equation-Pore size distribution

Following the path laid down by Langmuir in 1916, Brunauer, Emmett and Teller[46] approached the problem of adsorption as a process of interchange of molecules between the gas phase and the adsorbed film. According to Langmuir the surface of the solid is an array of adsorption sites, each site being capable of adsorbing one molecule. He postulated that when a molecule from the gas phase strikes an empty adsorption site, it condenses there, i.e. it remains attached to the site for a mean period τ and then re-evaporates. In 1938 Brunauer, Emmett and Teller extended the Langmuir mechanism to second and higher molecular layers as experimental evidence had made it increasingly likely that multilayer adsorption was a frequent occurrence.

Brunauer, Emmett and Teller have made the following assumptions in order to derive the well known BET equation:

i) the heat of adsorption in all layers above the first is equal to the latent heat of condensation L

ii) the evaporation-condensation constants in all layers above the first are identical

iii) when pressure p becomes equal to the saturated vapor pressure, the adsorbate vapor condenses as an ordinary liquid on to the adsorbed film so that the number of molecular layers becomes infinite on the surface, which is postulated to be freely exposed to the vapor phase.

The BET equation is of the following form:

$$\frac{P}{x\left(P_o - P\right)} = \frac{1}{x_m c} + \frac{c-1}{x_m c}\,\frac{P}{P_o} \qquad \text{Eq.3}$$

where: x is the amount adsorbed in grams per gram of adsorbent, x_m is the corresponding amount of the monolayer formed and c is a constant depending on the net heat of sorption.

The BET equation requires a linear plot of $\frac{P}{x(P_0 - P)}$ vs $\frac{P}{P_0}$ which for most solids using nitrogen as the adsorbate, is restricted to a limited region of the adsorption isotherm, usually in the $\frac{P}{P_0}$ range of the 0.05 to 0.35. This linear region is shifted to lower relative pressures for microporous materials. From the linear plot x_m and c parameters are determined.

Concerning the pore size distribution which is actually the distribution of pore volume with respect to pore size, the BJH method is commonly used. It is generally accepted that the desorption isotherm is more appropriate than the adsorption isotherm for evaluating the pore size distribution of an adsorbent. In certain cases, depending on type of hysteresis that the isotherm shows, the adsorption is recommended for pore size distribution determinations.

With the BJH method, the pore volumes at various relative pressures are calculated using the following equation:

$$V_{pn} = \left(\frac{r_{pn}}{r_{kn} + \Delta t_n / 2} \right)^2 \left(\Delta V_n - \Delta t_n \sum_{j=1}^{n-1} Ac_j \right) \qquad \text{Eq.4}$$

where

r_k is the Kelvin radius and for nitrogen it is given $r_k = \frac{4.15}{\log(P_0 / P)}$

r_p is the actual pore radius with $r_p = r_k + t$, where t is the thickness of the adsorbed layer. A convenient method for estimating t is the following equation as proposed by deBoer:

$$t = \left[\frac{13.99}{\log(P_0 / P) + 0.034} \right]^{1/2} \qquad \text{Eq.5}$$

Ac_j is the area exposed by the previously emptied pores from which the physically adsorbed gas is desorbed. This term is evaluated as follows: The area of each pore A_p

is a constant and can be calculated from the pore volume, assuming cylindrical pore geometry. That is,

That is,

$$A_p = \frac{2V_p}{r_p} \qquad \text{Eq.6}$$

while the term *c* is given by

$$c = \frac{\bar{r}_p - t_{\bar{r}}}{\bar{r}_p} \qquad \text{Eq.7}$$

2.5 Diffusion mechanisms in membranes

A real pore structure generally consists of a more or less random network of interconnecting pores of varying diameter and orientation. However it is helpful to consider first the mechanisms by which diffusion can occur by reference to a straight cylindrical pore.

2.5.1 Micropore diffusion

Nowadays it is well established that gas transport through microporous membranes takes place through two simultaneously occurring mechanisms, namely micro-pore diffusion and sorption. It has been shown that the activation energy for permeation is an apparent one, which consists of the isosteric heat of sorption and the activation energy for micropore diffusion. Barrer was the first who introduced a theoretical model describing the gas transport in zeolite crystals. Intracrystalline diffusion was considered to occur of molecular species that follow Langmuir's isotherm and therefore their diffusivity is independent of the fraction of channel sites occupied. An analysis of the interface processes can also be implemented considering that entry into and exit from porous crystals can occur only through the mouths of the channels (pores). The external surface is assumed to provide different kind of adsorption sites categorized to these located around channel mouths and to those existing on the plain surface. According to this analysis, the following equation was derived for the case that both internal and external sorption obey Henry's Law:

$$J = \frac{J_{id}}{1 + 2 \bullet \frac{d}{l} \bullet \exp\left[\left(E_s + \Delta \mathrm{E} - \Delta \mathrm{E}s - E_1\right)/RT\right]} \qquad \text{Eq.8}$$

where J_{id} is the flux in the ideal case that interface processes do not have an important contribution in flux,

ΔE is the energy difference between the gas phase and the molecules present in the micropores and is equal to the isosteric heat of sorption,

ΔE_s is the energy difference between the molecules adsorbed on the external surface and the gas phase,

E_s is the activation energy for pore entrance from the external surface,

d is the jump distance for micropore diffusion and l the membrane thickness.

From the above equation, it is clear that interface processes become less significant if the surface barrier is low (low ΔEs and or Es) for large crystals or thick membranes and for high temperatures. Based on the above analysis, de Lange *et al.*[47] proceeded to an integration of sorption and diffusion processes in micropores by making the implicit assumption that since sorption is strongly enhanced in the micropores compared to a ‘free’ surface, the term ΔEs which is the adsorption energy on the external surface can not be higher than ΔE (the sorption energy in micropores). Moreover, whereas in most of the cases permeance experiments for the calculation of the activation energy take place at elevated temperatures (373–600 K) and membrane thickness (2–5 μm for silica and 10–50 μm for zeolitic membranes) is large enough compared to the molecule jump distance. Therefore, it could be well assumed that both internal and external sorption obey Henry’s Law and that interface processes are of minor importance. Thus, they derived the following equation describing the activated flux through microporous membranes:

$$J = -\frac{\rho 1 - \varepsilon_p}{l \varepsilon_p} D_o \exp\left(\frac{-E_1}{RT}\right) K_o \exp\left(\frac{q_{st}}{RT}\right) \Delta P \qquad \text{Eq.9}$$

where ρ(kg/cm^3) is the top layer skeletal density, D_o (m^2/sec) the mean intrinsic diffusion coefficient for micropore diffusion, K_o the intrinsic Henry constant, ε_p the top layer porosity and ΔP(Pa) is the differential pressure across membrane. If the interface processes are not rate determining indeed and q_{st} is available from sorption experiments at different temperatures, then it is clear from Eq. E9 that E_1 can be derived from the apparent activation energy for permeation E_{act} by:

$$E_1 = E_{act} + q^{st} \qquad \text{Eq.10}$$

where, E_1, the activation energy for micropore diffusion and E_{act} can be determined from permeance measurements though the Arrhenius analysis.

2.5.2 Knudsen diffusion

In small pores or at low pressure, the mean free path may become comparable to or even greater than the pore diameter so that collisions between a molecule and the pore wall occur more frequently than intermolecular collisions. A molecule hitting the wall exchanges energy with the atoms or molecules of the surface, which will most likely be reflected; that is, the velocity of the molecule leaving the surface bears no relation to the velocity of the incident molecule and its direction is purely random. In other words diffusivity depends only in the pore size and the mean molecular velocity while the different components of a mixture propagate independently one of the other. This is known as Knudsen diffusion. In such a case, the diffusion coefficient is as follows:

$$D_K = \frac{4r}{3}\left(\frac{2kT}{M\pi}\right)^{\frac{1}{2}}\frac{2-f}{f} \qquad \text{Eq.11}$$

where r: is the pore radius in cm.

k: Bolzman constant

T: temperature in Kelvin (K).

f: the proportion of molecules that is randomly reflected (for most purposes f may be approximated to unity).

M: is the molecular weight of the gas

From the above equation, it is clear that Knudsen diffusion coefficient (D_K) slightly depends on temperature, while it is independent of pressure since the diffusion mechanism does not involve intermolecular collisions.

The steady-state flux according to Fick's first law is in molecules per second for one cylindrical capillary,

$$J_K = -\pi r^2 D_K \frac{dc}{dx} = -\frac{4r^3}{3}\left(\frac{2\pi kT}{M}\right)^{\frac{1}{2}} \frac{C_o - C_\ell}{\ell} \qquad \text{Eq.12}$$

where C_o is the value of C at $x = 0$ and C_l its value at $x = l$.

In accordance with the definition of the permeability coefficient where P=D*S (S being the solubility), we can define the Knudsen (P_K) permeability coefficient as $P_K = D_K$ for S = 1. For a capillary of surface area U, the following equation holds for P_K

$$P_K = \frac{J_K \ell}{U(C_o - C_\ell)} \qquad \text{Eq.13}$$

From equations E12, E13 it is apparent that for two different gas molecules A and B that flow in the same capillary with Knudsen mechanism, the following equation holds:

$$P_{KA}\sqrt{M_A} = P_{KB}\sqrt{M_B} \qquad \text{Eq.14}$$

2.5.2.1 Extension to porous media

For porous media where the actual pore length is $\tau \times \ell$ (τ being the tortuosity of the media and ℓ the thickness of the material), permeability is given by the following equation:

$$P = \frac{8\varepsilon^2}{3A_c}\frac{\delta}{\tau k_1}\left(\frac{2kT}{\pi M}\right)^{1/2} \qquad \text{Eq.15}$$

where

◆ε is the porosity of the media as expressed by

$$\varepsilon = \frac{V_{pores/gr}}{V_{pores/gr} + 1/\rho_{solid}} \qquad \text{Eq.16}$$

with ρ_{solid} being the density of the material

◆ k_1 is a shape factor which for cylindrical pores is 1.

2.5.3 Poiseuille flow

If there is a difference in total pressure between the ends of a capillary, there will be a bulk (laminar) flow in accordance with Poiseuille's equation. The diffusion coefficient is given by the following equation

$$D_p = \frac{pr^2}{8\eta} \qquad \text{Eq.17}$$

where (p) is the absolute pressure (dyn/cm^2) and (η) is the viscosity

2.5.4 Surface diffusion

The transport mechanisms considered so far, all involve diffusion through the fluid phase in the central region of the pore. If there is significant adsorption on the pore wall, there is the possibility of an addition flux due to diffusion through the adsorbed phase or <surface diffusion>. If adsorption equilibrium is favorable, the molecular density in the adsorbed layer may be relatively high. The fluxes through the gas phase and the adsorbed phase are to a first approximation independent and therefore additive, so that the diffusivity will be given by the sum of the pore and surface contributions. For a single pore

$$D = D_p + K' D_s \qquad \text{Eq.18}$$

where D_s is the surface diffusivity and K' is the dimensionless adsorption equilibrium constant expressed in terms of pore volume (moles adsorbed per unit pore volume/moles per unit volume in gas phase) and D_p denotes the contributions from Knudsen and molecular diffusion, as well as from Poiseuille flow (if significant). Considering a pore within a solid matrix, it is more usual to express the equilibrium constant in terms of the total volume of the porous solid so that in place of the previous equation we have

$$D = D_p + K\left(\frac{1-\varepsilon_p}{\varepsilon_p}\right)D_s \qquad \text{Eq.19}$$

were ε_p represents the porosity.

Surface diffusion is an activated process but the diffusional activation energy is generally smaller than the heat of adsorption. Therefore, it is generally insignificant at temperatures which are high relative to the normal boiling point of the sorbate.

2.6 Absorption of Gases by ionic liquids

2.6.1 Physical interaction

A number of investigations have shown that CO_2 is remarkably soluble in imidazolium-based ionic liquids.[47-49] In all these studies, the ILs solvation capacity for CO_2 outperformed this for other gaseous molecules. In this regard, imidazolium based ionic liquids may be established as excellent candidates for gas separations of high industrial interest such as CO_2/H_2, CO_2/N_2, CO_2/CH_4 and CO_2/CO.

By observing the effects of varying the anion among different imidazolium-based ILs, Maginn and coworkers[50] have shown that the anion influences the solubility of CO_2 in ionic liquids to a greater extent compared to the cation. Earlier, the nature of these anion–CO_2 interaction has been probed using vibrational spectroscopic methods. Kazarian et al. have reported a weak Lewis acid–base interaction between CO_2 and [PF_6^-] the anions of the ILs[51] based on ATR-IR studies. Furthermore, molecular dynamic (MD) simulations[52] pointed out that apart from ion-quadrupole interactions that are expected between the anion and CO_2, ion-induced dipole interactions could also be important. MD simulations indicated also that CO_2 organizes strongly around the IL anion in a “tangent like” configuration that maximizes favorable interactions.[53]

2.6.2 Chemical interaction

Apart from the physical solubility aspect described in the previous section, ILs can be functionalized through formation of covalent bonding in order to capture CO_2. Taking into account the chemistry of aqueous organic amines reacting with CO_2, amine functionalities can be added to ILs to introduce specific and tunable chemical reactivity with CO_2. The first reported example contained an amine group on an imidazolium cation which reacted with CO_2 in a manner similar to aqueous amines. Carbamic acid is formed at the first step followed by carbamate and ammonium ions formation in a stoichiometry of one CO_2 to two amines, [54,55] as shown in reactions 1 and 2 below.

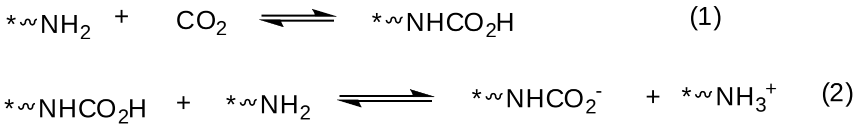

Recently Brennecke and co workers[56] introduced anion amino functionalized ILs that react with CO_2 in a ratio of one CO_2 per one amine (1:1stoichiometry). Moreover, the results demonstrate that the location of functional groups (anion vs cation) in ILs provides an additional degree of freedom in the design of functionalized ILs for specific applications.

3 EXPERIMENTAL PART

3.1 Characterization of porous materials

3.1.1 Nitrogen porosimetry

Liquid nitrogen isotherms at 77 K were obtained using the Autosorb-1 MP (Quantachrome) porosimeter. Before each measurement, the samples were degassed under high vacuum 10^{-5} mbar for 24 hours at the outgassing stations of the instrument. The outgassing temperatures were 433 K for the SILPs and 453 K for the supports and the silylated supports.

3.1.2 Adsorption isotherms-Diffusivity

The CO_2, CO gas solubility measurements were performed with a gravimetric microbalance (IGA, Hiden Analytical). The masses of the sample and counterweight pans, the hooks, the counterweight material and the hang chains of the microbalance assembly were of the order of one to three hundreds of milligrams per item and were defined with an accuracy of ±0.1%. The materials were appropriately selected to induce a symmetrical configuration to the balance set-up in order to minimize buoyancy effects. The microbalance had a 0.1 μg stable resolution. The amount of the bulk ionic liquid usually applied was 100-150 mg. Before each measurement, the bulk ionic liquid samples were degassed at 353 K and high vaccum (10^{-5} mbar). The involved amounts of the developed SILP systems and the corresponding supports were of the order of 50 mg and degassing was performed at high vacuum (10^{-5} mbar) and temperatures of 433 K and 453 K respectively. It should be noted that outgassing temperatures were selected in relation to the results of DSC analysis and were set at least 100 K lower than the melting or decomposition temperatures. The maximum time allowed to reach equilibrium at each pressure step was 10 hours and the internal algorithm of the microbalance software detected equilibration within a period of 3-4 hours.

3.2 Characterisation of membranes

3.2.1 Permeability-selectivity

Permeability and selectivity evaluation was performed in a flow apparatus (Figure 8) in which the feed, permeate and retentate gas compositions were analysed using a SRI gas chromatograph equipped with a stream selection valve, a gas sampling valve and TCD, FID detectors in series. Chromatographic separation was achieved with an Alltech Hayesep D 100/120 packed column (1/8, 30 ft).

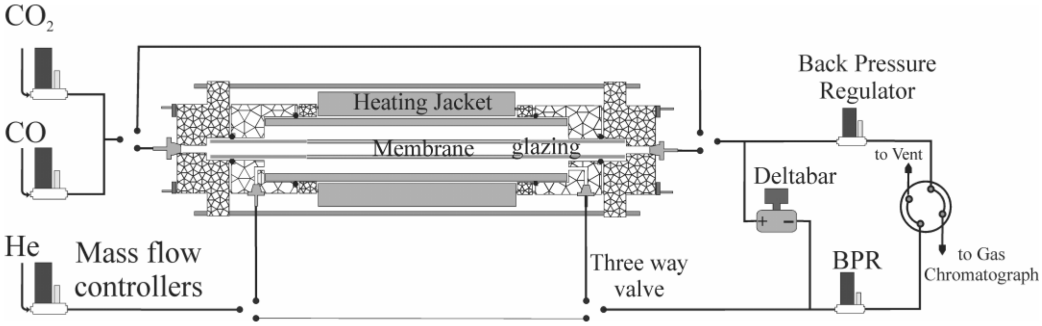

Figure 8. The Wicke-Kallenbach apparatus applied for the measurement of the CO_2/CO selectivity

The gas flow of each stream was controlled by electronic mass flow controllers (Bronkhorst F-200CV) with a scale of 2–100 ml/min for CO (99.997%) and CO_2 (99.998%) and 20–1000 ml/min for He (99.999%) that was used as the sweep gas from the permeate side of the membrane. The pressure at both sides of the membrane was controlled by means of two electronic backpressure regulators (Bronkhorst P-702CV). The temperature was controlled with a PID controller and a Type K thermocouple in contact with the surface of the testing cell. All tests were performed in the Wicke-Kallenbach configuration with a mixture of 50/50 %vol CO_2/CO sweeping the inner side of the tubular membrane (feed) and He sweeping its outer side (permeate).

3.3 Pore surface chemistry/morphology

3.3.1 Adsorption/desorption of water

The water adsorption-desorption isotherms were obtained using a homemade stainless steel gravimetric rig. The balance head (CI), counterweight compartment, valves andtubing of the system were thermostated in an air-circulating bath (±0.1 K), whereas the sample compartment was separately thermostated in a silicon oil bath (±0.01 K).

3.3.2 Thermogravimetric analysis

TGA experiments were performed with SETCYS-Revolution instrument and with temperature increments of 10 ^{o}C per minute.

3.3.3 SEM/EDAX

The cross sectional elemental composition of the membranes was analyzed with a Field emission SEM (JEOL JSM-7401F) equipped with EDS analyzer.

3.3.4 Small Angle X-ray Scattering (SAXS)

Small-Angle X-ray Scattering (SAXS) measurements were carried out on a SAXS/WAXS apparatus manufactured by JJ X-Ray Systems. The samples were in powder form and the measured Q range varied from about 0.012 to 0.16 Å^{-1}.

3.3.5 Differential scanning calorimetry (DSC)

Modulated DSC analysis was performed with a TA Instruments 2920 MDSC. The runs proceeded with a cooling down to –50 ^{o}C followed by an isothermal step of 10 minutes at this temperature and heating up to 330 ^{o}C with rates of 1.5 ^{o}C/min and 10 ^{o}C/min. The modulation parameters were set to 0.08 W/g for the amplitude and –2x10^{-4} W/g/^{o}C for the slope.

3.3.6 X-ray diffraction (XRD)

The X-ray diffraction (XRD) measurements were performed at a D8 Bruker system using Cu-Kα radiation. The samples were in powdered form and were mounted on a glass slide. Measurements were carried out to both pristine and SILP samples.

3.3.7 Elemental analysis

Elemental analysis (C, H, N) was performed with a Perkin Elmer 2400 CHN Analyser.

3.3.8 NMR

NMR spectra were obtained on a Bruker Avance/500MHz spectrometer.

3.4 Synthesis of ionic liquids and silylated ionic liquids

3.4.1 Synthesis of 1-butyl-3-methylimidazolium hexafluorophosphate ([bmim][PF_6^-]).

1-Chlorobutane (3 mL, 28.7 mmol) was added to a round bottom flask containing 1-methyl-imidazole (2 mL, 23.4 mmol). The flask was fitted with a reflux condenser and the reaction mixture was heated at 85 ^oC under stirring and N_2 atmosphere for 48 hr. The viscous yellow–orange liquid obtained was washed with EtOAc (2 x 30 mL) and dried under high vacuum at 90 ^oC to give 3.9 g (95%) of 1-butyl-3-methylimidazolium chloride. For the ion exchange step, 1.39 g (7.59 mmol) of 1-butyl-3-methylimidazolium chloride was dissolved in 6 mL of CH_2Cl_2 followed by the addition of sodium hexafluorophosphate (1.7 g, 10.1 mmol) as a solution in CH_3CN (10 mL). The milky solution was left under stirring at room temperature for 24 h, cooled at -10 ^oC for 10 min and then centrifuged at 9000 rpm for 20 min to remove sodium chloride produced during the ion exchange step. The supernatant phase was treated with 10 mL of dichloromethane and the resulting organic phase was washed with deionized (3 × 50 mL) water until the $AgNO_3$ test was negative. The organic phase was dried over $MgSO_4$, filtered and then concentrated in a rotary evaporator to yield 1.57 g (73%) of less viscous light yellow to colorless liquid. ^1H NMR (500 MHz, $CDCl_3$) : δ 0.93 (t, 3H), 1.34 (m, 2H), 1.86 (m, 2H), 3.95 (s, 3H), 4.2 (t,2 H), 7.47 (s,2H), 8.71 (s,1H).

3.4.2 Synthesis of 1-methyl-3-(3-triethoxysilylpropyl) imidazolium hexafluorophosphate ([spmim][PF_6^-]).

(3-Chloropropyl)-triethoxysilane (12 mL, 49.8 mmol) was added to a round bottom flask containing 1-methylimidazole (3 mL, 37.6 mmol). The flask was fitted with a reflux condenser and the reaction mixture was heated at 85 ^{o}C under stirring and N_2 atmosphere for 48 hr. The resulting mixture was washed twice with ethyl acetate (30 mL) and then dried under vacuum at 80 ^{o}C to afford 1.1 g (90%) of a viscous yellow liquid. ^{1}H NMR (500 MHz, $CDCl_3$):δ 0.61(t, 2H, Si-$\underline{CH_2}$-CH_2-CH_2-N), 1.23 (t,9H, $\underline{CH_3}$-CH_2-O), 2.0 (m, 2H, Si-CH_2-$\underline{CH_2}$-CH_2-N), 3.78 (m, 2H, CH_3-$\underline{CH_2}$-O), 4.11 (s, 3H, N-CH_3), 4.33 (t, 2H, Si-CH_2-CH_2-$\underline{CH_2}$-N), 7.26 (s, 1H, N-C$\underline{H}$-C$\underline{H}$-N), 7.17 (s, 1H, N-C$\underline{H}$-C$\underline{H}$-N), 10.97 (s, 1H, N-C$\underline{H}$-N).

Ion exchange step: The complex of 1-methyl-3-(3-triethoxysilylpropyl) imidazolium chloride (281.2 mg, 0.87 mmol) was dissolved in CH_3CN (3 mL) and then treated with 1.1 equivalent of sodium hexafluorophosphate (160.9 mg, 0.96 mmol). The resulting slurry was stirred for 5 days at room temperature under N_2 atmosphere. The precipitate was removed by centrifuging at 9000 rpm for 20 min, while volatiles where removed by rotary evaporation at reduced pressure to give a light yellow liquid.

3.4.3 Synthesis of 1-methyl-3-(1-trimethoxysilylmethyl)imidazolium hexafluorophosphate ([smmim][PF_6^-]).

Chloromethyl-trimethoxysilane (2 mL, 13.3 mmol) was added to a round bottom flask containing 1-methylimidazole (1.4 mL, 17. 6 mmol). The flask was fitted with a reflux condenser and the reaction mixture was heated at 85 ^{o}C under stirring and N_2 atmosphere for 48 hr. The resulting mixture was washed with diethyl ether (2 × 30 mL) and then dried under vacuum at room temperature to afford 3.2 g (95%) of a viscous orange/brown liquid ([smmim][Cl^-]).

Ion exchange step: The complex of 1-methyl-3-(1-trimethoxysilylmethyl) imidazolium chloride (3.2 g, 12.7 mmol) was dissolved in CH_3CN (4 mL) and treated with 1.1 equivalent of sodium hexafluorophosphate (2.3 g, 13.7 mmol) dissolved in CH_3CN (40 mL). The resulting slurry was stirred for 5 days at room temperature under N_2 atmosphere. The precipitate (NaCl) was removed by centrifuging at 9000 rpm for 20 min, while volatiles where removed by rotary evaporation at reduced pressure to give a yellow liquid ([smmim][PF_6^-]).

3.5 Development of supported ionic liquid systems for CO_2 capture

Hybrid materials of ionic liquid on Vycor, MCM-41 and SBA-15 supports were prepared with the "grafting to" method. The Vycor® substrate was initially treated with H_2O_2 30% w/v at 90 °C for 30 min, washed with deionized water until neural pH, and dried at 433 K for 24 hr under high vacuum. Solvents were used as purchased without further drying. Toluene (puriss, Reag ACS, Aldrich), dichloromethane (GC 99.5%, Aldrich), chloroform (GC, Aldrich), methanol (≥99.8%, Aldrich). Reaction reagents were used as purchased without further purification. (3-Chloropropyl)-trimethoxysilane (97%, Aldrich), (3-chloropropyl)-triethoxysilane (95%, Aldrich), sodium hexafluorophosphate (98%, Aldrich), hexafluorophoric acid (60 wt% solution in water, Aldrich).

3.5.1 Pore surface activation

Vycor glass was treated in different basic conditions and time periods in order to induce more hydroxyl groups on the pore surface.

Table 3. Surface activation conditions

Sample ID	pH	Time
Vyc_1	8.1	30 min
Vyc_2	8.1	1 hr
Vyc_3	8.1	3 hr
Vyc_4	8.5	20 min
Vyc_5	8.5	1 hr
Vyc_6	9.5	20 min
Vyc_7	9.5	2 hr
Vyc_8	9.5	6 hr

In a round bottom flask, approximately 500 mg of vycor glass was treated under sonication with an aqueous solution of NH_4OH of different pH (Table 3). Then, samples were washed with deionized water until a neutral pH was reached.

3.5.2 Preparation of the hybrid material 1-(silylpropyl)-3-methyl-imidazolium hexafluorophosphate/Vycor® ([spmim][PF_6^-] /vycor®).

Samples prepared via a silylation procedure are summarized in Table 4.

Table 4. Silanization conditions

Vycor					
Samples	S3	S4	S5	S1	S2
Solvent	CH_2Cl_2	$CHCl_3$	$CHCl_3$	toluene	toluene
Reflux temperature (K)	313	334	334	383	383
Silylant concentration (M)	0.05	0.4	0.4	0.4	0.4
Reaction time (h)	24	24	24	24	24

The synthetic procedure of grafting the (3-chloropropyl)trimethoxy silane on the surface of vycor was as follows: A solution of (3-chloropropyl)trimethoxy silane in the corresponding solvent (Table 4) and corresponding concentration was added to Vycor® glass in a round bottom flask. The mixture was stirred under reflux and N_2 atmosphere for 24 h. The samples were then washed by refluxing sequentially with pentane (40 mL), CH_3CN (40 mL) and dried in vacuum.

Sample S6. Sample S1 (precursor) of 1.5 g was treated with an excess of 1-methylimidazole at 85 ^oC under N_2 atmosphere for 48 hr. The sample was then washed with toluene at rt (2 × 15 mL) and dried in vacuum for 2 hr. To the dried sample, a solution in methanol of HPF_6 (20 ml, 0.05M) was added. The mixture was sonicated under N_2 atmosphere for 30 min and then stirred at room temperature for 72 hr. Ion exchange was confirmed with a positive $AgNO_3$ test. The mixture was filtered and subsequently washed with deionized water until neutral pH and a negative $AgNO_3$ test was observed in the water phase. The sample was left to dry in air.

Sample S7: Sample S4 (precursor) of 1.04 g was treated with an excess of 1-methylimidazole at 85 ^oC under N_2 atmosphere for 48 hr. The sample was then washed with toluene (2 × 15 mL at rt) and dried in vacuum for 2 hr. To the dried sample, a solution (0.06 M) of $NaPF_6$ (50 mg) in MeOH (5 mL) was added and the mixture was sonicated under N_2 for 30 min. Ion exchange was confirmed with a positive $AgNO_3$ test. The mixture was left at room temperature under stirring for 70 hr. The reaction mixture was filtered and the sample was washed with MeOH (30 mL) for 15 min. After filtration, the sample was dried in vacuum for 1 hr.

Sample S8: Sample S5 (precursor) of 0.74 g was treated with an excess of 1-methylimidazole at 85 ^{o}C under N_2 atmosphere for 48 hr. The sample was then washed with toluene (2 × 15mL at rt) and dried in vacuum for 2 hr**.** To the dried sample, a solution (0.05 M) of $NaPF_6$ (56 mg) in MeOH (7 mL) was added and the mixture was stirred under N_2 atmosphere at room temperature for 90 hr. $AgNO_3$ test was found positive in the first 24 hr from the reaction onset. The reaction mixture was filtered and the sample was washed by reflux with MeOH (30 mL) for 15min. After filtration, the sample was dried in vacuum for 1 hr.

3.5.3 Preparation of the hybrid material 1-(silylpropyl)-3-methyl-imidazolium hexafluorophosphate/MCM-41 ([spmim][PF_6^-]/MCM-41).

204 mg of MCM-41 was dried at 423 K and in high vacuum for 1 h. To the dried powder, a solution of triethoxychloropropyl silane (2.5 mL , 10.4 mmol) in 10 mL of dry $CHCl_3$ was added and the mixture was refluxed under N_2 atmosphere for 24 hr. The mixture was filtered and the remaining powder was washed sequentially with pentane (30 mL), acetonitrile (30 mL) and then refluxed with diethyl ether (30 mL). The powder was filtered and dried at 343K in vacuum for 1 h. Then 1-methyl imidazole (5 mL) was added and the mixture was stirred at 358 K under N_2 atmosphere for 48 h. The mixture was filtered and the remaining powder was refluxed with diethyl ether (30 mL) for 30 min, filtered and the remaining powder was then dried at 343 K under vacuum for 1 hr. To 64 mg of the dried powder, a solution of $NaPF_6$ (68 mg, 0.4 mmol) in EtOH (6 mL) was added and the mixture was left for 5 days under stirring and N_2 atmosphere. $AgNO_3$ test was positive in the first 24 hr from the reaction onset. The reaction mixture was filtered and the sample was washed by reflux with MeOH (30 mL) for 15 min. After filtration, the sample was dried in vacuum for 1hr.

3.6 Development of ionic liquid membranes for CO_2/CO separation

Tubular nanofiltration membranes (tubes of 15 cm length, 0.7 cm ID, 1 cm OD, glazed ends 1.5 cm) with an active NF area of 26 cm^2 were obtained from Inopor®. The tubes consisted of a macroporous α-alumina support (2.5 μm mean pore size), two intermediate γ-alumina layers of mean pore size 0.5 and 0.25 μm and thickness of 25 and 40 μm respectively, and a top separating layer of about 1.5 μm thickness, located on the inner side of the tubes. The pore size for the NF γ-alumina layer was 5 nm and for the NF silica layer 1 nm.

Table 5. Samples treated in different conditions for membrane activation

sample	pH	Temperature (^{o}C)	Time
Cer_1	9,8	r.t	6 h
Cer_2	9,8	r.t	21 h
Cer_3	9,8	60	20 min
Cer_4	9,8	60	1 h
Cer_5	9,8	95	20 min

Before preparing the hybrid material, nanofiltration membranes were activated by means of increasing the hydroxyl groups on their surface. For this reason, basic hydrolysis was chosen (see Table 5) and different samples were prepared in order to elucidate optimal conditions. The experimental conditions were as follows: In a round bottom flask, a solution of NH_4OH in water (pH = 9.8) was applied to a piece of the membrane (~1 g) and the mixture was either left at room temperature or heated in an oil bath (Table 5) for several periods of time. The samples were then washed with deionized water.

3.6.1 Membrane accommodation

After surface activation at the optimum conditions (NH_4OH pH = 9.8, 20 min at 60 ^{o}C), the tubular NF membranes were incorporated in a specially manufactured high-pressure stainless-steel reactor cell (Figure 9), which apart from its use in the membrane modification procedure was further applied as the permeation cell for investigating the CO_2/CO separation performance. In this way, we avoided contact of the SILM with the atmospheric air moisture.

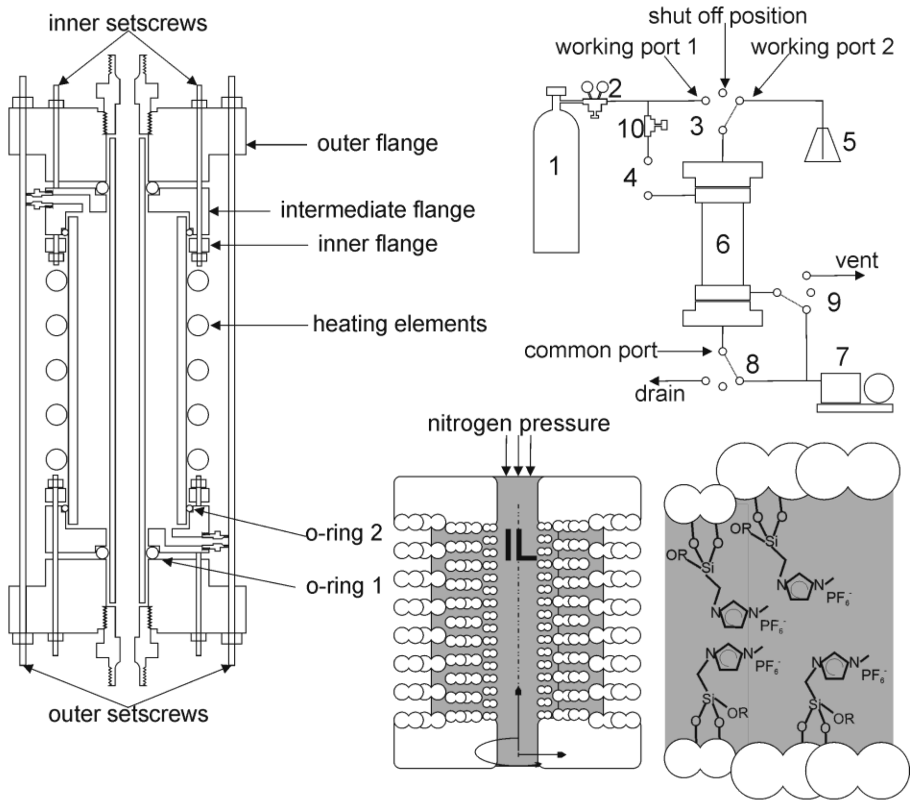

Figure 9. The complete set-up applied for the imbibition reaction modification of the tubular ceramic membranes

As it can be seen in Figure 9 (left), the glazed ends of the tubular ceramic membrane (1.5 cm each) are initially passed through the borehole of two flanges (intermediate), while the inner flanges hold in place the tubular borosilicate glass cell of the reactor. Thereafter the outer flanges are introduced and squeezed together with the other two, by means of four internal setscrews. In this way the small diameter o-ring that embraces the glazed ends of the membrane, ensures efficient gas tight sealing between the outer and inner space of the membrane, whereas the large diameter o-ring, placed around the borosilicate glass cell, ensures the proper sealing between the outer space of the membrane and the environment. The outer setscrews allow for the involvement of elevated pressures in the internal space of the membrane tube and are tightened with a lower torque than this applied for the inner ones.

3.6.2 Membrane modification

3.6.2.1 Physical imbibition

The reactor cell is transferred to the imbibition/reaction device (Figure 9, right side) where the membrane is evacuated at both its sides for several hours by switching the three-way valves 8 and 9 to the vacuum pump (7) working ports and the valves 3 and 4 to the shut-off position. The maximum temperature applied at this stage is 180 ^{o}C to ensure the preservation of most of the surface hydroxyls of the membrane. Thereafter, the temperature is decreased and a solution (0.6 M) of the silylated IL in acetonitrile is suctioned under vacuum to the internal space of the membrane tube (lumen) by switching valve 3 to the IL solution working port (5) and valve 8 to the shut-off position.

As soon as the bore space of the membrane fills up with the solution, valve 3 is switched to the nitrogen flask working port (1) and the pressure is increased by means of the front pressure regulator (2). The pressure is applied to assure proper wetting of the pore structure and its maximum value depended on the pore size of the involved nanofiltration membrane. Then the high vacuum on the external side of the membrane is replaced by a gentle flow of nitrogen gas, generated by means of the second front pressure regulator (10) after switching valve 4 to the on position. The nitrogen stream sweeps the external surface of the membrane and flows out of the cell, through valve 9, which is switched to the vent working port. This configuration ensures sufficient pressure relief in case of membrane failure and, at the same time, the atmosphere at the external side of the membrane is inert during imbibition and subsequent reaction.

3.6.2.2 Reaction

The imbibition procedure ceases as soon as there is an optical indication for complete wetting of the membrane external area. This was achieved after about 1 hour at the pressures of 7 and 1 MPa for the NF membranes with pores of 1 and 5 nm respectively. At this point, the internal pressure is lowered to permit a very small flow rate of the IL solution through the pore structure. The temperature is increased to 80 ^{o}C and the reaction procedure starts and continues (see Figure 9) until the collection of a 5 mL volume of the IL solution from the vent working port of valve 9. This corresponds exactly to the internal volume of the membrane tube, from the lower end of its upper glazed part to the common port of valve 3.

3.6.2.3 Washing and regeneration

After the completion of the reaction stage, the pressure in the internal side of the membrane is relieved down to 2 bars and the valve 8 is energized to the drain working port in order to remove the remaining IL solution. Then both the internal and external sides of the membrane are evacuated and pure solvent (acetonitrile) is suctioned in the internal side of the membrane. The sequence of the solvent suction and draining is repeated for a minimum of three times and, finally, acetonitrile is driven to flow through the pores of the membrane under elevated pressure with a procedure similar to the one already described in section 3.6.2.2. This stage is necessary to remove excess (unreacted) ionic liquid phase from the interior of the pores. Then the pressure is relieved, the solvent is drained and the residual solvent is removed with the application of high vacuum on both sides of the membrane under elevated temperature (180 ^{o}C). Energizing all the surrounding valves to the shut-off position seals the reactor cell, which is then transferred to the permeability apparatus.

4 RESULTS-DISCUSSION

4.1 Supported ionic liquid systems for CO_2 capture

CO_2 capture experiments were performed in materials with pore size distributions of 4 nm (Vycor), 2.3 nm (MCM-41) and 3.3 nm (MCM-41) which were modified by a covalently linked ionic liquid in order to produce the desired hybrid material. The synthetic procedure was performed by the “grafting to” method where the hydroxyl groups on the surface of the materials were covalently bonded to a chloropropyl trialkoxysilane followed by an SN2 type reaction (see Figure 10) with methyl imidazole in order to produce the chloro anion based ionic liquid hybrid material. Then, exchange of the chloride ion with PF_6^- ion completed the synthetic procedure resulting in materials expected to give high values of CO_2 capture.

With the “grafting to” method, the surface of the inorganic material had to be silylated first giving optimal coverage. Therefore conditions for this reaction step were optimized in accordance to solvent polarity, concentration of reactant, and temperature reaction. In Table 5, samples prepared in different reaction conditions are provided with the percentage of coverage accomplished as determined by water vapour adsorption-desorption cycles.

The water desorption method for the determination of the percentage of silanization coverage is described in section 4.1.1. From reaction parameters provided in Table 5 it can be seen that polarity of the solvent plays an important role in the silanization step. For type II SN2 mechanism (expected to be involved in the reaction under consideration), where the reactants are neutral, reactivity is expected to be enhanced by polar solvents. As it can be seen, the grafting extent correlates well with the polarity of toluene and chloroform. However the presence of trace water in toluene solvent is inducing quite different silanization mechanisms (as it will be discussed in section 4.1.1), thus prohibiting the extraction of reliable conclusions about the polarity effect. Also the solvent reflux temperature favours in the direction of a faster diffusion of the reacting silanes into the nanoscale pores of the involved materials. In this work the reaction time applied for all the samples (24 hours) was extended enough and thus it didn’t allow for an investigation of diffusion limitations.

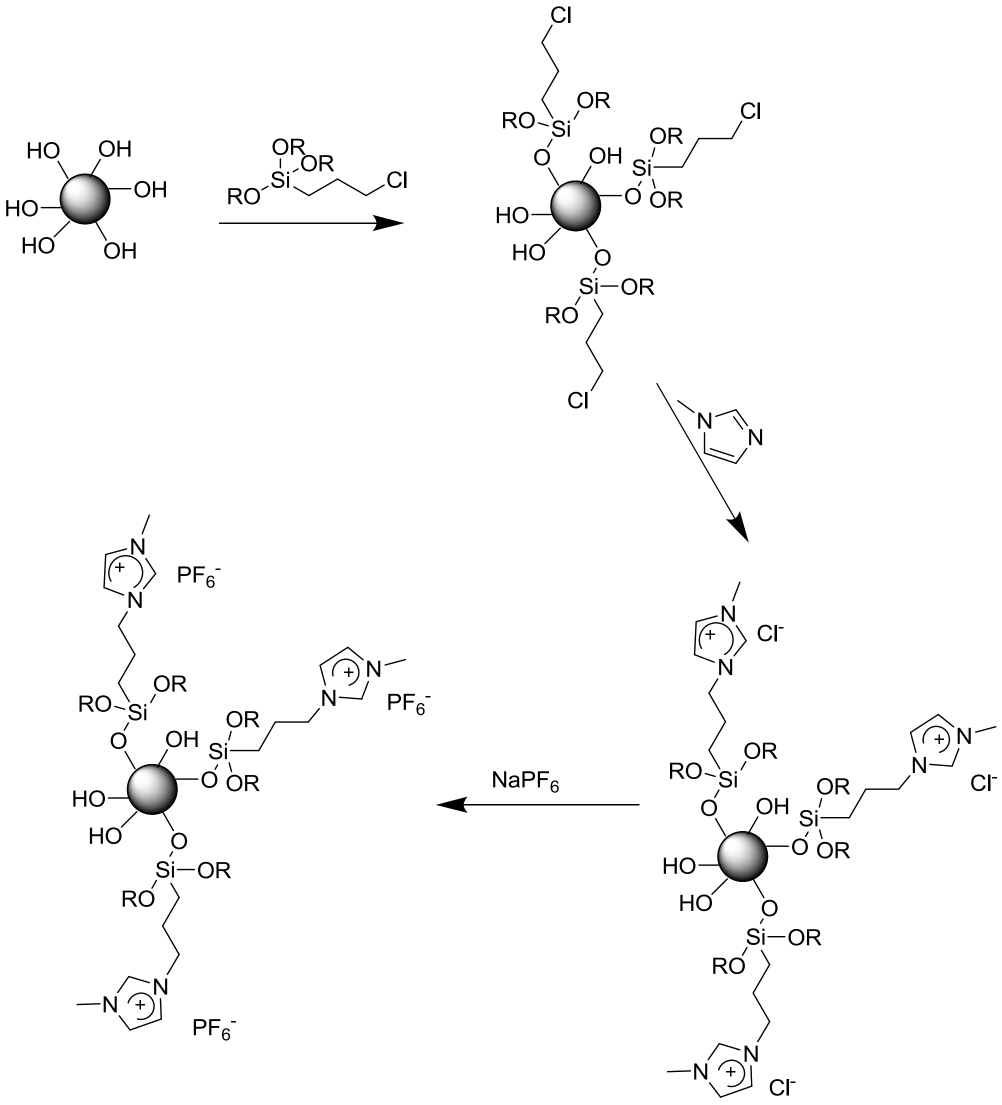

Figure 10. Synthesis of hybrid material with the “grafting to” method

Table 5: Effect of silanization conditions on the grafting extent

Vycor					
Samples	S3	S4	S5	S1	S2
Solvent	CH_2Cl_2	$CHCl_3$	$CHCl_3$	toluene	toluene
Polarity index	3.1	4.1	4.1	2.4	2.4
Reflux temperature (^oC)	40	61	61	110	110
Silane concentration (M)	0.05	0.4	0.4	0.4	0.4
Reaction time (h)	24	24	24	24	24
Sample pretreatment[α]	-	-	+	-	+
% Coverage [b]	16	80	96	41	55

[α] At 180 ^oC and high vacuum (10^{-4} mbar) for 24 h

[b] As determined by water vapour adsorption-desorption cycles

4.1.1 Surface rehydroxylation-Silanization process *(Water adsorption-desorption method, N_2 porosimetry)*

The grafting extent of the silylating agent was determined by water vapour adsorption-desorption cycles. This method is based on the determination, by gravimetric measurements, of the amount of water vapor that is hydrogen bonded with the remaining, after silylation, hydroxyl groups on the surface of the sample assuming one to one hydrogen bond interaction between water and the hydroxyl groups of the surface. This method requires at first samples to be thermally treated at 160 ^{o}C under high vacuum (10^{-4} mbar) for 24 h in order to free the surface silanol groups from absorbed water. Then samples are equilibrated at a water vapor relative pressure P/Po of 0.75 to ensure sufficient coverage of the total pore surface by water molecules. The succeeding desorption step takes place at 35 ^{o}C under high vacuum conditions (10^{-4} mbar) and for a quite extended period of time up to when no alteration of the mass can be detected by the high accuracy microbalance (resolution 0.2 μg).

It should be noted that at this stage the method is not reliable for quantitative estimation of the amount of hydroxyl groups on the surface of the inorganic material. In comparison with other methods such as ^{29}Si cross-polarization magic-angle-spinning NMR (^{29}Si-CP-MAS NMR), isotopic exchange followed by ^{1}H-NMR spectroscopy,[57] thermogravimetric analysis (TG) up to 1273 K,[58] diffuse-reflectance infrared Fourier-transform spectroscopy (DRIFT)[59] and water sorption calorimetry BET analysis,[60] the method seems to underestimates the amount of silanols on the materials surface (see Table 6).

The α_{OH} values (μmol OH/m^2) were calculated from the amount of water h_w (g/g) remaining adsorbed after 24 hours of evacuation at 308 K and 10^{-4} mbar, assuming a one to one interaction/correspondence between the hydroxyl groups of the silanols and the water molecules. The following equation was involved for the calculation:

$$\alpha_{OH} = \frac{10^6 h_w}{M_w A_{BET}} \qquad \text{Eq.20}$$

where Mw = 18 g/mol and A_{BET} (m^2/g) the surface area of the material defined by LN_2 porosimetry.

Xerogel silica[61] and MCM-41,[62] dehydroxylated through thermal annealing at 550 °C and rehydroxylated by refluxing in hydrochloric acid (18.5% w/w) as well as Vycor® dehydroxylated through thermal annealing at 550 °C and rehydroxylated in H_2O_2 (30 % w/w 90 °C) followed by sequential washings with deionized water, were adopted as reference materials to evaluate the validity of the water vapor desorption method applied in this work.

Table 6. Hydroxyl population determined by different analytical methods

	α_{OH} (μmol OH/m^2)								
	Literature							This work	
	Calcination at 823 K				Rehydroxylated			Calcination at 550 °C	Rehydroxylated
	NMR	TG	H_2O sorption	DRIFT	NMR	TG	H_2O sorption	H_2O desorption	
MCM-41	2-4[62], 4-5[63]	2[63]	2.65 [60]	1.5	5	4.4[58]		0.75	
Xerogel silica[61]	2.9	3			8	8.5		0.77	2.6
Vycor®			/1.55[63]		3.8[63]			0.6	1.3

Comparing the surface hydroxyl numbers presented by different authors, one should consider that the results could depend on both the analytical techniques involved and the synthetic procedures of the corresponding mesoporous materials. However as it can be observed (Table 6), in all cases our method underestimates the surface–OH population by a significant factor of the order of 3. The rough assumption of a one to one interaction between the surface silanol groups and water molecules is also adopted in other studies using different techniques[60] and thus it cannot be considered as a reason for the –OH number underestimation. It is rather the hypothesis that all of the hydrogen-bonded water remains on the solid surface under the involved high vacuum conditions (10^{-4} mbar, 35 °C) that generates this large discrepancy. From the several methods applied, DRIFT and ^{29}Si-CP-MAS NMR spectroscopy primarily provide qualitative information about the type of surface silanol groups and isolated terminal ($\equiv SiOH$), hydrogen bonded terminal ($SiOH\cdots{}^{-}OSi$), geminal ($=Si(OH)_2$) and associated geminal groups that can be distinguished,[58] with relative populations depending on heat treatment and rehydroxylation conditions of the material. The most important finding of these studies is that from the different types of surface silanol groups, the isolated terminal (≡SiOH) exhibit the higher affinity towards water[58, 64] and can be regarded as the most capable of retaining hydrogen-bonded H_2O molecules under high vacuum. On the basis of the latter concept we suggest that our method provides an estimate of the more reactive isolated terminal silanols alone, as these are the first silanol groups to be anchored with the silylating agents. Although thermogravimetric analysis up to 1273 K is the more direct and accurate method for the calculation of the surface hydroxyl number, thermal stability limitations prevent the determination of the extent of organic grafting through this approach. Thus we propose the water desorption method as a simple procedure, instead of the more complicated isotopic exchange ^{1}H-NMR and DRIFT spectroscopies, in order to compare materials treated under different conditions and investigate the degree of their hydroxylation and silanization.

Before silanization optimal conditions for rehydroxylating vycor and xerogel silica materials were monitored in order to obtain maximum concentration of surface sinalol groups. Samples were treated in acidic and basic conditions at different time periods and temperatures, while the α_{OH} values (μmol OH/m^2) were calculated from the amount of water h_w (g/g) remaining adsorbed after 24 hours of evacuation at 308 K and 10^{-4} mbar (see Figure 11).

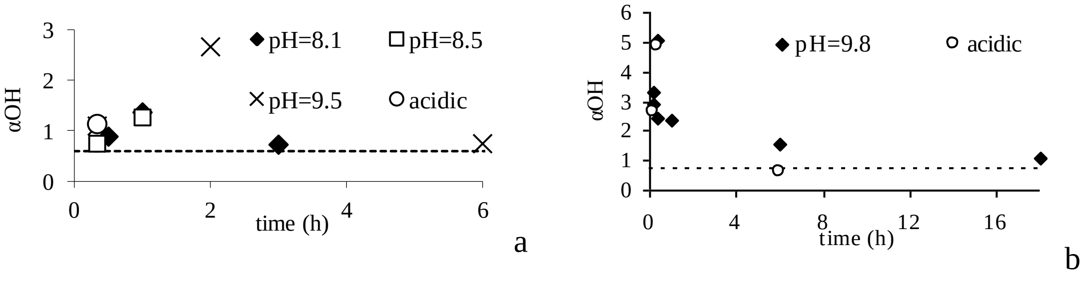

Figure 11. Effect of basic and acidic treatment on the α_{OH} number for (a) Vycor and (b) xerogel silica

Figure 11a shows that in the case of Vycor® and under mild basic hydrolysis conditions (pH = 8.1-9.5) at room temperature, the period of treatment rather than the pH is the most important parameter and the α_{OH} value presented a maximum after about 2 hours of sonication in a NH_3 solution of pH = 9.5, whereas for treatment periods well in excess of 2 hours, extended leaching of the surface led to a moderate population of the hydroxyl groups. Moreover acidic hydrolysis with a solution of

H_2SO_4/H_2O_2 (4/1) for 20 minutes, presented similar to the NH_3 solution (pH = 9.5) efficiency in regenerating surface silanol groups. In the case of xerogel silica and under stronger basic conditions (pH = 9.8), a treatment period of under 0.5 hr suffices for the full rehydroxylation of the surface (Figure 11b), whereas 60 ^{o}C was the optimum treatment temperature. Acidic treatment (H_2SO_4/H_2O_2, 4/1) at 60 ^{o}C, under same periods of time as with the basic conditions, was found less efficient with regards to the capacity to regenerate surface hydroxyls (Figure 11b).

Moreover, the ability of the material to retain its pore structure unaffected during the rehydroxylation procedure was investigated by LN_2 porosimetry for the basic hydrolysis conditions, as it was considered the procedure of choice. As shown in Figure 12a, the N_2 (77 K) isotherms indicate that in moderate pH conditions (pH = 9.5, 2 h) Vycor exhibits higher surface area than the calcinated sample, while from the pore size distribution (Figure 12b) the pore sizes are slightly smaller than the calcinated ones. This is attributed to the fact that the silanol groups resulting from the basic hydrolysis act as adsorption sites during the formation of N_2 monolayer, thus enhancing the surface roughness (fractality). Therefore subsequent multilayer adsorption of nitrogen starts to form at a distance from the pore walls occupied by the silanol groups.

On the other hand, the extended leaching of the Vycor sample treated at pH = 14 for 15 min led to lower surface area and larger pore sizes compared to the calcinated samples, as shown in Figures 12(a) and (b) respectively. In such drastic pH conditions, elimination of certain fine features of the silica framework such as thin necks is unavoidable, leading to pore merging and surface area reduction. The later is confirmed by water adsorption isotherm (Figure 12c), where the water upload of the leached sample at pH = 14 is much less than the calcinated one.

Concerning now the silanization process, water adsorption-desorption cycles were obtained for the samples prepared (see Table 5) in order to have a relevant indication of surface coverage in different reaction conditions. Figure 13 shows the water desorption curves of the Vycor and the silanized samples of Table 5. As observed, sample S5 prepared in $CHCl_3$ and thermally pretreated for 24 h at 453 K and high vacuum (10^{-4} mbar), gave the lowest amount of water remaining at the desorption step of the isotherm, thus indicating optimal silanization conditions. It should be noted that at this stage to ensure sufficient coverage, the involved concentration (mmol/g) of the 3-(chloropropyl)trialkoxysilane per mass of the solid was well in excess of the surface hydroxyl concentration, which was 0.24 mmol/g for the H_2O_2 (30%) treated and 0.47 mmol/g for the fully rehydroxylated Vycor at pH = 9.5 for 2 h.

The grafting extent G_g(%/g) and G_s (%/m^2) were calculated from the water desorption method through the following equations:

$$G_g\% = 100\frac{hg_{vyc} - hg_{sil}}{hg_{vyc}} \qquad G_s\% = 100\frac{hs_{vyc} - hs_{sil}}{hs_{vyc}} \qquad \text{Eq.21}$$

where, hg_{vyc} and hg_{sil} is the mass of water remaining adsorbed per mass of the Vycor® sample and the silanized sample respectively and hs_{vyc} and hs_{sil} is the mass of water remaining adsorbed per the specific surface area of the materials.

The specific surface area of the samples, BET (m^2/g), for the calculation of the G_s (%/m^2) factor was determined by N_2 porosimetry. In Figure 14 the N_2 (77 K) adsorption isotherms of the calcinated Vycor and the silylated samples are provided.

The pore size distribution was extracted from the adsorption step of the isotherm in order to investigate the alterations caused on the size of the bulk of the pores, thus excluding the contribution of existing constrictions in the pore structure such as the narrow pore mouths of the Vycor® pores.

From the isotherms in Figure 14, it can be seen that for the samples prepared in toluene (S1, S2) we have a significant pore volume reduction of the order of 30%, as compared to Vycor®, while samples prepared in $CHCl_3$ (S4, S5) showed a much smaller reduction in the pore volume (8% and 15% respectively). This at first comes in contradiction with the grafting extent of the samples determined by the water adsorption-desorption cycles methods. The values of G_g (%/g) and G_s (%/m^2) for all samples measured are provided in Table 7. The highest silane coverage was achieved in samples prepared in $CHCl_3$ (S4, S5) rather than in toluene (S1, S2) as it would be expected by the reduction in the pore volume with G_g (%/g) values being in the order of 94% and 51% respectively. To elucidate this inconsistency, the carbon content of the samples was calculated out of the grafting extent and it was compared to that determined experimentally by elemental analysis. The results are provided in Table 7 and are in fully agreement indicating that the water desorption method is reliable for the determination of relevant coverage. Thus for the inconsistency between the pore volume reduction and the extent of silanization observed in samples prepared in

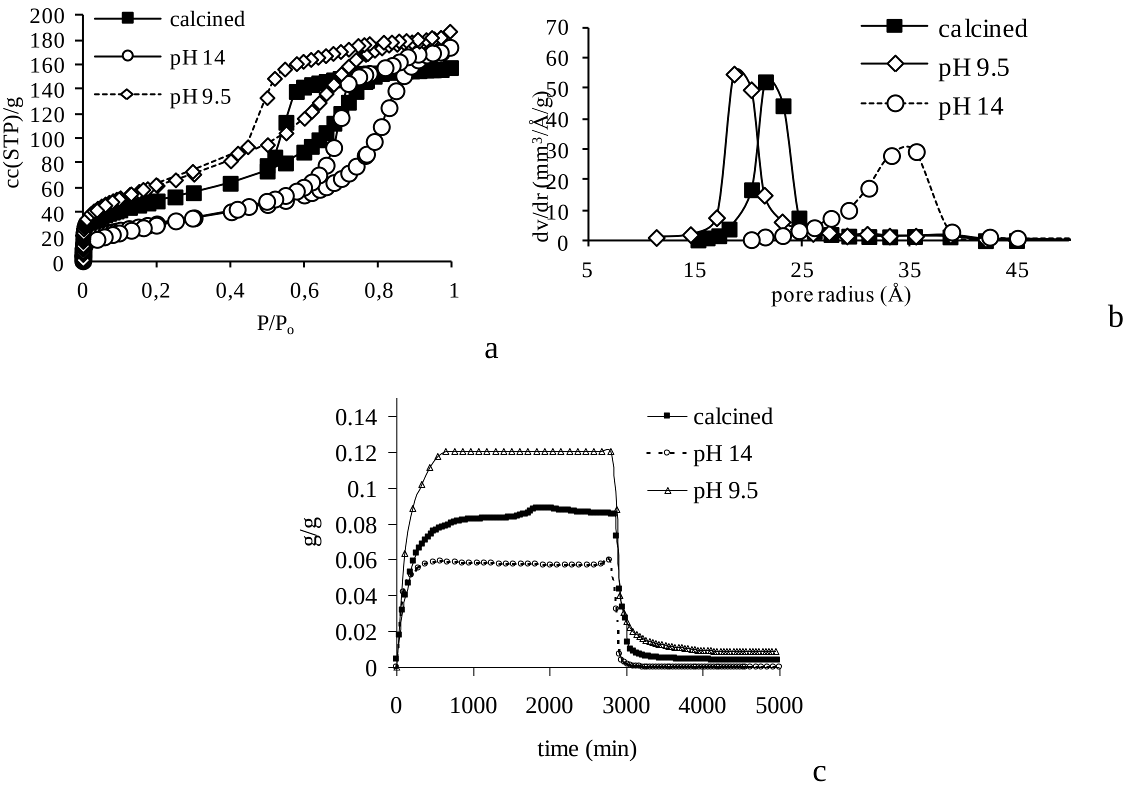

Figure 12. (a) LN_2 adsorption desorption curves, (b) corresponding PSD distributions, and (c) water adsorption desorption cycle

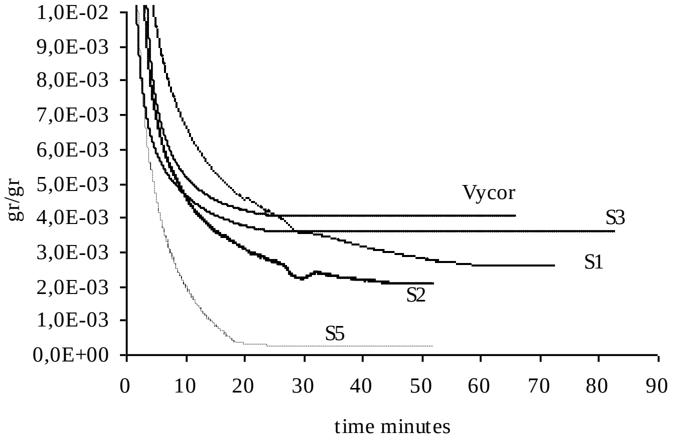

Figure 13. Gravimetric detection of water remaining adsorbed under high vacuum and at 35 °C

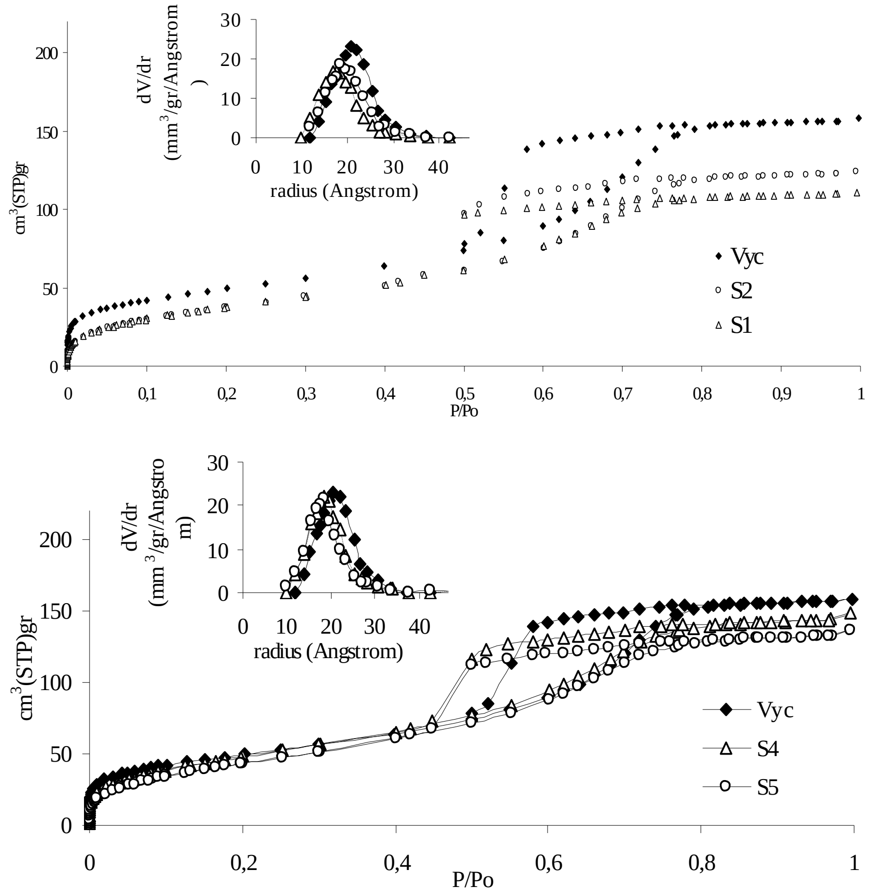

Figure 14. N_2 (77 K) adsorption isotherms and BJH derived pore size distributions after silylation

toluene, it was concluded that residual water present in toluene led to polymerization of the alkoxy-silanes before anchoring to the surface silanols and thus leading to the formation of bulky organosilane entities.

The BJH derived pore size distribution of all samples showed moderate changes in comparison to Vycor® (Figure 14, Table 7). In particular for the toluene prepared samples which showed significant pore volume reduction, it was expected that the pore size distribution would be significantly altered in comparison to Vycor®. The fact that we had a moderate alteration for these samples, led to the conclusion that the bulky entities of polymerized silane formed, as concluded earlier, are not continuous but randomly distributed on the pore surface. Moreover pretreatment of samples at 453 K and high vacuum (10^{-4} mbar) for 24 h prior to silanization, enhanced the grafting extent by a factor of 1.2-1.3 independently of the reaction solvent. This leads to the conclusion that residual water absorbed at the surface of Vycor® hydrolyzes the unreacted alkoxy groups of the already grafted silanes and enhances the polymerization with incoming alkoxy-silanes, creating entities that hinder surface silanols from reacting.

Table 7. Effect of silanization conditions on the grafting extent

		Vycor®	S3	S4	S5	S1	S2
Solvent			CH_2Cl_2	$CHCl_3$	$CHCl_3$	Toluene	Toluene
Polarity Index			3.1	4.1	4.1	2.4	2.4
Reflux temperature ^{o}C			40	61	61	110	110
Silane concentration (M)			0.05	0.44	0.37	0.46	0.44
$Mmol_{Silane}/g_{sample}$			1.8	7.3	7.4	5.5	5.5
Reaction time (hr)			24	24	24	24	24
Sample pre-treatment**			-	-	+	-	+
BET surface area S_{BET}	m^2/g	200	202	179	165	142	142
Total pore volume TPV	ml/g	0.24	0.25	0.22	0.2	0.17	0.19
Mean pore size BJH method	nm	2.00	1.85	1.85	1.85	1.75	1.85
hg_i	g/g	$4.3x10^{-3}$	$3.6x10^{-3}$	$8.6x10^{-4}$	$2.5x10^{-4}$	$2.6x10^{-3}$	$2.1x10^{-3}$
hs_i	g/m^2	$2.2x10^{-5}$	$1.8x10^{-5}$	$4.8x10^{-6}$	$1.5x10^{-6}$	$1.8x10^{-5}$	$1.5x10^{-5}$
Grafting extent G_g / G_s	%		16 / 17	80 / 78	94 / 93	40 / 15	51 / 31
Carbon content*	% C		0.23	1.15	1.35	0.57	0.73
Carbon content experiment	% C		0.31	1.08	-	-	0.8

Regarding the BET surface area (Table 7), it was reduced for samples prepared in toluene and in accordance with pore volume reduction, while for samples prepared in $CHCl_3$ the alteration was insignificant. From the analysis of the data presented, we concluded that the presence of water either in the solvent or on the material's surface plays a crucial role in the silanization process and the pore morphology of the hybrid material prepared. For samples prepared in toluene where residual water was present in the solvent, we had the highest pore volume reduction in the hybrid material prepared, while surface coverage of the silanol groups was only limited to 51% maximum for the pretreated samples where absorbed water on the surface of Vycor® was removed.

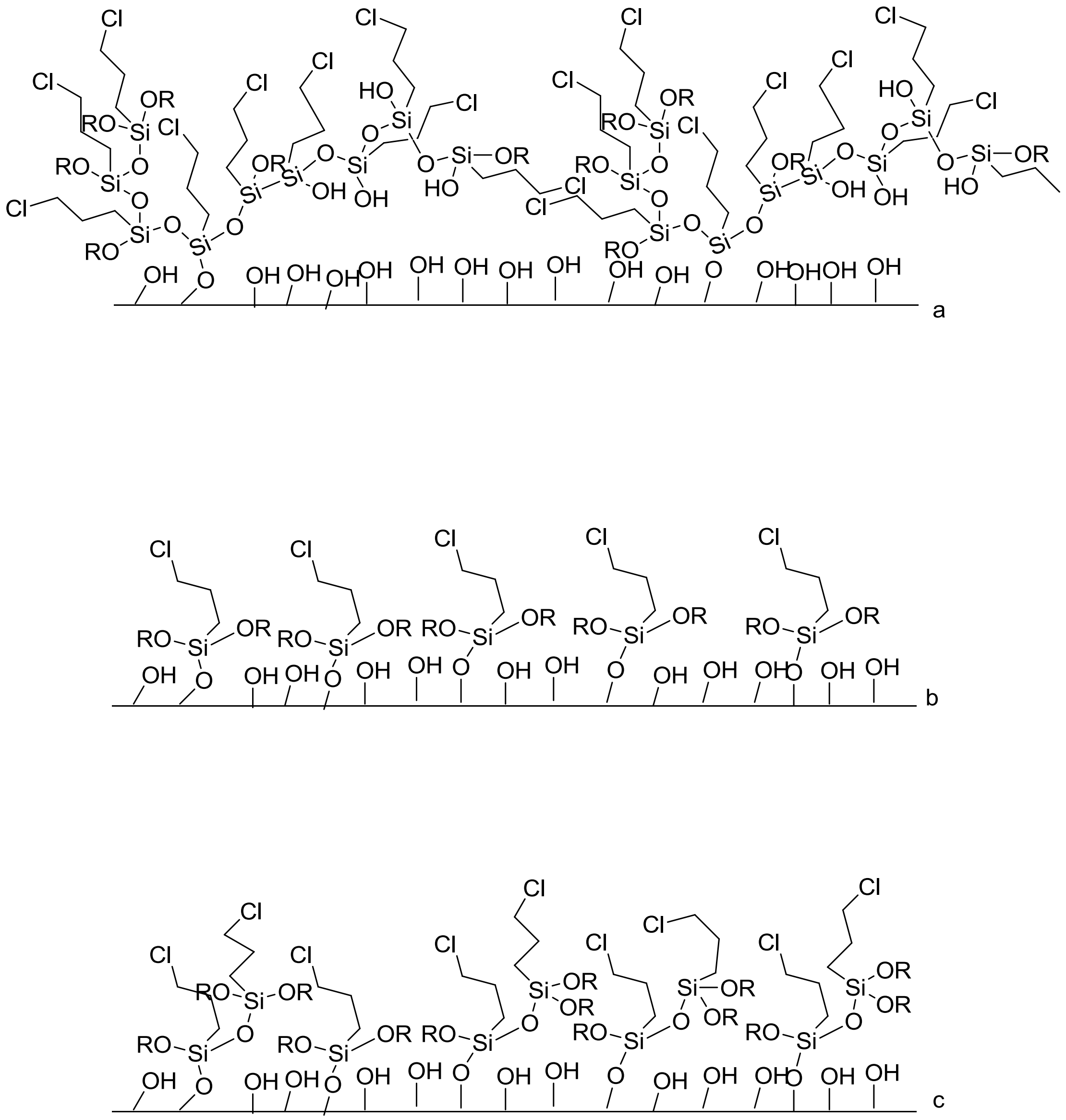

Figure 15. Pore morphology of the silylated samples

In this case we concluded that bulky entities of polymerized alkoxy-silanes are grafted on the surface prohibiting reaction of free silanol groups with incoming alkoxy-silanes due to steric effects (Figure 15a). For samples prepared in dry $CHCl_3$ and thermally pretreated in high vacuum, the highest surface coverage (94%) was obtained, while the sample's pore volume was insignificantly affected leading to the conclusion that we have the formation of a monolayer of grafted silanes (Figure 15b). The presence of absorbed water on the surface of the sample could also lead to limited polymerization prohibiting full cover to an extent of 80% as obtained in the non pretreated sample prepared in dry $CHCl_3$ (Figure 15c).

4.1.2 Surface Analysis by LN_2 porosimetry and SAXS

The pore surface fractality of the hybrid material prepared in deferent silanization conditions was investigated with both N_2 porosimetry and Small-angle X-ray scattering (SAXS). From N_2 porosimetry, the fractal dimension D_s was calculated from the adsorption isotherms by involving the following equation[65]:

$$\ln\left(\frac{V}{V_m}\right) = const \times \tan t + (D_s - 3)\left[\ln\ln\left(\frac{P_o}{P}\right)\right] \qquad \text{Eq.22}$$

where, V_m is the volume of adsorbed molecules in a monolayer at the standard temperature and pressure STP, V is the volume adsorbed at equilibrium pressure P, D_s is the fractal dimension, and P_o is the saturation pressure of the adsorbate. By analyzing the relation between $\ln(V/V_m)$ and $\ln\ln(P_o/P)$, the fractal dimension D_s can be obtained by:

$D_s=S+3$ where $S = d[(\ln(V/V_m))]/d[\ln\ln(P_o/P)]$ Eq.23

In the following Figure 16, the nitrogen adsorption isotherms are expressed as the relation between $\ln(V)$ and $\ln\ln(P_o/P)$.

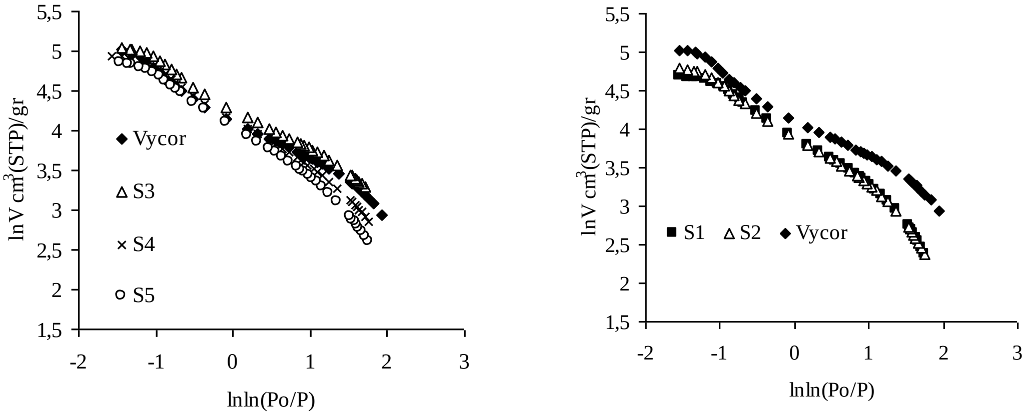

Figure 16. Determination of the fractal dimension from N_2 (77K) isotherms

The slope at the linear region of these curves equals S and the derived D_s values are also presented in Table 8. The calculated fractal dimension of the dry Vycor® ($D_s = 2.46$) was in good agreement with the value defined in a previous work[66] (~2.5) via an experimental procedure involving water adsorption in conjunction with small-angle neutron scattering (SANS). The fractality of the pore surface geometry of the dry Vycor® has already been attributed to open silicate entities emanating from the surface of the Vycor® pores.[67, 68]

Table 8. Extent of grafting and its effect on pore morphology

	Vycor®	S1	S2	S3	S4	S5
Solvent		Toluene	Toluene	CH_2Cl_2	$CHCl_3$	$CHCl_3$
Silane concentration (M)		0.4	0.4	0.05	0.4	0.4
Sample pre-treatment**		-	+	-	-	+
% Amount of grafted Si-OH per gram		41	55	16	80	96
Fractal dimension D_s from adsorption isotherms	2.46	2.37	2.36	2.48	2.41	2.40
Fractal dimension D_s from SAXS data	2.50	2.40	-	2.52	2.44	-

**At 453 K and high vacuum.

The D_s values determined by SAXS were in reasonable agreement with those calculated from the adsorption isotherms (Table 8). The scattering curves from dry Vycor® as well as from the silane grafted samples are illustrated in Figure 17.

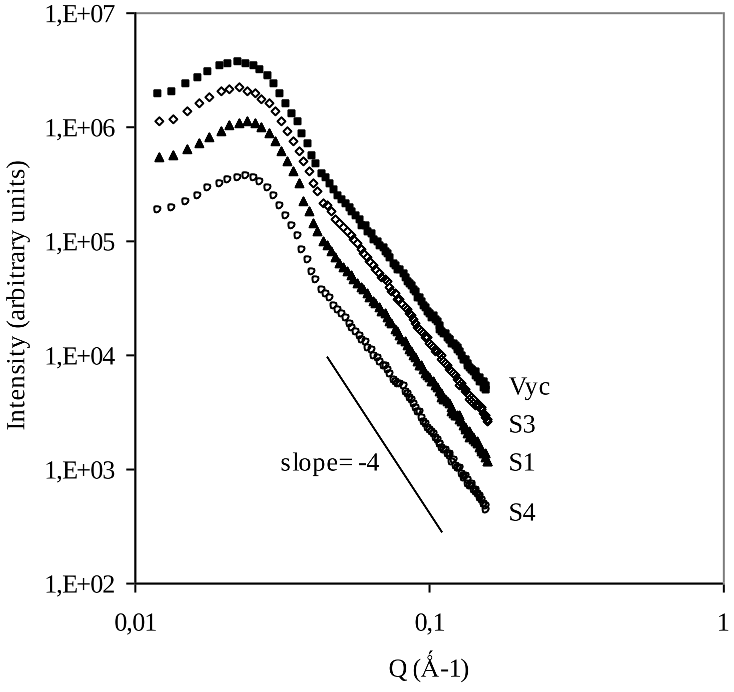

Figure 17. Scattering curves of Vycor® and silylated samples

The surface fractal dimension D_s is calculated from the slope of the scattering curves according to the Bale-Schmidt formula[69]:

$$I(Q) \propto Q^{D_s-6} \qquad \text{Eq.24}$$

where I(Q) is the intensity of the scattered radiation and $Q = 4\pi \sin\theta / \lambda$ is the wave scattering vector, with λ the wavelength and 2θ the scattering angle. SAXS is a well-established technique for obtaining information about the texture of the pore interface. According to the theory, at the high-Q region the intensity decreases asymptotically as Q^{-4} following the so-called Porod's law. When the interfacial boundary is not sharp, deviations from Porod's law behavior may occur which can be explained in terms of a fractal dimensionality according to the Bale-Schmidt formula. If a surface is smooth, $D_S = 2$ (Porod's law). When, however, the surface interface is fractally rough as in the case of many porous materials such as Vycor®, $2 < D_s < 3$. Table 8 shows the values of D_s extracted from the scattering curves of most of the samples under investigation. In the case of dry Vycor®, $D_s = 2.50$, in accordance to previous measurements.[66, 70] Regarding the surface modified samples, S3 [prepared in CH_2Cl_2 and very low concentration of silylating agent (0.05 M)] did not present any alteration of the initial fractal dimension of the dry sample and it showed an insignificant increase, whereas for all the other samples the grafting procedure led to the smoothening of the pore surface geometry. This defractalization was more pronounced in the cases where toluene was used as the grafting solvent (samples S1, S2).

In addition all samples show a pronounced peak at $Q \approx 0.025$ Å^{-1}. It is well known that the small-angle scattering from Vycor® porous glass exhibits a broad peak at the aforementioned position, which has been attributed to spinodal decomposition during the formation process of the glass.[71-75] The location of the peak is also related to the mean pore size of each particular glass, that is, the larger the average pore size the lower the scattering vector where the peak is located. In samples S1 and S4, a slight tendency of shifting the peak towards higher scattering angles is observed. This is in agreement with the isotherm data where a reduction of the pore size was deduced.

4.1.3 Pore characteristics of the IL modified Vycor®-([spmim][PF$_6^-$]/Vycor®)

Silylated Vycor samples were further reacted with methylimidazole in order to synthesize with the “grafting to” method (Figure 10) the composite ionic liquid materials [spmim][Cl$^-$]/Vycor®. Ion exchange of [Cl$^-$] ions with [PF$_6^-$] was followed in order to produce the desired hybrid material [spmim][PF$_6^-$]/Vycor®. Pore volume reduction in comparison to Vycor® and the silylated precursor samples was monitored by N_2 porosimetry while BET surface area was calculated both by N_2 (77 K) adsorption isotherms and CO_2 adsorption at 273 K. Results are provided in Table 9.

Given that nitrogen shows low to non detectable adsorption in PF6$^-$-imidazolium cation based ionic liquids,[76] nitrogen porosimetry can be considered reliable for the determination of pore characteristics such as total pore volume reduction and BET surface area.

Table 9. Pore characteristics of the IL modified Vycor®

		Precursor		Precursor		Precursor	
Samples	Vycor®	S1	S6	S5	S8	S4	S7
Trialkoxysilyl-Grafting solvent		Toluene		$CHCl_3$		$CHCl_3$	
Sample pretreatment*		–		+		–	
% Silylation surface coverage		41		96		80	
BET m^2/gr	175	142	96	165	147	179	125
Total pore volume ml/gr	0.242	0.170	0.12	0.206	0.2	0.223	0.2
Pore volume reduction		compared to Vycor® 30%	compared to S1 29%	compared to Vycor® 15%	compared to S5 3%	compared to Vycor® 8%	compared to S4 10%
BET reduction		19%	32%	6%	11%		24%
Fractal dimension D_s	2.46	2.37	2.34	2.40	2.38		2.40
BET from CO_2 m^2/gr	203		119				142

* At 180 °C and high vacuum.

Deviations to higher values obtained by CO_2 adsorption isotherms indicate the presence of ionic liquid on the surface of the material prepared. Sample S6 (prepared from the silylated sample S1 in toluene) showed a significant reduction in total pore volume and BET surface area in the order of 29% and 32% respectively (Figure 18, Table 9) as compared to the precursor. In this case and in accordance with the morphology of the precursor material S1 as described in Section 4.1.1, it is concluded that a polymerized in bulky entities ionic liquid is formed and grafted on the surface of Vycor®. In contrast to pore volume reduction, the pore size distribution (Figure 18) remained unaffected. The later is attributed to the not continuous character of the grafted silane layer.

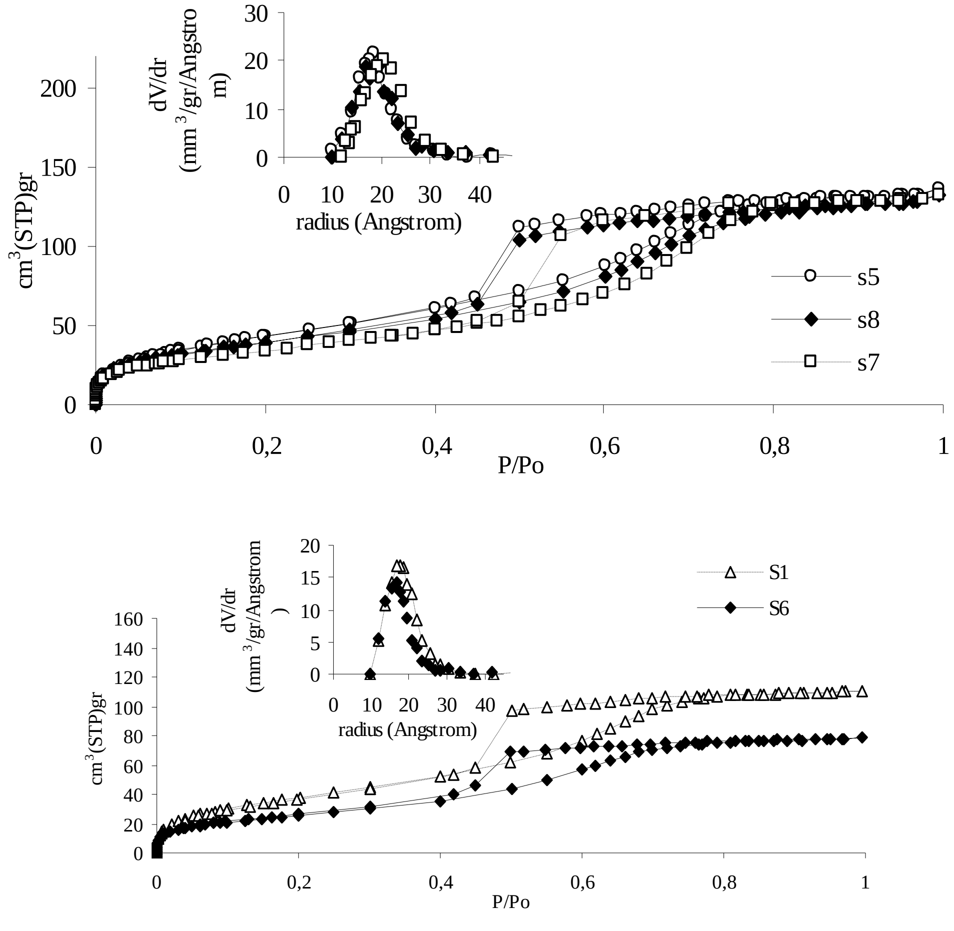

Figure 18. N_2 (77 K) adsorption isotherms and BJH derived pore size distribution

On the contrary, sample S8 presented insignificant alteration on the pore volume and BET surface as compared to its organosilane-grafted precursor S5 (prepared in dry $CHCl_3$ with water removed from the sample's surface prior silanization). As it was concluded in Section 4.1.1, in this case polymerization of the alkoxy-silanes was prohibited at the surface of the precursor S5, thus leading to the formation of a monolayer of ionic liquid grafted on the surface of sample S8 unable to significantly affect the total pore volume. Sample S7 showed an intermediate alteration in pore volume in the order of 10% and in accordance to its precursor's S4 pore morphology, as showed in section 4.1.1. S4 was prepared in dry $CHCl_3$ while water was not removed from the sample's surface prior silanization leading to partial polymerization.

The BET surface area of Vycor® and samples S6, S7, extracted from the CO_2 isotherm was 203, 119 and 142 m^2/g respectively (Table 9). CO_2 produces a 16% higher BET value for Vycor® as compared to the value obtained from the N_2 (77 K) isotherm (Table 9), whereas for sample S6 the increase was much higher (24%) indicating the presence of an ionic liquid phase that adsorbs enhanced amount of CO_2 compared to nitrogen. For the calculations the isotherms were reconstructed in terms of CO_2 relative pressure (Vapor Pressure of CO_2 at 237 K = 33 bar) and the BET method was involved to calculate the specific surface area of the samples by adopting an occupation area of 18.7 $Å^2$ for the adsorbed CO_2 molecule at 273 K.[77] The adsorption isotherms of the developed hybrid ([spmim][PF_6^-]/Vycor®) samples at 273 K are presented in Figure 19 in comparison with these of the pristine Vycor® and the bulk ionic liquid [bmim][PF_6^-] synthesized in our lab.

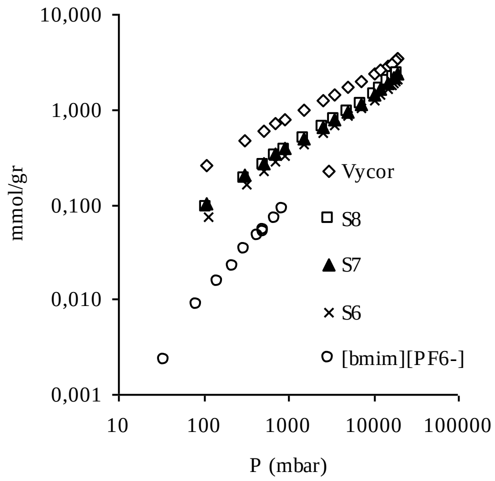

Figure 19. CO_2 isotherms at 273 K (Axes in logarithmic scale)

4.1.4 Loading of IL on hybrid material – CO_2 adsorption kinetics at 273 K

For the determination of IL loading on hybrid material, the well known solution for the transient sorption curve for slabs[21] was appropriately modified to incorporate two diffusivity constants characterizing the two different mechanisms of diffusion occurring simultaneously in the hybrid [spmim][PF_6^-]/Vycor® samples: diffusion in nanopores (Vycor®) and dissolution-diffusion in the ionic liquid phase [bmim][PF_6^-].

The derived expression is:

$$\frac{m_t}{m_\infty} = 1 - A\frac{8}{\pi^2}\sum_{n=0}^{\infty}\frac{1}{(2n+1)^2}\exp\left(\frac{-D_a(2n+1)^2\pi^2 t}{4\ell_a^2}\right) - (1-A)\frac{8}{\pi^2}\sum_{n-0}^{\infty}\frac{1}{(2n+1)^2}\exp\left(\frac{-D_b(2n+1)^2\pi^2 t}{4\ell_b^2}\right) \qquad \text{Eq.25}$$

where A the mass fraction of the ionic liquid phase in the total material, D_a, D_b (cm^2/sec), the diffusivity constants of the ionic liquid and Vycor® respectively and 2ℓ (cm) the slab thickness.

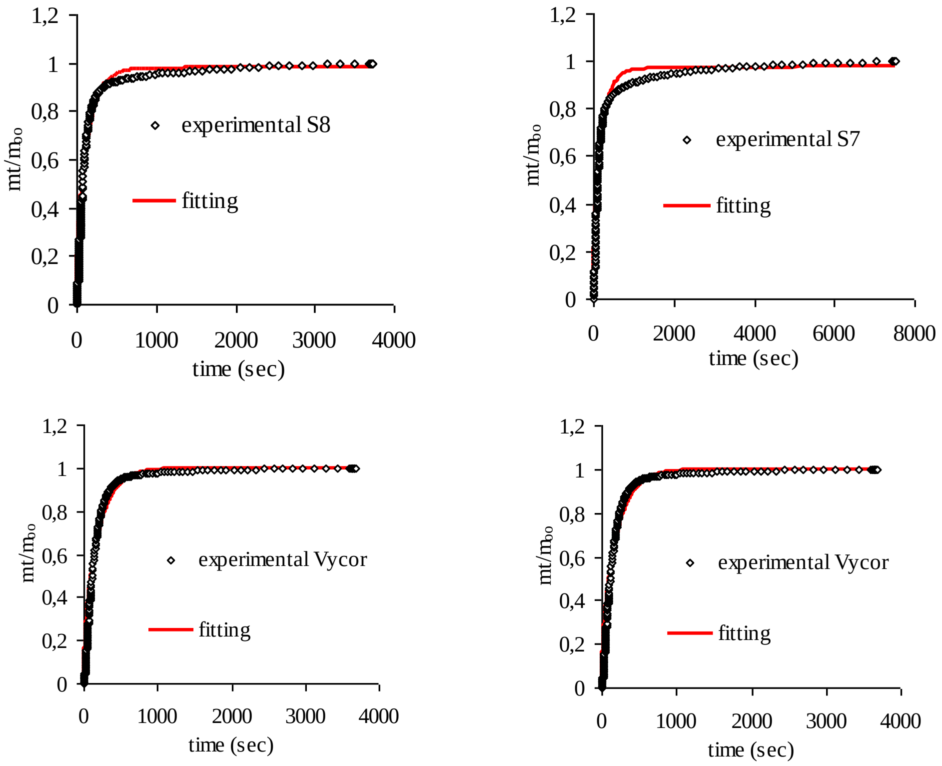

Figure 20. CO_2 adsorption transient curves at 273 K and corresponding fitting curves

The apportionment of the contribution of the two diffusion constants, expressed as *A* mass fraction, was defined by fitting the experimental CO_2 adsorption transient curve of the prepared hybrid material with the modified solution using the Lavenberg–Marquardt algorithm and adopting the experimentally calculated diffusivity constants of the bulk ionic liquid [bmim][PF_6^-] synthesized in our lab and the pristine Vycor® for identical pressure steps during adsorption. The diffusivity constants D_a, D_b, were calculated from the corresponding [bmim][PF_6^-] and Vycor® CO_2 adsorption transient curves using the equation:

$$\frac{m_t}{m_\infty} = 1 - \frac{8}{\pi^2}\sum_{n=0}^{\infty}\frac{1}{(2n+1)^2}\exp\left(\frac{-D(2n+1)^2\pi^2 t}{4\ell_a^2}\right) \qquad \text{Eq.26}$$

The experimental with their calculated fitting curves are illustrated in Figure 20, whereas the defined IL mass fraction values A% for the pressure steps examined are presented in Table 10 in comparison with those derived by thermogravimetric analysis (TGA).

Table 10. IL loading derived by TGA and CO_2 transient curves

Pressure step (mbar)	**0-100**	**100-300**	**300-500**	**500-700**	**700-900**
$D_a/4\ell^2$(sec^{-1})	3.85E-06	5.89E-06	7.13E-06	8.09E-06	8.09E-06
$D_b/4\ell^2$(sec^{-1})	4.90E-04	7.10E-04	7.30E-04	7.30E-04	8.00E-04
			A%		
S6	7.5	7.1	7.4		
S7 (TGA 3.54%)	3.6	3.5	3.6	3.9	3.6
S8	3.5	2.7	2.5	2.2	3.3

For sample S7, an IL loading value of 3.54% was determined by TGA (Figure 21) and is in full agreement with the corresponding values determined by the CO_2 transient curves method (Table 10). Sample S6, with the lowest extent of grafting, gave the highest IL loading. The later enhances the already derived, by N_2 porosimetry, conclusion (Section 4.1.3) that a polymerized ionic liquid is grafted on the surface.

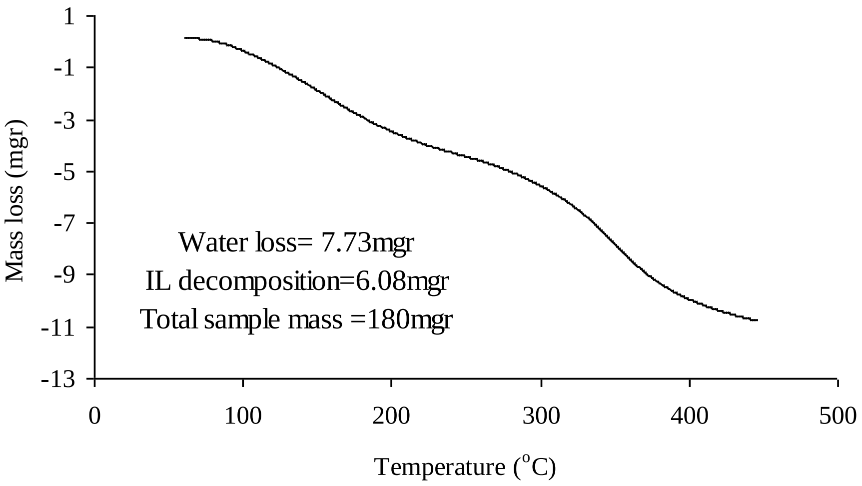

Figure 21. TGA curve of the hybrid sample S7

4.1.5 Thermal Stability of grafted Ionic Liquid

A thermolysis study of dialkylimidazolium salts reports that the decomposition is a SN2 process that results in a mixture of *N*-alkylimidazoles and 1-alkylhalides.[78] Ohtani *et al.*,[79] studied the thermal decomposition behaviours of several imidazolium based ionic liquids by pyrolysis-gas chromatography. They observed that the thermal decomposition proceeds through C-N bond cleavage (Figure 22).

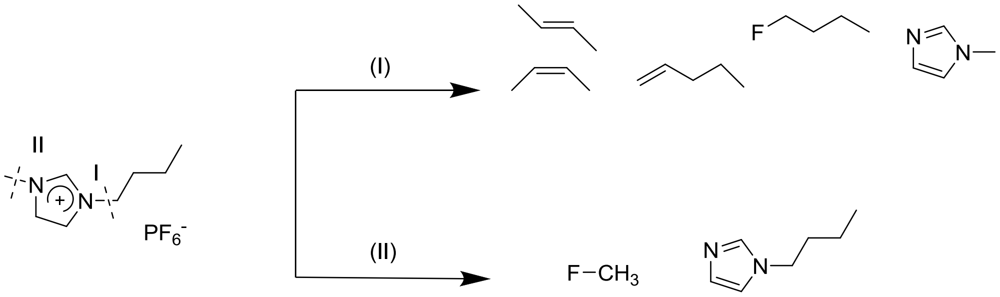

Figure 22. Thermal decomposition pathways of 1-butyl-3-methylimidazolium hexafluorophospate

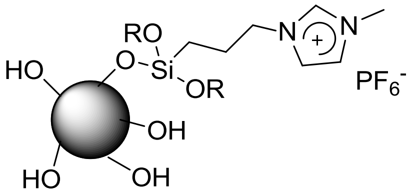

Figure 23. Grafted [spmim][PF$_6^-$] ionic liquid

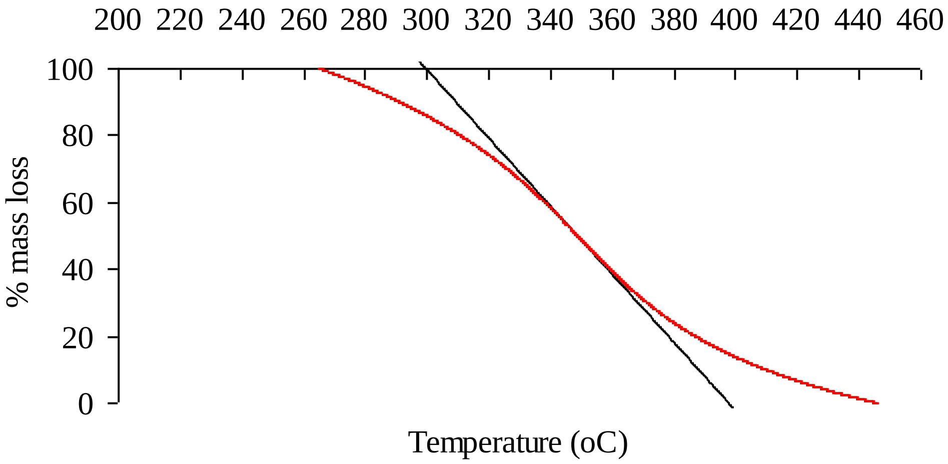

Figure 24. Tangent method for the determination of the grafted [spmim][PF$_6^-$] IL decomposition temperature

Based on the former, we assume that grafted [spmim][PF$_6^-$] (Figure 23) thermally decomposes through a similar path. For the grafted [spmim][PF$_6^-$], a decomposition temperature of the order of 300 °C was determined by TGA as shown in Figure 24.

4.1.6 Pore characteristics of the IL modified MCM-41 - ([spmim][PF_6^-]/MCM-41)

MCM-41 with pore sizes of 2.3 nm and 3.3 nm respectively were modified with the “grafting to” method in order to prepare the [spmim][PF_6^-]/MCM-41 hybrid material. To avoid polymerization during the silanization step, samples were thermally pretreated in high vacuum while dry $CHCl_3$ was used as a solvent in order to obtain maximum surface coverage (see Section 4.1.1). As is clear from the nitrogen porosimetry results (Figure 25), the pores of the MCM-41, having a mean size of 2.3 nm, were totally occupied by the grafted [spmim][PF_6^-] ionic liquid face. The upward step of the LN_2 isotherm at a relative pressure close to unity, observed for both the Supported Ionic Liquid Phase (SIPL) and the MCM-41, is attributed to nitrogen condensation in the interparticle void volume of the solid support.

For MCM-41 with larger pores (3.3 nm), the blockage of the void space was significant but not complete (Figure 25b). Again the upward step of the LN_2 isotherm at relative pressure close to unity is attributed to phenomena of capillary condensation in the interparticle void volume of the solid.

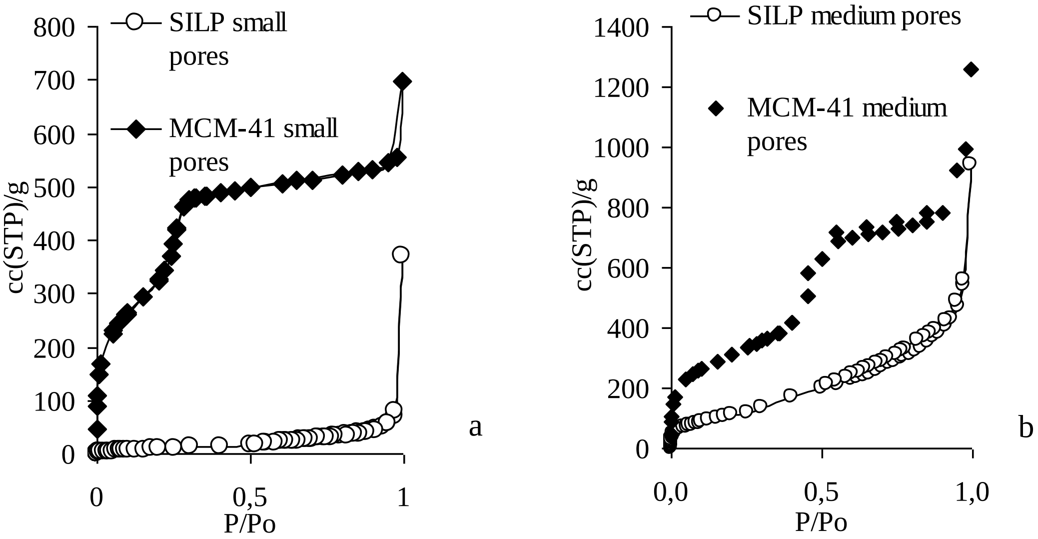

Figure 25. LN_2 (77 K) isotherms for MCM-41 and SILP: (a) 2.3 nm, (b) 3.3 nm.

4.1.7 CO_2 and CO absorption in the Bulk Ionic Liquid Phases – Selectivities

In Figure 26 we present the results of CO_2 and CO absorption at different temperatures in the three bulk ionic liquid phases examined in this work. Gas absorption properties were for the first time studied at the temperature of 273 K, which is about 6 K below the melting point of the bulk ionic liquid [bmim][PF_6^-]. However, after considering several studies describing the difficulty to obtain stable [bmim][PF_6^-] crystals by cooling, as solidification often results in glass formation,[80, 81] we cannot claim that at this temperature the ionic liquid was in its solid state.

As it can be observed, independently of the IL physical state, the carbon dioxide follows the exothermic character of solvation in both the commercial [bmim][PF_6^-] and the synthesized [spmim][PF_6^-]. For the three bulk ionic liquid phases examined, the Henry constants ($\overline{H}$ bar/mol fraction) were determined from the CO_2 absorption isotherms (Table 11). Calculations involve the determination of the slope of the line that arises by plotting the moles of absorbed CO_2 per mole of IL versus pressure where $\overline{H}$ =1/slope.

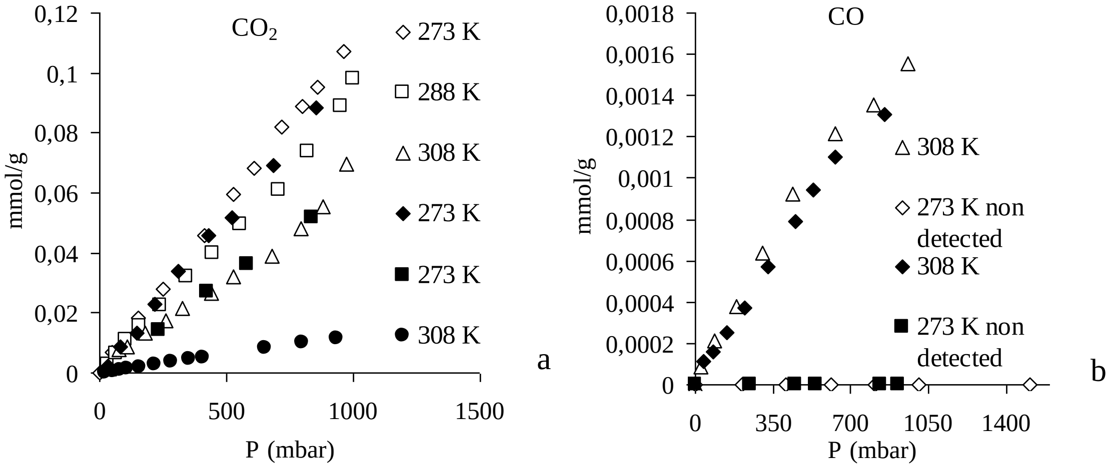

Figure 26. (a) Open symbols: commercial [bmim][PF_6^-], filled rhombs: synthesized [bmim][PF_6^-], filled rectangles-filled cycles: synthesized [spmim][PF_6^-]. (b) Open symbols: commercial [bmim][PF_6^-], filled rhombs: synthesized [bmim][PF_6^-], filled rectangles: synthesized [spmim][PF_6^-].

Table 11. Henry constants of CO_2 absortion in bulk IL

Ionic Liquid	Henry constants ($\overline{H}$ bar/mol fraction)		
	273K	288K	308K
Commercial [bmim][PF_6^-]	31.9	40.3	63
Synthesized [bmim][PF_6^-]	33.8		
Synthesized [spmim][PF_6^-]	39.2		

The Henry constants ($\overline{H}$ bar/mol fraction) correlated positively with temperature. The $\overline{H}$ values of 31.9, 40.3 and 63 bar/(mol fraction) calculated for the commercial ionic liquid at 273, 288 and 308 K respectively, were in good accordance with those often encountered in literature.[82] The $\overline{H}$ value of the synthesized [bmim][PF_6^-] (33.8 bar/mol fraction) at 273 K, deviated no more than 6% from the value of the commercial material and this signifies the purity of the synthesized ionic liquid phase. It should be noted that the absorption results presented in Figure 26a, were normalized over the entire mass of the bulk ionic liquid absorbents. However, in the case of the synthesized alkoxysilyl-IL [spmim][PF_6^-] and in order to derive reliable conclusions, absorption results should be normalized per the net mass of the 1-propyl-3-methylimidazolium-hexafluorophosphate [pmim][PF_6^-] in the alkoxysilyl-IL molecule, since the silyl part is not expected to have any remarkable contribution on the CO_2 absorption capacity. By applying a mass fraction (silyl/[pmim][PF_6^-]) of 0.45 as calculated from the stoichiometry of the molecule and with the assumption that hydrolysis of the silyl part of the silylated IL was completely avoided under the involved conditions of inert atmosphere and high vacuum, we derived an $\overline{H}$ value of 39.2 bar/(mol fraction) at 273 K for the synthesized alkoxysilyl-IL. There are two possible reasons for the lower absorption capacity of the silylated-IL.

The first has to do with the number of carbon atoms in the alkyl chain of the imidazolium ring, that is 3 for the [spmim][PF_6^-] and 4 for the bulk ionic liquid [bmim][PF_6^-]. Although several studies revealed that only the anionic part of the IL significantly affects the CO_2 solubility,[83] changes in the imidazolium cation involving alkyl groups were also proved to have a relatively moderate influence on the gas solubility properties. In fact the longer alkyl chains usually resulted to slightly better CO_2 absorption capacity in the ionic liquid but there are not sufficient explanations about this issue.[84, 85] In our case the effect of the carbon atom number seems to be more enhanced, as the Henry constant ratio for a difference of one carbon number in the alkyl chain was 0.87 compared to ratios of 0.94 often found in literature[84] for differences of 2 up to 4 carbon atoms. Based on this fact we can claim that the lower CO_2 solubility value results from the presence of the silyl group attached to the alkyl chain of the imidazolium ring. Recent MD simulations indicated that CO_2 organizes strongly about the $[PF_6^-]$ anion in a "tangentlike" configuration that maximizes favorable interactions[83] which enhance its solubility. The presence of the silyl group may lead to a modest loss of organization of the anion and the CO_2 around the cation as had also occurred in other studied cases, where the acidic hydrogen on the C2 carbon of the [bmim] cation was replaced with a methyl group.[83]Concerning the CO solubility (Figure 26b), this was detectable just for the commercial and the synthesized $[bmim][PF_6^-]$ at 308 K. The calculated $\overline{H}$ values of 2158 and 2202 bar/(mol fraction) respectively were in good accordance with those found in the work of Kumelan *et al.*,[86] and deviated positively by approximately 100 % from those found in the studies of Jacquemin *et al.*[87] Interesting enough is that for the ionic liquid $[bmim][PF_6^-]$ at 273 K, the CO absorption was undetectable producing negative erroneous values for the amount absorbed. Thus the CO_2/CO selectivity rises from the value of 40 at 308 K to infinite at 273 K. Moreover in both of the aforementioned studies the calculated Henry constant $\overline{H}$ values for CO practically did not depend on temperature. More specifically, Kumelan even had a negative correlation as it also holds in our case, showing that the amount absorbed increases with temperature. This different solvation behavior of the carbon monoxide has been already emphasized in several studies by the calculated zero enthalpy of solvation compared to the negative values calculated for the carbon dioxide and the other investigated gases.[87] This indicates that the crossed gas–ionic liquid molecular interactions are of different nature in CO and in CO_2. As will be shown in the following sections, independently of the temperature, the examined ionic liquid under extreme confinement into the small pores of the MCM-41 supports was in its solid state. This implies for enhanced IL stability and infinite CO_2/CO selectivity even at elevated temperatures rendering the developed SILP systems potential candidates for PSA applications.

4.1.8 Adsorption of CO_2 and CO on the pristine supports and absorption in the SILP systems

In Figures 27 and 28 we present respectively the obtained CO_2, CO isotherms for the small pore size (2.3 nm) MCM-41 and the relevant supported ionic liquid system (SILP). As we have shown in Section 4.1.6 from the nitrogen porosimetry results, the pores of the MCM-41, having a mean size of 2.3 nm, were totally occupied by the developed [spmim][PF_6^-] ionic liquid phase. Based on this it can be stated that the further described CO_2 and CO absorption capacity of the developed SILP is only related to the inherent solvation properties of the [spmim][PF_6^-] phase that fully occupied the pores of MCM-41. This is the reason we adopted the term absorption for the SILP systems. As an exception to this statement it is noted that the higher CO_2 amount absorbed in the SILP at the low-pressure region and the relevant curvature in the absorption curve (Figure 27), compared to this in the bulk [bmim][PF_6^-], arise as a result of the contribution of the external surface area of the support particles. On the other hand, the CO_2 absorption capacity at higher pressures, above 5 bars, appears artificially lower due to the normalization over the entire mass of the hybrid SILP material. The entire mass of the hybrid material comprises the mass fraction of the MCM-41 support that has negligible contribution to the CO_2 uptake at high pressures.

An interesting feature is that the CO_2 absorption in the SILP system (Inset Figure 27) did not follow the exothermic character observed for the commercial ionic liquid [bmim][PF_6^-] (Section 4.1.7). Indeed the isotherms obtained at two quite different temperatures seem to come in convergence and their slight difference could lie within the accuracy limits of the microbalance setup, as suggested by the error bars. However we can still note the significant contribution of the support external surface at low CO_2 pressures and the low temperature (273 K) and the higher CO_2 solubility at the higher temperature (308 K) for pressures above 5 bars.

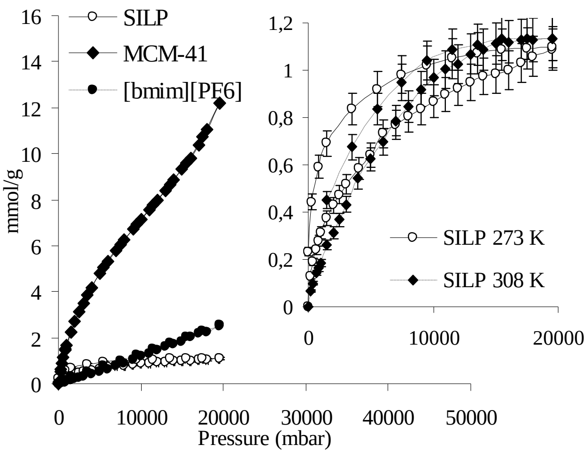

Figure 27. CO_2 isotherms at 273K. Inset: CO_2 absorption in the SILP (MCM41-2.3 nm) at different temperatures.

This inversion of the CO_2 solubility dependence on temperature, observed for the SILP system was a first indication that the developed ionic liquid [spmim][PF_6^-] phase under extreme confinement was in a different physical state from the bulk liquid. A possible existence of crystallinity in the developed ionic liquid may be responsible for the higher amount of CO_2 dissolved at the higher temperature as expected besides the dissolution dependence on temperature for solids. Supporting discussions on that, in relation with the results of XRD and DSC analysis are found in the following section 4.1.9.

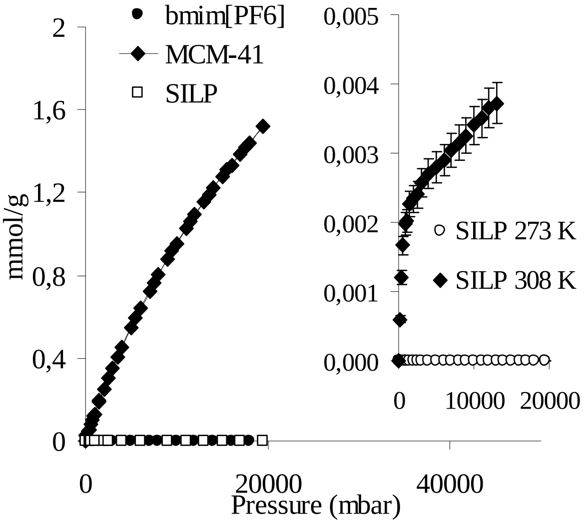

Figure 28. CO isotherms at 273 K. Inset: CO absorption in the SILP (MCM41-2.3 nm) at different temperatures.

Finally the CO_2/CO selectivity at 273 K for the SILP and the ionic liquid [bmim][PF_6^-] was infinite as a result of the zero CO solvation and for this reason it is not included in the selectivity plots (Figure 29).

At 308 K and for the SILP system, CO_2/CO selectivity increases with pressure up to 300. For pressures up to 1 bar the SILP CO_2/CO selectivity values were in the order of 100 and about double from those of the bulk ionic liquid [bmim][PF_6^-]. This again indicates for different solvation properties related to the different physical state of the developed [spmim][PF_6^-] phase under extreme confinement into the pores. The SILP system developed on the MCM-41 3.3 nm support gave also a higher amount of CO_2 absorbed at low-pressures (Figure 30), compared to that in the bulk [bmim][PF_6^-], attributed to contribution of the external surface area of the support particles.

In contrast to the SILP developed in the support with the smaller pores of 2.3 nm, the CO_2 adsorption in this case followed the usual exothermic trend (inset Figure 30), emphasizing the fact that after the silane grafting and sequential treatment with methylimidazole and anion exchange with PF_6^-, there must still exist a void pore space that significantly contributes to the CO_2 uptake and defines the characteristics of the adsorption isotherm.

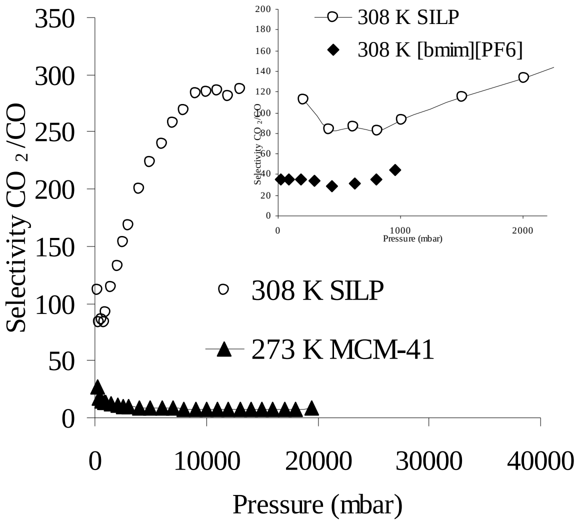

Figure 29. CO_2/CO selectivity vs pressure

Despite this explanation, this exothermic character of the CO_2 adsorption could also be attributed to the probability that the developed into the larger pores [spmim][PF_6^-] phase does not crystallize and retains the absorption characteristics of the bulk liquid

(IL). However, as it will be shown in the following section, this statement does not hold.

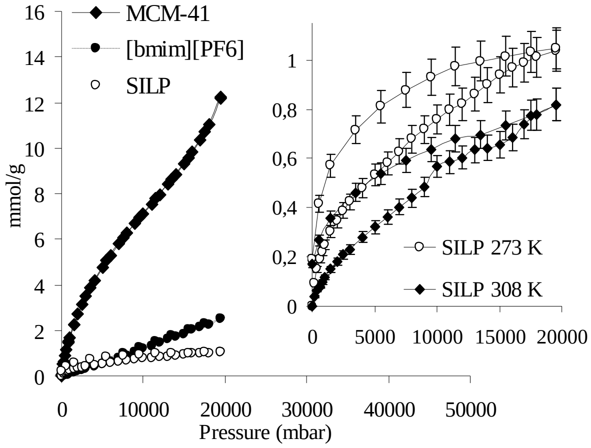

Figure 30. CO_2 isotherms at 273 K. Inset: CO_2 absorption in the SILP (MCM41-3.3nm) at different temperatures.

What arises as a stronger evidence for the persistence of an open pore space is that the CO adsorption (Figure 31) was detectable even at 273 K, something that was observed neither for the bulk IL nor for the SILP developed on the 2.3 nm support. Interesting enough is also that the SILP developed in the 3.3 nm MCM-41 support exhibited a much lower CO_2 adsorption capacity than the one developed in the small pores support. Since the deposition of the IL phase starts from a surface reaction and proceeds to the bulk of the pore, Ionic Liquid loading should be related to the initial specific surface area of the supports.

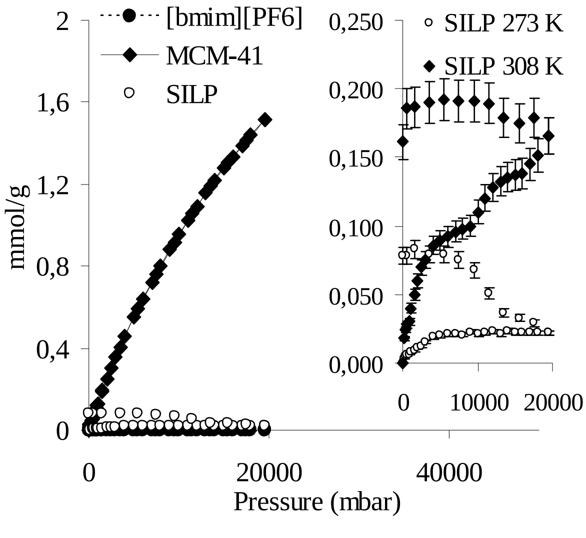

Figure 31. CO isotherms at 273 K. Inset: CO absorption in the SILP (MCM41-3.3nm) at different temperatures.

Indeed the BET surface area is 1205 and 1120 m^2/g for the 2.3 and 3.3 nm MCM-41 respectively and this justifies a higher IL loading into the smaller pores support. The CO adsorption capacity increases with temperature (Figure 31), as was the case for the bulk [bmim][PF_6^-]. Interesting enough is the extended hysteresis of the CO even at very low pressures that can be attributed to diffusion limitation phenomena during absorption. This means that although the allowed experimental time for equilibration was 10 hr, the absorption isotherm points were still obtained in the transient state of each pressure increment due to the extremely slow rate of diffusion.

In what concerns the performance of the developed SILP, the CO_2/CO selectivity had the value 50 at 273 K (Figure 32) that is by far superior to the performance of the pristine 3.3 nm MCM-41 support, which gave a CO_2/CO selectivity of 8. However, the incomplete coverage of the pores void volume considerably suppressed the separation performance that was about 5 at 308 K, when compared to the value of 280 obtained for the SILP developed on the small pore size support (Figure 32).

In the case of Vycor® the extent of pore blockage was negligible and no enhancement of the CO_2/CO separation capacity of the SILP compared to the pristine support was observed.

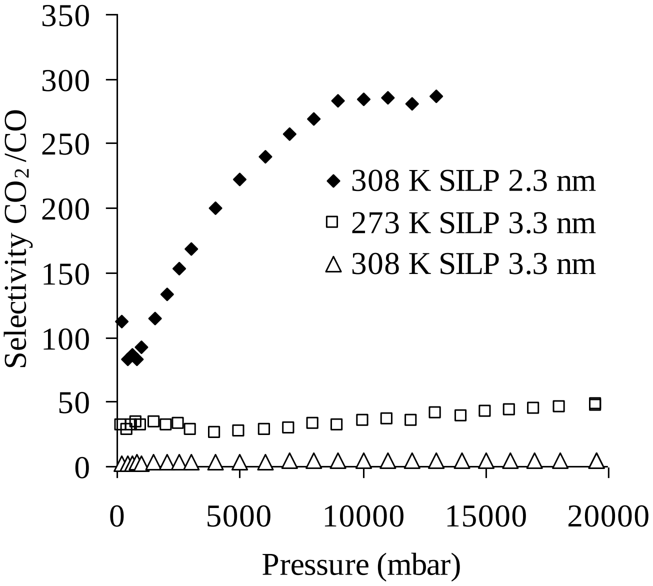

Figure 32. CO_2/CO selectivity vs pressure

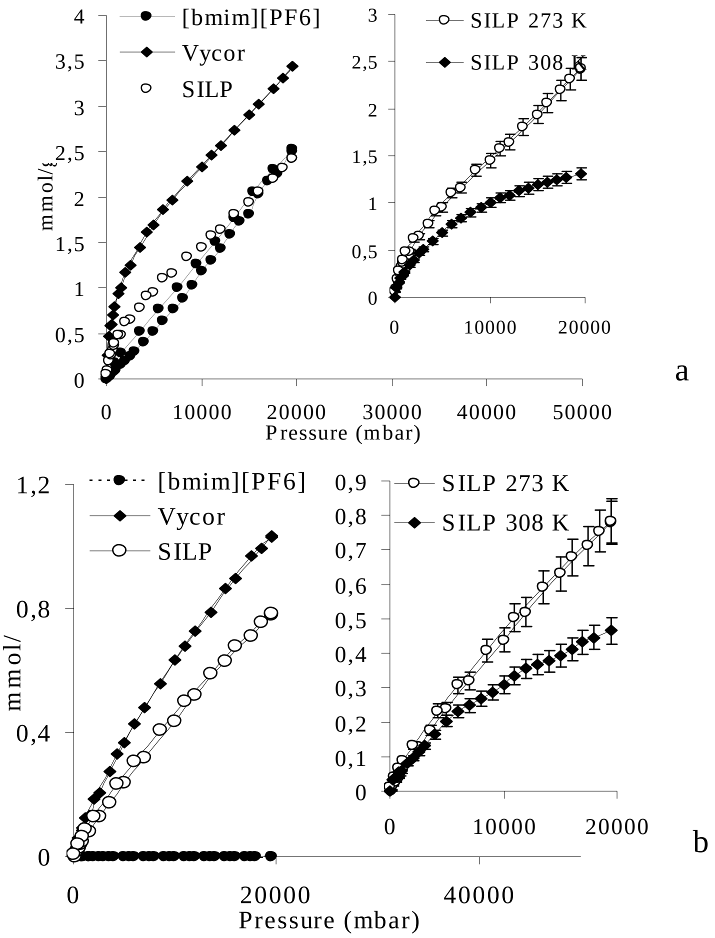

Figure 33. (a) CO$_2$ isotherms at 273 K. Inset: CO$_2$ absorption in the SILP (Vycor) at different temperatures. (b) CO isotherms at 273 K. Inset: CO absorption in the SILP (Vycor) at different temperatures.

The CO$_2$ and CO isotherms (Figures 33a and b respectively) followed the exothermic character of adsorption as a result of the significant contribution of the Vycor® open pores. Concerning the CO$_2$/CO selectivity of the SILP system at 273 K, it was found to be better than the selectivity of the Vycor® support (Figure 34) only at pressures up to 500 mbar. This is because in very low pressure ranges the effect of the CO$_2$ solvation in the [spmim][PF$_6^-$] phase becomes more evident due to the small amounts of CO$_2$ and CO that are stacked on the open pore surface forming the adsorbed monolayer.

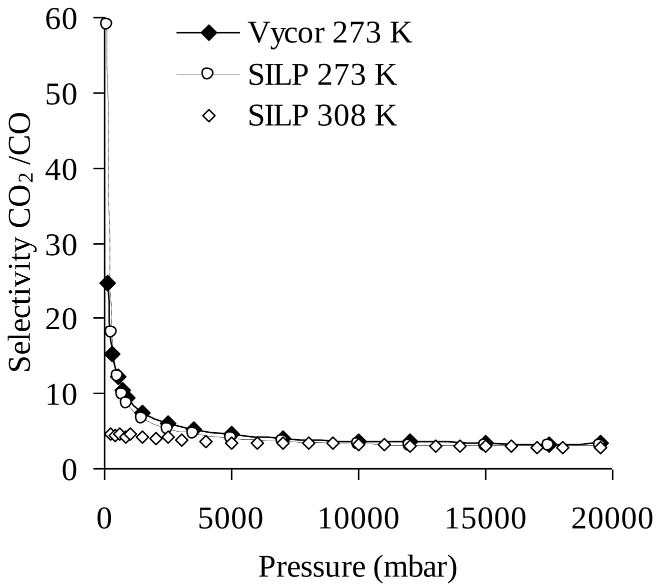

Figure 34. CO_2/CO selectivity vs pressure

4.1.9 Physical state of [spmim][PF_6^-] in the developed MCM-41 hybrid material- Differential Scanning Calorimetry (DSC) and XRD Results

In Figure 35, the results of modulated DSC analysis for the SILP developed on the 2.3 nm MCM-41 support, are presented in comparison to those for the pristine MCM-41 support.

The reversing component of the SILP comprises of an endotherm in the area of 260 ^{o}C that was larger in the case of faster heating (10 ^{o}C/min), as expected for a heating rate depended on reversing transition. This endotherm is attributed to melting of the developed [spmim][PF_6^-], which was already crystallized in room temperature (see XRD, Figure 37b) under the extreme confinement into the 2.3 nm pores.

The second endotherm at 320 ^{o}C, appearing only in the non-reversing component of the MDSC was the result of the thermal decomposition of [spmim][PF_6^-] (Figure 35 b). As it can be observed in Figure 35b, the melting endotherm also comprises of a non-reversing component. This change in behavior can be explained as follows: During the early stages of melting, the presence of many crystallites facilitates melting and recrystallization as heating modulation occurs. Eventually, however, all the crystallites (sites for recrystallization) have melted and recrystallization cannot occur. At that point, melting becomes non-reversing. The relative amount of reversing and non-reversing melting behavior depends primarily on the modulation frequency but further investigations were not performed to address this issue. Finally the high heating rate did not allow to obtain well-resolved melting and decomposition endotherms (Figure 35c).

The development of the [spmim][PF_6^-] phase into the Vycor pores is verified by the decomposition endotherm at 320 ^{o}C (Figure 36b), in good accordance with the endotherm observed in the case of the MCM-41, 2.3 nm support. The higher heating rate (Figure 36b), did not induce any alteration on the intensity of the non-reversingtemperature depended decomposition event, except from a slight shift of its occurrence temperature at 300 ^{o}C. No signs of [spmim][PF_6^-] crystallization were observed, as it was also concluded from the XRD analysis of the sample.

Finally in Figure 36 we present the thermogram of the silanized sample. The decomposition of the grafted silane molecules starts at temperatures well above 320 ^{o}C and on this concept we can claim that the presence of silane does not affect the thermal stability of the developed [spmim][PF_6^-]. On the contrary we can claim that the grafted [spmim][PF_6^-] ionic liquid has a better thermal stability than the bulk [bmim][PF_6^-] (290 ^{o}C).

Figure 37a illustrates the diffraction spectra of both pristine (3.3 nm) MCM-41 and the correspondent SILP sample developed on the MCM-41 support. The background pattern (glass slide) is presented as well. Compared with the pristine sample, the SILP sample shows diffraction peaks appearing at 2θ = 18.2^{o}, 31.9^{o}, 38.2^{o}, 39.4^{o}, 44.5^{o}, 46.2^{o} and 50.9^{o}. The results strongly suggest the formation of [spmim][PF_6^-] crystals within the pores of the nanoporous material. This transition might be attributed to the IL confinement within the pores of the nanostructured materials. Chen *et al.*,[88] based on DSC and XRD analysis, have also reported the transition of IL [bmim][PF_6^-] from liquid to high-melting-point crystal when confined in multi-walled carbon nanotubes.

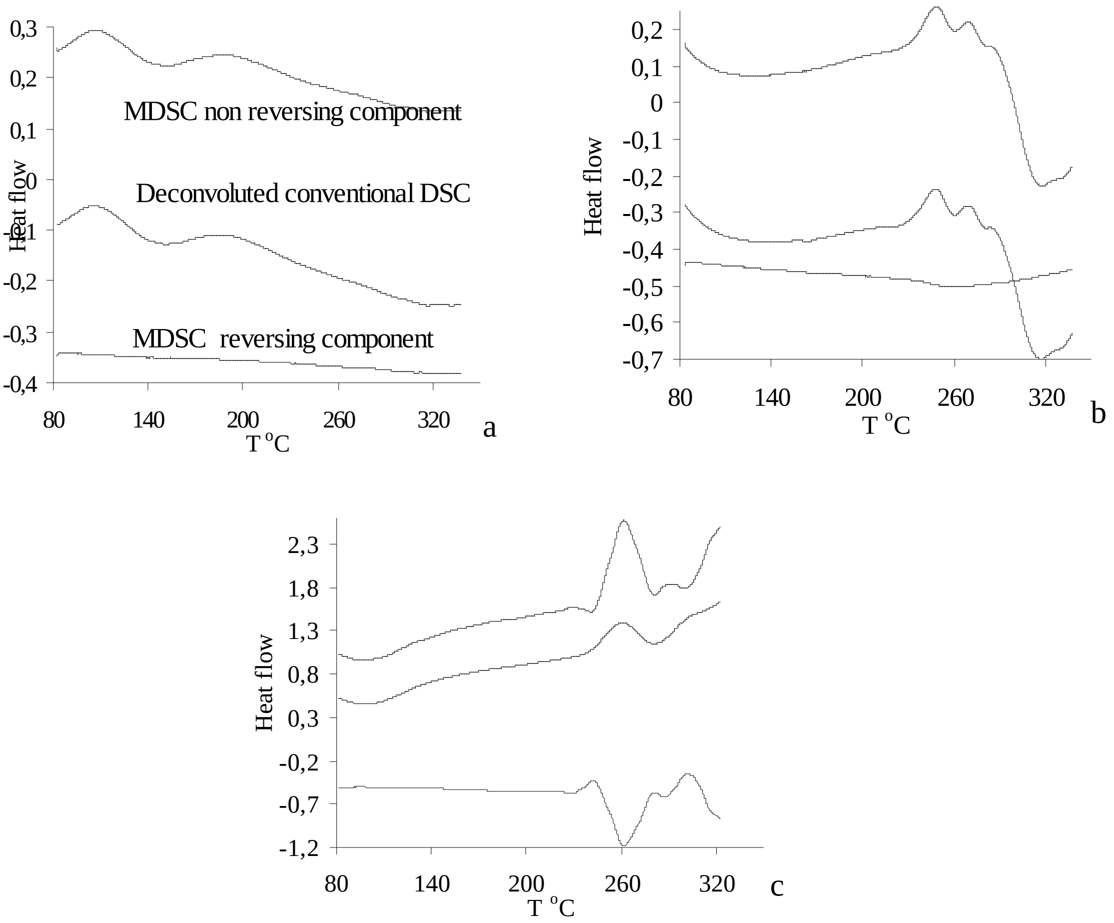

Figure 35. a) MDSC analysis of pristine MCM-41, 2.3 nm, heating rate 1.5 °C/min. b) MDSC analysis of SILP, heating rate 1.5 °C/min. c) MDSC analysis of SILP, heating rate 10 °C/min. Lines from top to bottom of the plots correspond to non-reversing, conventional and reversing components.

In addition, some of their reported peaks (1st, 4th, 6th and 7th) are comparable to ours, implying that the solid phase formed inside the carbon nanotubes has similarities with the one formed within the pores of MCM-41. As in the case of the IL encapsulated inside the nanotubes, a detailed investigation of the IL crystal structure within the pores of the MCM-41 support is difficult to attain and out of the scope of the present study.

Figure 37b presents the diffraction patterns of both pristine MCM-41 (2.3 nm) and the SILP sample. In this case, only the $2\theta = 18.1^{\circ}$ and 32.3° peaks might be attributed to the silylated IL crystallization due to its confinement in the pores, suggesting a short-range order.

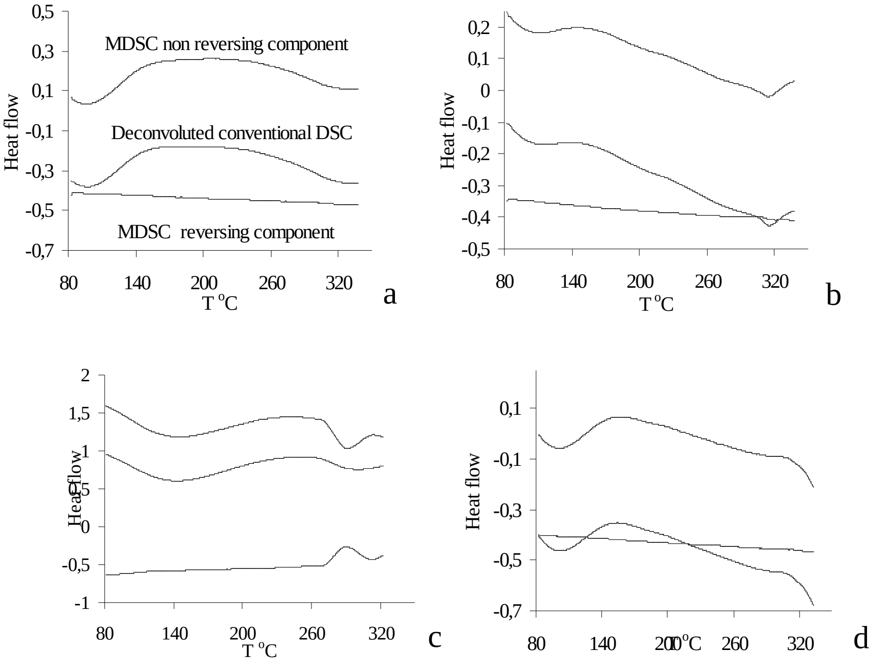

Figure 36. a) MDSC analysis of pristine Vycor®, 4 nm, heating rate 1.5 °C/min. b) MDSC analysis of SILP, heating rate 1.5 °C/min. c) MDSC analysis of SILP, heating rate 10 °C/min. d) MDSC analysis of silanized Vycor®, heating rate 1.5 °C/min.

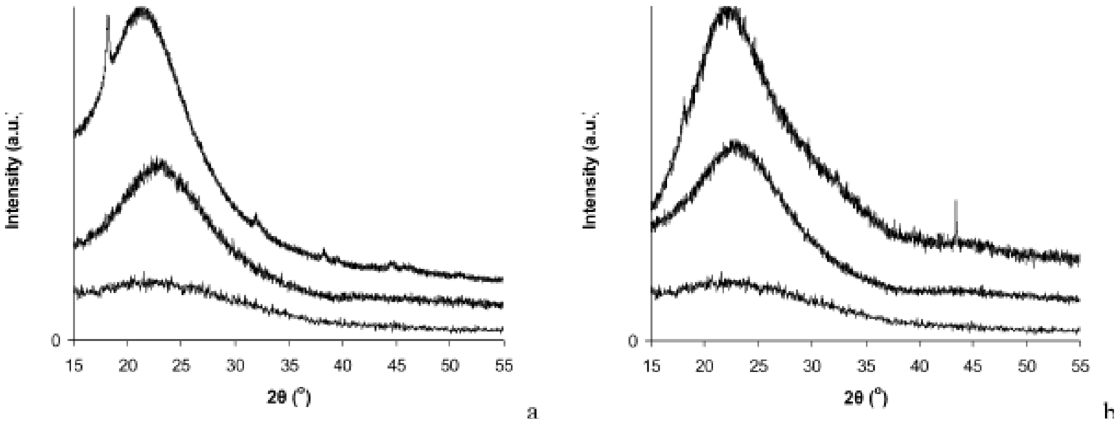

Figure 37. a) X-ray diffraction spectra (from bottom to top) of glass, pristine MCM-41, 3.3 nm and the correspondent SILP system. b) X-ray diffraction spectra (from bottom to top) of glass, pristine MCM-41, 2.3 nm and the correspondent SILP system.

Finally, concerning Vycor sample, the XRD spectra of pristine and SILP samples are similar (not shown), indicating the absence of crystallization at room temperature.

4.2 Supported ionic liquid membranes for CO_2 separation

For the preparation of the Supported Ionic Liquid Membranes (SILM) the "grafting from" method was used, where the ionic liquid is synthesized and then grafted to the support (Figure 38). In order to test the reproducibility of the proposed IL grafting method and the effect of the silanes alkyl chain length on the imbibition efficiency, we have proceeded with the modification of nanofiltration membranes with different pore size. Thereby, two silica (1 nm pore size) and one gamma-alumina (5 nm pore size) membranes were modified with 1-methyl-3-(1-trimethoxysilylmethyl) imidazolium hexafluorophosphate ($C_8H_{17}N_2SiO_3PF_6$). Also, one silica and one gamma-alumina membranes were modified as well with 1-methyl-3-(3-trimethoxysilylpropyl) imidazolium hexafluorophosphate ($C_{10}H_{21}N_2SiO_3PF_6$). The sample codes are included in the following Table 12.

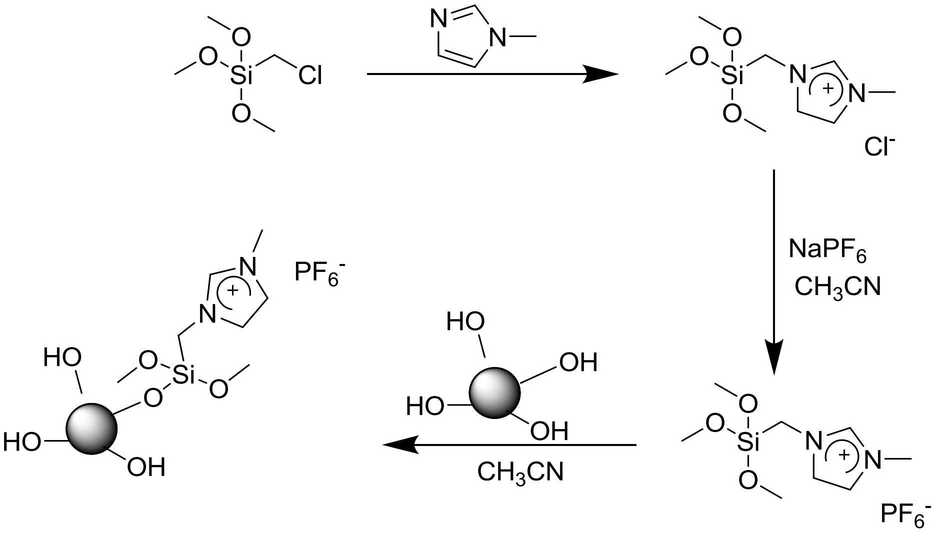

Figure 38. Synthesis of 1-methyl-3-(1-trimethoxysilylmethyl) imidazolium hexafluorophosphate ($C_8H_{17}N_2SiO_3PF_6$) /[smmim][PF_6^-]

For the preparation, a chloroalkyl(methyl, propyl)trialkoxysilane is reacted with methylimidazole in order to obtain the corresponding ionic liquid with the [Cl^-] anion. The procedure is followed by the ion exchange step where the [Cl^-] anion is exchanged by the [PF_6^-] anion. A solution of the prepared ionic liquid in acetonitrile is applied to the membranes in a modified reaction cell (see experimental section) in order to graft the ionic liquid on the inorganic supports.

Table 12. Modified and unmodified membranes with the corresponding chemical formulas of the grafted ionic liquids

Sample code	Pore size	Grafted molecule
M1	1 nm	untreated
SILM1A	-//-	$C_8H_{17}N_2SiO_3PF_6$
SILM1B	-//-	-//-
SILM1C	-//-	$C_{10}H_{21}N_2SiO_3PF_6$
M5	5 nm	untreated
SILM5A	-//-	$C_8H_{17}N_2SiO_3PF_6$
SILM5B	-//-	$C_{10}H_{21}N_2SiO_3PF_6$

4.2.1 Membrane Rehydroxylation

The effect of basic and acidic treatment on the surface hydroxyls population was investigated by means of TGA analysis in argon atmosphere. The α_{OH} values (μmol OH/g) presented in Table 13 were calculated from the mass loss during the temperature ramp from 250 ^oC to 900 ^oC and the isothermal step at 900 ^oC.

Table 13. The surface activation conditions and the resulting hydroxyl group concentration

Entire membrane tube	
Conditions of treatment	**TGA μmol OH/g**
Untreated membrane	17
H_2O_2/H_2SO_4 (1/2), 20 min 60 ^oC	39
H_2O_2/H_2SO_4 (1/4), 20 min 60 ^oC	61
NH_4OH pH 9.8, 6 h 25 ^oC	22
NH_4OH pH 9.8, 18 h 25 ^oC	15
NH_4OH pH 9.8, 20 min 90 ^oC	34
NH_4OH pH 9.8, 10 min 90 ^oC	48
NH_4OH pH 9.8, 1 h 60 ^oC	33
NH_4OH pH 9.8, 20 min 60 ^oC	**71**
NH_4OH pH 9.8, 10 min 60 ^oC	41
Silica nanofiltration layer	
NH_4OH pH 9.8, 20 min 60 ^oC	**150**

Before the ramp, an isothermal step at 250 ^oC was applied to completely remove the physically adsorbed water. The results show that under mild basic hydrolysis conditions (pH = 9.8) and at each of the examined solution temperatures, there is a maximum of the α_{OH} value with the time of treatment. For treatment periods well in excess of the point where the maximum occurs, extended leaching of the surface leads to a moderate population of the surface hydroxyl groups. Acidic hydrolysis in a solution of H_2SO_4/H_2O_2 (4/1) for 20 minutes, presented moderate rehydroxylation efficiency compared to the NH_4OH solution (pH = 9.8).

What is most important to note is the inhomogeneity in the population of surface hydroxyls along the asymmetric structure of the membrane. Indeed, after activation, the silica nanofiltration layer exhibited a double OH population compared to the entire membrane.

4.2.2 Nitrogen porosimetry

The LN_2 porosimetry was performed on the bare alumina support and the entire silica membrane; both materials were provided by the ceramic manufacturer (Inopor$^{®}$). The support isotherm was subtracted from that for the entire membrane and the derived isotherm was appropriately interpreted in order to calculate the open microporosity (ε) and pore surface area (A_c) of the silica nanofiltration layer. The raw isotherms and the one produced from the subtraction procedure are presented in Figure 39.

From the geometrical dimensions and the solid density (d) of the materials consisting the NF layer (silica, d = 2.2 g/cc, thickness 1.5 μm) and the support (alumina, d = 3.2 g/cc, ID = 7 mm, OD = 10mm), we were able to calculate the mass ratio of the NF layer over the entire membrane. The following equation describes the isotherms subtraction procedure:

$$V_{NF}\left(\frac{cc\,(STP)}{g}\right) = \frac{V_{mem}\,(cc(STP)) - V_{\sup}\left(\frac{cc(STP)}{g}\right) x M_{mem}\,(g)\, x\, R_{\sup}}{M_{mem}\,(g) x R_{NF}} \qquad \text{Eq.27}$$

where, V_{NF} is the standard gas volume per mass adsorbed by the nanofiltration layer, V_{mem} is the absolute standard gas volume adsorbed by the entire membrane, $V_{\sup}$ is the standard gas volume per mass adsorbed by the support, M_{mem} is the mass of the entire membrane, $R_{\sup}$ is the mass ratio of the support, and R_{NF} is the mass ratio of the nanofiltration layer. The derived NF layer isotherm was interpreted with the Dubinin and Radushkevich approximation to define the micropore volume and microporosity (V_m = 0.128 cc/g, ε = 0.22) and the micropore surface area (A_c = 360 m^2/g).

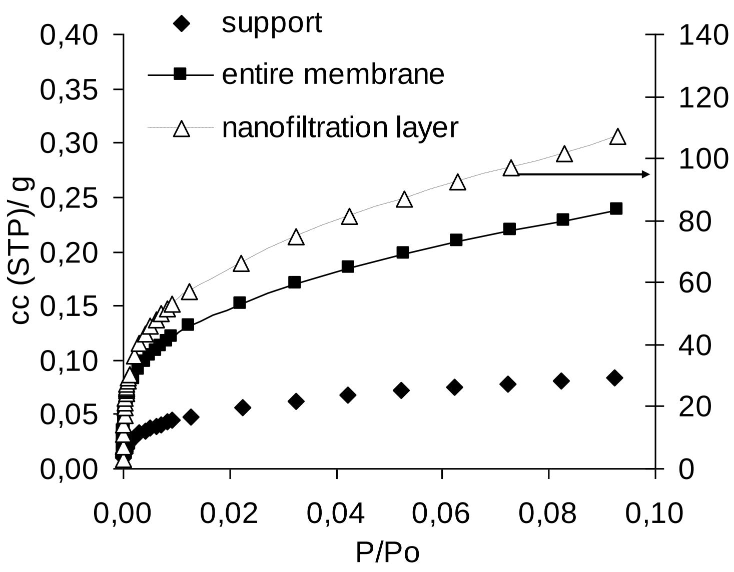

Figure 39. The low-pressure area of the LN_2 isotherms performed on the support and the entire membrane

4.2.3 Elemental analysis /EDAX analysis

The following Table 14 presents the C, H, N content of the nanofiltration layer, as determined by elemental analysis, and the macroporous support of the 1 nm membrane (SILM1A), which was modified with the 1-methyl-3-(1-trimethoxysilylmethyl) imidazolium hexafluorophosphate. These sections of the tubular membrane are easily distinguishable and were mechanically removed and subjected to elemental analysis after the completion of permeability tests. Before the elemental analysis and in order to avoid the contribution of absorbed CO and CO_2, the membrane was degassed at high temperature (180 ^oC) in the imbibition/reaction device.

By EDAX elemental analysis, a strong gradient of the surface concentration of the grafted ionic liquid (C%, N%) is found along the thickness of the membrane (see Figure 40); the simplest explanation is that the concentration gradient results completely from the already discussed in Section 4.2.1 inhomogeneity in surface activity.

Table 14. Elemental analysis results

Silica nanofiltration layer					
C %	H %	N %	C/N	C/H	N/H
4.42	0.67	1.74	**2.5**	**6.6**	**2.6**
α-Alumina macroporous support					
C %	H %	N %	C/N	C/H	N/H
0.84	0.16	0.33	**2.55**	**5.3**	**2.1**
Predicted ratios depending on the number of the grafted alkoxy groups of the silylated IL					
			C/N	C/H	N/H
$C_7H_{14}N_2SiO_2PF_6$			3.0	6.0	2.0
$C_6H_{11}N_2SiO_2PF_6$			**2.6**	**6.5**	**2.5**
$C_5H_8N_2SiO_2PF_6$			2.1	7.5	3.5

However, the α_{OH} ratio ~2.1 between the silica NF layer and the entire membrane (Section 4.2.1), was much lower than the relevant ratio ~5.3 of the carbon concentration (Table 14); consequently the (-OH) gradient along the asymmetric membrane structure is not the only reason for the observed grafting inhomogeneity.

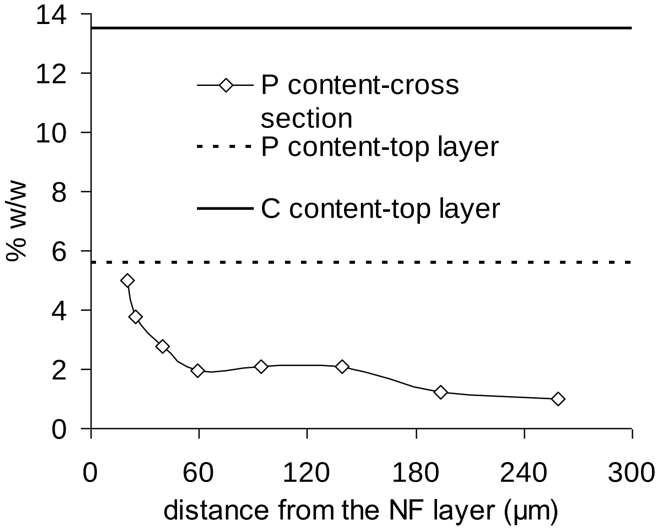

Figure 40. EDAX elemental (C, P) analysis of the membranes' vertical cross-section and top nanofiltration layer

.

In this context we might conclude that the anchoring of the silylated ionic liquid into the nanopores of the NF layer effectively hinders the passage of additional molecules into the pore structure of the succeeding layers. The latter interpretation is supported by Figure 40, where we present the P% weight content defined by the EDAX analysis of the membrane cross section as a function of the distance from the NF layer. The x-coordinate corresponds to the center of the scanned area, with a width and a height of 40 μm. Thus, the first point pertains to the NF layer together with the main part of the subsequent γ-alumina layer (see Figure 41) and each of the remaining points is obtained by successive shifts of the x-coordinate by 5 microns in the direction from the inner to the outer side of the membrane. The horizontal lines represent the average C% and P% w/w contents, defined by scanning the top surface of the silica nanofiltration layer. The very sharp drop of the P% occurring up to a distance of 60 microns from the internal side demonstrates the sieving action of the grafted nanofiltration pores. On the other hand, the almost identical P% contents of the NF layer's top surface and cross section indicate that most of the excess silylated IL layer, which may have been formed due to the sieving mechanism on the top of the internal membrane's surface, have been effectively removed by means of the washing procedure described in the experimental section.

In addition, the C%/P% w/w content ratio for the top surface is about 2.4 instead of 3.1, which would be the value expected from the stoichiometry of a non grafted silylated IL molecule ($C_8H_{17}N_2SiO_3PF_6$).

Moreover, both the C%/P% ratio of the top surface and the C%/N% ratios presented in Table 14 are compatible with the idea that grafting occurred with two of the methoxy groups of the silylated IL. This is evidence for the high density of the OH groups being the result of the optimum activation conditions defined in this work. Finally although the derived by elemental analysis hydrogen content can be affected by the contribution of the surface hydroxyls, the good accordance of the C%/H% and N%/H% with those of the grafted silylated IL molecule ($C_6H_{11}N_2SiO_2PF_6$) is compatible with the idea that there is almost a complete consumption of the surface hydroxyls, especially those of the NF layer.

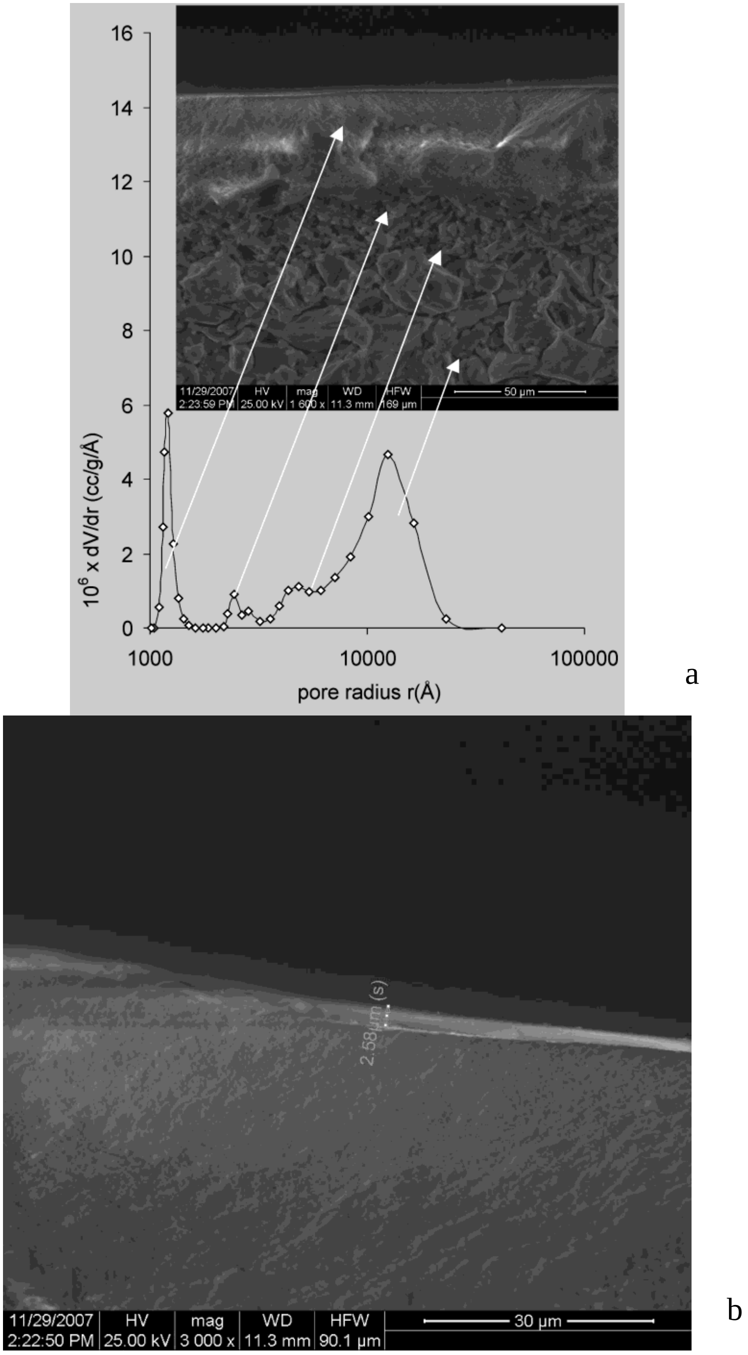

Figure 41. (a) SEM image of a vertical cross section of the membrane showing the sequential layers of different pore size as defined by mercury porosimetry and (b) SEM image focusing in the area of the top nanofiltration layer.

4.2.4 Permeability of He - Extraction of the structure factor

In order to determine how tortuous the structure of the membranes' NF layer was, He permeability experiments were conducted. Structure factors (κ_g) were calculated for three silica membranes of the same batch and are provided together with the corresponding permeability values in Table 15.

Table 15. Experimental values of He permeability and the calculated structure factors

	Temperature °C		
	100	200	300
	He permeability (cm^2/sec) / structure factor (κ_g)		
M1A	2.17E-06 / 6.4E-03	4.36E-06 / 1.1E-02	1.12E-05 / 5.9E-03
M1B	1.10E-06 / 3.3E-03	2.28E-06 / 6.0E-03	6.98E-05 / 3.7E-03
M1C	1.37E-06 / 4.0E-03	3.69E-06 / 9.7E-03	1.09E-05 / 5.8E-03

For the calculation of the structure factor κ_g, the following equation was used which gives the permeability factor D (cm^2/sec) according to the Fick's first law:

$$\frac{J\ell}{U_c\left(\Delta C\right)} = D^o\kappa_g = D = \frac{8}{3}\kappa_g\frac{\varepsilon}{A_c}\left(\frac{2RT}{\pi M}\right)^{1/2} \quad ,\kappa_g = \frac{\delta\varepsilon}{\tau} \qquad \text{Eq.28}$$

where, D^o (cm^2/sec) is the thermodynamic or 'ideal' permeability factor for the case of parallel cylindrical pores of uniform size, κ_g is the structure factor, R is the gas constant, M is the gas molecular weight and τ the tortuosity factor. δ is depended on pressure and for low pressures $P_\mu \rightarrow 0$, $\delta \rightarrow (2-f)/f$, where f is the fraction of molecules striking the pore walls. The porosity ε and pore surface area A_c used for the calculations were determined by LN$_2$ porosimetry as we saw in Section 4.2.2. The κ_g values for the three membranes were derived by the ratio between the experimentally defined and the ideal permeability factor and are included in Table 15. These values indicate a quite tortuous structure of the NF layer with the tortuosity factor ranging between 20 and 60.

4.2.5 CO$_2$-CO absorption curves/Solubility

In Figure 42 we present the results of CO$_2$ and CO absorption at different temperatures for the ionic liquid [bmim][PF$_6^-$] and its silylated analogue 1-methyl-3-(1-trimethoxysilylmethyl) imidazolium hexafluorophosphate ($C_8H_{17}N_2SiO_3PF_6$) [smmim][PF$_6^-$]. As it can be observed, the carbon dioxide follows the exothermic character of solvation in both the commercial [bmim][PF$_6^-$] and the [smmim][PF$_6^-$]. The Henry constants ($\overline{H}$ bar/mol fraction) correlated positively with temperature. The $\overline{H}$ values of 32, 40 and 63 bar/(mol fraction) calculated for the commercial ionic liquid at 273, 288 and 308 K respectively, were in good accordance with those often encountered in literature.[89]

The $\overline{H}$ value of the synthesized [bmim][PF_6^-] (33.8 bar/mol fraction) at 273 K, deviated no more than 6% from the value for the corresponding commercial product; this finding is compatible with the assumption that the synthesized ionic liquid phase is a substantially pure one. In the case of the synthesized alkoxysilyl-IL [smmim][PF_6^-], absorption results were normalized per net mass of the 1-methyl-3-methylimidazolium-hexafluorophosphate [mmim][PF_6^-] in the alkoxysilyl-IL molecule since the silyl part is not expected to have any remarkable effect on the CO_2 absorption capacity.

By applying a mass fraction (silyl/[mmim][PF_6^-]) of 0.5 as calculated from the stoichiometry of the molecule, we derived an $\overline{H}$ value of 42 bar/(mol fraction) at 273 K, 60 bar/(mol fraction) at 288 K and 80 bar/(mol fraction) at 308 K for the synthesized alkoxysilyl-IL. There are two possible reasons for the lower absorption capacity of the silylated-IL. The first has to do with the number of carbon atoms in the alkyl chain of the imidazolium ring, that is 1 for the [smmim][PF_6^-] and 4 for the bulk ionic liquid [bmim][PF_6^-]. Various studies suggest that apart from anionic part of the IL, changes in the imidazolium cation involving alkyl groups might also affect the CO_2 solubility.[34] In fact the longer alkyl chains usually lead to slightly better CO_2 absorption capacity in the ionic liquid phase.[91, 92]

In our case the effect of the carbon atom number seems to be more enhanced as the Henry constant ratio, for a difference of 3 carbon atoms in the alkyl chain, was about 0.7 compared to ratios of 0.94 often found in literature for differences of 2 up to 4 carbon atoms.[91] Based on this fact we might conclude that the lower CO_2 solubility value mainly arises as a result of the presence of a silyl group attached to the alkyl chain of the imidazolium ring; the latter feature might lead to a modest loss of organization of the anion and the CO_2 around the cation.

As regards the CO solubility, the calculated $\overline{H}$ values of 2158, 2185, and 2373 bar/(mol fraction) at 308, 288 and 273 K for the commercial [bmim][PF_6^-] and 2202 at 273 K for the synthesised [bmim][PF_6^-], were in good accordance with those found in the work of Kumelan *et al.*,[93] and deviated positively by approximately 100% from those found in the studies of Jacquemin *et al.*[94]

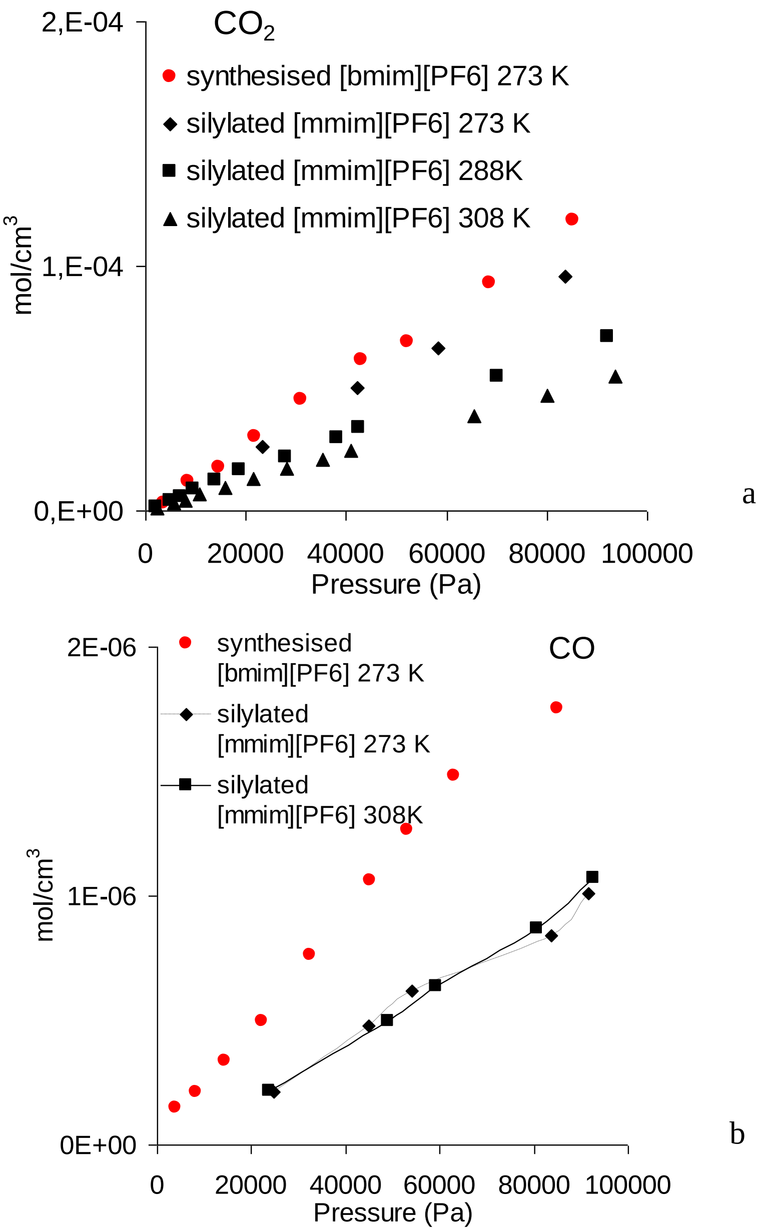

Figure 42. a) CO_2 absorption on the synthesized [bmim][PF_6^-] and silylated [smmim][PF_6^-], and (b) CO absorption on the synthesized [bmim][PF_6^-] and silylated [smmim][PF_6^-].

Moreover in both of the aforementioned studies and also in our work the calculated $\overline{H}$ values for CO practically did not depend on temperature. As a matter of fact, in the case of Kumelan's[94] work there was even an indication of a slightly negative correlation and the same is true in our case ($\overline{H}$=2373, 2185 and 2158 bar/(mol fraction) at 273, 288 and 308 K respectively); such trends indicate that the crossed gas–ionic liquid molecular interactions are of different nature in the CO and CO_2 cases.

Table 16. Solubility of CO_2 and CO and the derived ideal selectivities

T(K)	308	288	273
	Solubility (S_i) 10^{10} x (mol/cm^3/Pa) S_{CO2} / S_{CO} / **(selectivity CO_2/CO)**		
Commercial [bmim][PF_6^-]	8.61 / 0.24 / **36**	12.5 / 0.23 / **54**	15 / 0.21 / **72**
Silylated [smmim][PF_6^-]	5.91 / 0.12 / **50**	7.7 / - / -	11.5 / 0.11 / **105**

In Table 16 we present the CO_2 and CO solubility values expressed in mol/cm^3/Pa and the derived ideal sorption CO_2/CO selectivities. As it can be seen, the silylation of the imidazolium based ionic liquid had a more intense negative effect on the solubility of CO compared to CO_2, thus resulting in an enhanced CO_2/CO separation capacity.

In general the selectivity values observed suggest that the potential of membrane CO_2 separation technology by means of a SILM system is a substantial one.

4.2.6 Transient curves/CO_2 Diffusivity

For the definition of the diffusivity D (cm^2/sec) of CO_2 in the commercial ionic liquid and the silylated IL, the transient curves of the CO_2 adsorption at 308 K were fitted to the solution proposed by Crank for the adsorption in a plane sheet at the beginning of a sorption experiment when the following conditions are satisfied:[95] 1) the initial concentration of the gas in the liquid is uniform, 2) the surfaces of the liquid film are kept at constant concentration, 3) the amount of the gas taken up by the liquid is a negligible fraction of the whole. The solution has the following form:

$$\frac{m_t}{m_\infty} = 2\left(\frac{Dt}{\ell^2}\right)^{-\frac{1}{2}} \left\{\pi^{\frac{1}{2}} + 2\sum_{n=1}^{\infty}(-1)^n \, ierfc \, \frac{n\ell}{\sqrt{Dt}})\right\} \qquad \text{Eq.29}$$

where m_t is the total amount of gas which has diffused into the liquid film at time t, m_∞ is the total amount of gas that has diffused into the liquid after infinite time and ℓ (cm) is the half liquid film thickness. For very short times, the fractional uptake of the gas by the liquid is approximated well by the simple equation:

$$\frac{m_t}{m_\infty} = 2\left(\frac{Dt}{\pi\ell^2}\right)^{-\frac{1}{2}} \qquad \text{Eq.30}$$

The diffusivities for the several pressure steps were calculated from the slope of the $\frac{m_t}{m_\infty}$ vs $\sqrt{t}$, for a liquid film thickness 2ℓ of about 0.15 cm, as calculated by the liquid mass and density and the diameter of the sample basket used in the microbalance setup. The results are presented in Table 17.

Table 17. Diffusivity constants (*D*) and permeability factors calculated from the transient curves of the absorption experiments

	Pressure steps (mbar) 50-150	 250-400	 500-600
	$2(D/(\pi\ell^2))^{1/2}$ (sec$^{-1/2}$) / D (cm^2/sec)		
Commercial [bmim][PF$_6^-$]	0.0055 / 1.7E-06	0.0063 / 2.33E-06	0.0096 / 5.4E-06
Silylated [smmim][PF$_6^-$]	0.0041 / 9.8E-07	0.0048 / 1.35E-06	0.0057 / 1.91E-06
	Permeability (10^{16} x (mol cm/cm^2/sec/Pa)) / Barrer		
Commercial [bmim][PF$_6^-$]	14.63 / 4368	20 / 5971	46.5 / 13883
Silylated [smmim][PF$_6^-$]	5.8 / 1732	7.98 / 2383	11.28 / 3368

The $\frac{m_t}{m_\infty}$ vs $\sqrt{t}$ plots for the synthesized ionic liquid and the silylated IL are depicted in Figure 43. In both examined cases, the diffusivity increases with pressure as the result of the decrease of the ionic liquid viscosity due to the dissolution of higher amounts of CO_2.

The diffusivity constants (*D*) of 10^{-6} cm^2/sec coincide with the results of Hou and Baltus.[96] Finally, the predicted CO_2 permeability values are also included in Table 17. They were calculated with the assumption that transport through a SILM follows the solution/diffusion mechanism:

$$P = D\ S \qquad \text{Eq.31}$$

where *P* is permeability, *S* is solubility (in moles per volume per partial pressure), and *D* is diffusivity.

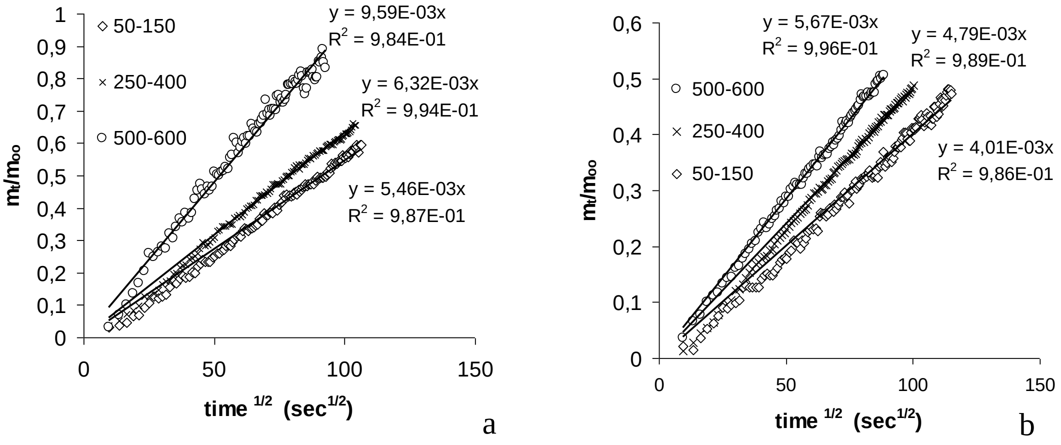

Figure 43. $\frac{m_t}{m_\infty}$ vs $\sqrt{t}$ plots at several pressure steps: (a) [bmim][PF_6^-] and (b) [smmim][PF_6^-].

A remarkable observation is that the presence of the silyl group on the alkyl chain of the imidazolium ring not only resulted in considerably lower CO_2 absorption capacity, but also decreased the rate of diffusion to about half the value of that of the commercial [bmim][PF_6^-] sample.

4.2.7 Selectivity CO_2/CO – Diffusion mechanism

The stability of the developed SILM membranes and the reproducibility of the proposed imbibition/reaction method can be concluded from the permeability selectivity results presented in Figure 44.

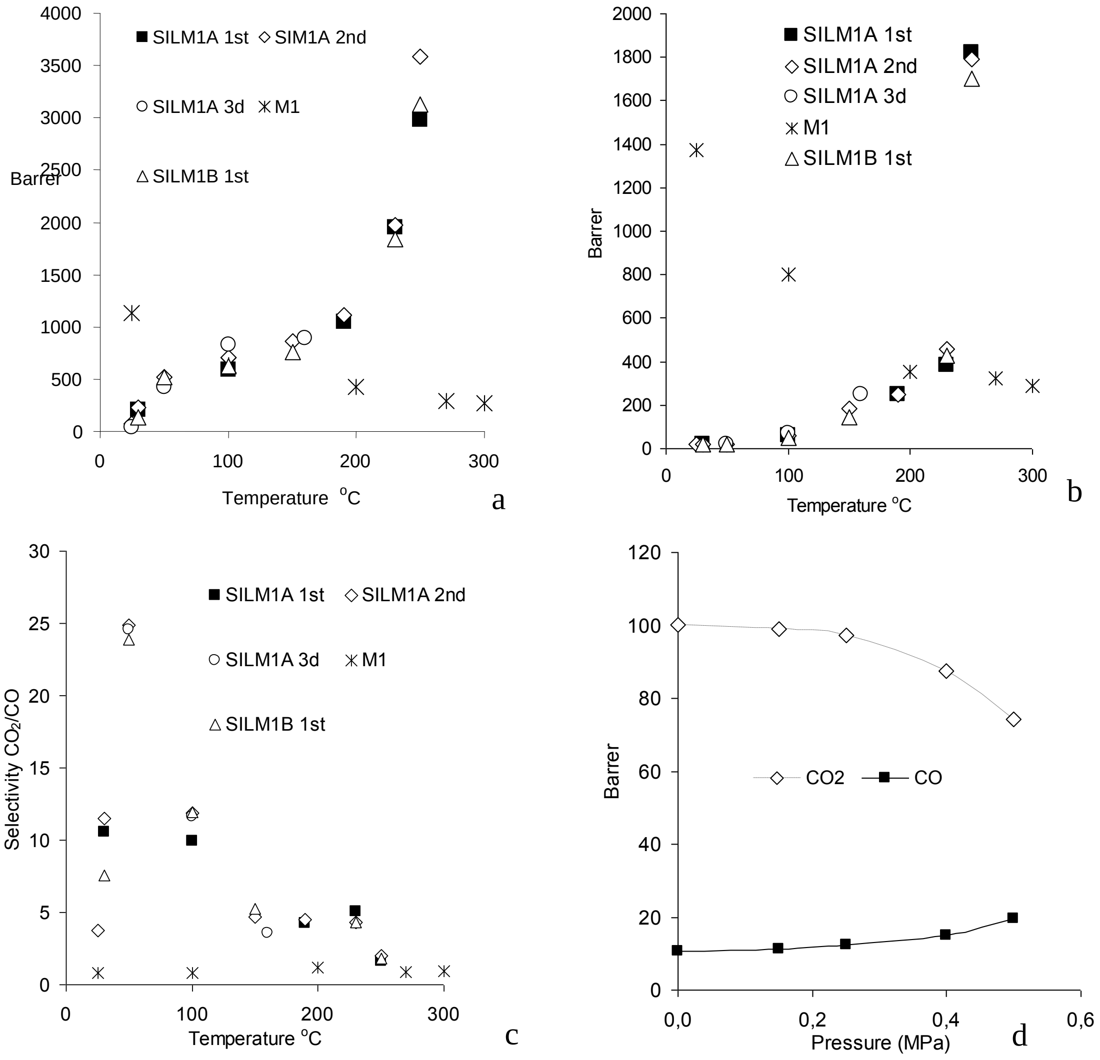

Figure 44. (a) Permeability of CO_2 dependence on temperature, (b) permeability of CO dependence on temperature, conditions for (a-c): trans-membrane pressure = 0.5 MP, feed conc. = 50% - 50%, CO_2/CO (v/v), (d) permeability dependence on pressure at 25 °C.

The duration of testing at each temperature was about 4 hours. For example, membrane SILM1A which was subjected to three sequential heating/cooling cycles from RT (or rt) to 250 °C, at a trans-membrane pressure of 0.5 MPa, exhibited a 5-day stability. In addition, the similarly developed membrane SILM1B exhibited permeability factors within ±10% of those defined for SILM1A.

The permeability was calculated with the assumption that the pore volume of the thin nanofiltration layer (1.5 μm thickness) is completely occupied by the silylated ionic liquid phase [smmim][PF_6^-], which primarily controls the gas diffusion through the entire SILM. Indeed, the CO permeability of the pristine nanofiltration membrane

M1 at room temperature is about 100 times higher than that of the modified SILM membranes; this finding is indicative of the high extent of pore blockage.

An issue that requires further explanation is that at the temperature of 30 ^oC, the experimentally derived permeability values of CO_2 for the modified membranes SILM1A and SILM1B (Figure 44a) are about one order of magnitude lower than those calculated by means of Equation 30 (Table 17), with the factors *D* and *S* already defined from the CO_2 isotherm of the silylated ionic liquid [smmim][PF_6^-] (Table 16). Several factors may contribute to the deviation from the predictions, each one with a different impact, such as:

A) The counter diffusion of the sweep gas applied in the permeability-selectivity measurements.

B) The fact that even if the pores are completely filled with the ionic liquid, the IL permeability is underestimated due to the presence of the non permeable ceramic in the remaining fraction of the membrane volume (porosity) and the tortuosity of the pore structure.

C) The presence of the second type of gas molecules that dissolve simultaneously with the CO_2 molecules in the bulk of the silylated ionic liquid.

D) The contribution of the silylated ionic liquid phase that is deposited on the pore surface of the subsequent macroporous membrane layers without blocking, at the same time, the pore space. This contribution is indirectly demonstrated on the basis of the data presented in Table 18. From the comparison of the cases of M5 (non grafted nanoporous) and SILM5B (grafted but non blocked nanoporous), it is clear that the CO_2/CO selectivity is worse in the latter case i.e. when the grafted material does not block the pores, it favors the passage of CO over that of $CO_{2.}$

E) The application of elevated trans-membrane pressures (0.5 MPa).

The negative effect of the first two factors has already been discussed in literature;[97-99] the larger of the two contributions corresponds to the second factor and depends on the porosity ε of the membrane and the tortuosity factor τ (usually $\varepsilon = 70$ % and $\tau = 1.2\text{-}2$ for macroporous polymeric membranes). The ceramic nanofiltration membranes used in this work had a moderate open microporosity of 22%, whereas the tortuosity (τ) exceeded the value of 20. According to these pore structural characteristics, the experimentally defined CO_2 permeability of the ionic liquid should be 20/0.22, that is~100 times lower than the predicted one. Thereby, we can claim that the ionic liquid permeability is overestimated rather than underestimated. A possible explanation for this discrepancy is that the routes of the permeating CO_2 molecules inside the pores are less tortuous than those in the bulk liquid because the grafted material inside the pores is a structured one.

In what follows we provide evidence that the ionic liquid phase, which is deposited on the pore surface of the subsequent macroporous membrane layers, may have a considerable contribution to the reduction of the CO_2/CO separation performance. To this end we present (Table 18) the results obtained for the modified γ-alumina NF membrane (SILM5) with nanofiltration pores of 5 nm. The latter size was too large for complete pore filling by the surface anchored [smmim][PF_6^-] species. Because of the openings left, the combined result was a CO_2/CO selectivity less than one.

It can be concluded that when the deposition of the silylated IL was not accompanied by complete blockage of the nanopore structure (SILM5A), we had an opposite effect on the CO_2/CO separation capacity, e.g. the CO permeated faster.

Based on these findings, a complex diffusion mechanism is proposed for the [smmim][PF_6^-] modified nanofiltration membranes of 1 nm pore size (Figure 45). Specifically, at the section of the nanofiltration layer (A), the preferable solvation of CO_2 into the silylated ionic liquid favors its separation from CO. Thus more CO_2 molecules diffuse through the bulk ionic liquid and desorb into the gas phase inside the void space of the succeeding macroporous layers. Next to that, partitioning of the CO_2 and CO molecules occurs between the gas phase and the ionic liquid film. The partitioning mechanism favors the faster permeation of CO, since the CO_2 molecules reside for a longer time into the liquid phase. The partitioning effect must be strong due to the minor diffusion length of the nanofiltration layer (1.5 μm) compared to that of the succeeding macroporous layers (1500 μm).

However we cannot accept it as the only reason for the CO_2/CO selectivity decrease from 50, as predicted from the absorption results (Table 16), to about 11 as defined from the permeability experiments (Table 18). On the basis of the data presented in Figure 44d, we suggest that the elevated trans-membrane pressure and the co-solvation/diffusion of CO have a negative effect on the permeability of the CO_2 species.

Table 18. Experimental permeability values measured with the Wicke-Kallenbach set-up

Material	Molecular Formula	T °C	Pe CO_2 Barrer	Pe CO Barrer	Selectivity CO_2/CO
M5	-	25	27412	28496	0.96
		100	27365	27941	0.98
SILM5A	$C_8H_{17}N_2SiO_3PF_6$	25	22987	27375	0.84
		100	23124	27564	0.84
SILM5B	$C_{10}H_{21}N_2SiO_3PF_6$	25	454	624	0.73
		100	460	672	0.68
M1	-	25	1135	1373	0.83
		100	635	800	0.8
SILM1A	$C_8H_{17}N_2SiO_3PF_6$	25	226	20	11.3
		100	715	60	11.9
SILM1C	$C_{10}H_{21}N_2SiO_3PF_6$	25	124	154	0.81
		100	84	79	1.07

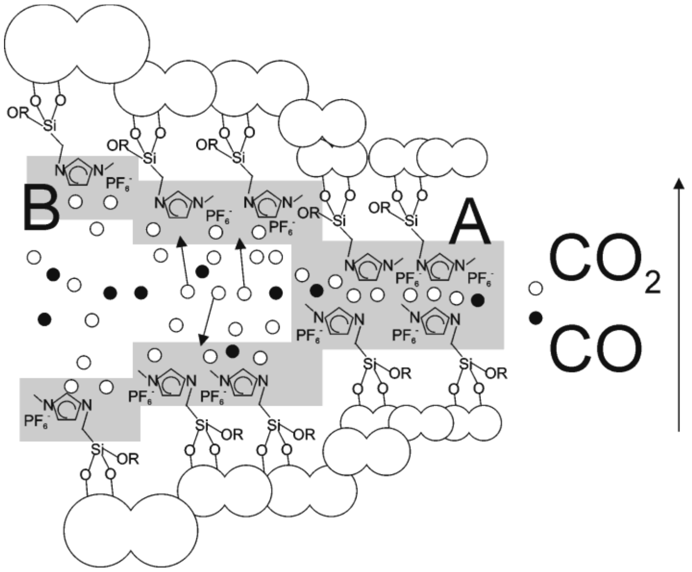

Figure 45. The proposed overall diffusion mechanism showing the contribution of the uncovered macroporous layers of the asymmetric membrane

The pressure plot demonstrates that for a 50/50 (% v/v) mixture of CO_2/CO, the trans-membrane pressure increments have provoked considerable reduction of the CO_2 permeability and an exactly analogous increase of the CO permeation. Contrary to this, the analysis of the single-phase CO_2 absorption transient curves revealed a positive correlation of the CO_2 diffusivity with pressure, as expected due to the decrease of the IL viscosity upon absorption of higher amounts of CO_2.

In this context we can argue that the reason behind the negative correlation of the CO_2 permeability with pressure is ultimately due to the increasing amounts of CO molecules, which they strongly modify the CO_2-ionic liquid interactions. In a study concerning the system ionic liquid/carbon monoxide,[100] conducted by high pressure ^{13}C NMR spectroscopy, it was shown that the CO solubility depends upon the nature of the ionic liquid due to the presence of dipole moment and polarisability. In the same study concerning the 1-butyl-3-methylimidazolium cation based ionic liquids, the solubility of CO increased with increasing anion size due to the decrease in π^* interactions. Thereby the interaction of the CO molecules with the anion may lead to the loss of the "tangent like" organisation of the CO_2 molecules around the anion, which is regarded as the main reason for the high CO_2 solubility.[101]

Concerning the performance dependence on temperature, it is interesting to note that the CO_2/CO selectivity presented a maximum at 50 ^oC for both membranes SIM1A and SILM1B. This indicates that the solution-diffusion mechanism is not a simple one. Selectivity would normally be a monotonous function of temperature in a bulk material where local structural subtleties are averaged. On the other hand in our case the structure of the matrix material (grafted pore-filling material) exhibits a variation along the radius and at least in the case of CO_2 species there might be a preference for certain, far from random, paths that favour Lewis-acid based interactions. When the temperature is raised, individual CO_2 diffusion steps might become easier but at the same time the intraporous material might become less ordered and hence the original path might become more tortuous/less efficient; the outcome of the combined effect of the latter two factors allows for the exhibition of subtleties (including non-monotonous variation of selectivity with temperature) which are not encountered in the usual case of bulk matrices.

Finally from the results presented in Table 18, we can conclude that the longer alkyl chain of the silane molecule (chloropropyl instead of chloromethyl silane) was not sufficient to provoke the complete blockage of the 5 nm pores (SILM5B). Although the permeability factors were considerably reduced compared to membrane SILM5A, the CO_2/CO selectivity was still inversed, thus confirming the partitioning effect, which occurs in cases where the ionic liquid phase is just deposited on the pore surface without effectively blocking the pore space. On the other hand, the propyl chain was long enough to prohibit the entrance of the silylated-IL (1-methyl-3-(3-trimethoxysilylpropyl)imidazolium hexafluorophosphate) into the 1 nm pores of membrane SILM1C. In this case, the permeability was about one order of magnitude lower than that of the unmodified membrane as a consequence of the deposition of the silylated IL molecules on the external surface of the top-separating layer around the pore mouths. Thus the pore mouth openings were partially blocked resulting to considerable hindrance on the entrance of the gas molecules into the pore structure but not to a considerable enhancement of the CO_2/CO selectivity since the deposited IL phase was not exerting full control over the diffusion of the gaseous molecules.

4.3 Study of the effect of pore structure characteristics on the gas diffusivity – and gas separation of SILPs

4.3.1 Amount of IL deposited in a porous system by ex-situ dipping techniques

In order to elucidate physicochemical properties of the IL under confinement, supports of various diameter were modified either by grafting the IL on the surface (functionalized IL) or by impregnating [bmim][$PF6^-$] (non-functionalised) into the pores of the support (Table 19).

Factors, which control the amount of IL loaded into the channels of a porous support, are exemplified in regard to the LN_2 porosimetry results (Table 19). These are the total pore volume and surface, the surface chemistry (functional groups) and charge, as well as morphological characteristics of the pore structure such as the dimension of the pores, the pore size distribution and the tortuosity of the network.

The volume of IL loaded during the ex situ dipping technique, using the functionalized and non-functionalized IL, was calculated from the pore volume difference between the pristine support and the SILP system.

When a silylated IL was applied as surface modifier, there was a quite satisfying correlation between the BET surface area of the pristine support and the pore volume reduction after dipping, the latter expressed as volume of IL loading (Figure 46a).

No correlation was observed between the IL loading and the initial pore volume or pore dimension (Figure 46b). In this regard, the formation of a monolayer of the functionalized IL on to the pore walls of the support can be safely concluded. Small deviations from linearity (Figure 46a) can be attributed to the different population and proximity of the silanol (Si-OH) groups on the surface of the several materials applied as supports. In general, the silanol density of ordered mesoporous silicas (e.g. MCM-41 or SBA-15) ranges[102-104] between 1 and 3 SiOH/nm^2 whereas for porous glasses like Vycor® and CPG, silanol densities between 1.6 and 3.8 SiOH/nm^2 have been reported.[105] However the population of surface silanols and their distribution on the mesopore surface strongly depends on thermal treatments, activation under vacuum and dehydroxylation/rehydroxylation processes.

In the case of a standard SBA-15, a silanol density closer to 1 SiOH /nm^2 had been observed when the material was heated at 200 ^{o}C under vacuum,[104] conditions which were similar to those applied in the current work in order to regenerate the samples just before the LN_2 measurement and the ex situ dipping process.

On the other hand, in a recent study of our group,[106] a water vapor desorption method has been developed and applied that allowed for the definition of the surface silanol population. By means of this method, silanol densities of 1.3 and 2 SiOH/nm^2 were obtained for Vycor and MCM-41 respectively. In this respect, the correlation factor is readily improved from 0.92 to 0.96 when the IL loading is plotted in relation to the silanol density per mass unit of the support (Figure 46c). Deviation from linearity was observed solely for the MCM-41 samples of different pore size. The reason behind this might be that MCM-41 is characterized of at least three types of silanol groups: single silanols $(SiO)_3SiOH$, hydrogen bonded $(SiO)_3SiOH$-$OHSi(SiO)_3$ and geminal silanols $(SiO)_2Si(OH)_2$ with different accessibility to silylating agents and different relative population between samples. It is also worth noting that there is no deviation from the linearity between the tortuous (Vycor, CPG) and non-tortuous samples (MCM-41, SBA-15, a fact indicating that the interconnectivity and constrictions of the channel network do not affect the proper wetting of the pore walls with the IL solution during the ex situ dipping process.

The absence of a good correlation between the amount of IL loaded and any of the pore structure characteristics for the supports modified with the non-functionalised IL, is evidenced in Figure 46d, e. The main reason is that the interactions of the IL with the pore surface are limited to dipole interactions (there is not chemical bonding) and therefore a random leaching of the deposited IL layers during the sequential washings with the solvent might occur.

Table 19. Surface area pore size and volume of the samples before and after the modification with the ILs

	BET	Pore size	Total pore volume
	m^2/g	nm	ml/g
Vycor	175	4.3	0.24
CPG	153	20.1	0.85
SBA-15	711	5.6	0.93
MCM-41-3.3	1117	3.3	1.54
MCM-41-2.9	1068	2.9	1.18
MCM-41-2.3	1543	2.3	0.86
Vycor-f*	96		0.12
CPG-f	147		0.71
CPG-nf**	96		0.61
SBA-15-f	359		0.65
SBA-15-nf	14		0.05
MCM-41-3.3-f	430		0.84
MCM-41-2.9-f	368		0.42
MCM-41-2.9-nf	113		0.33
MCM-41-2.3-f	41		0.08

* A functionalised (silylated) IL is abbreviated with –f. ** A non-functionalised IL is abbreviated with –nf.

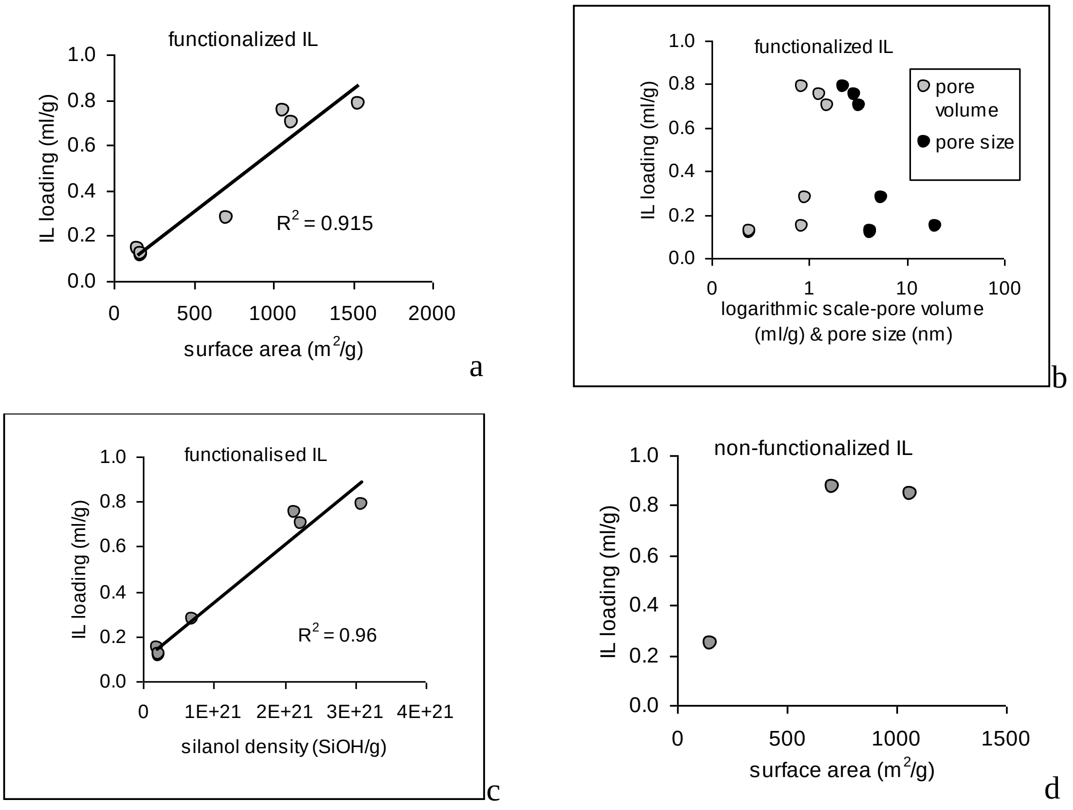

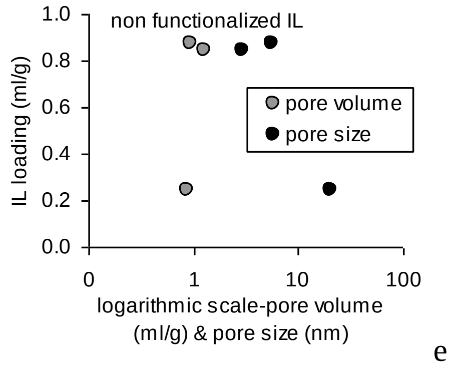

Figure 46. Correlation of the IL loading with a) and d) the surface area of the support, b) and e) pore volume and pore size, c) surface silanol density.

Even though interactions with the surface are weak, we should emphasize that the amount of IL loading was higher for the cases when the non-functionalized [bmim][PF_6^-] was applied as support modifier (Table 19). The smaller molecular volume compared to the silylated IL as well as different deposition orientations with both anions and cations in direct contact with the surface, may generate enough intra pore space for the formation of succeeding layers and enhanced loading. Extended discussion on the possible orientation of IL molecules in relation to the obtained gas diffusivity data, and with the support of recent findings of other groups that apply techniques such as photoelectron and surface vibrational spectroscopy, is given in paragraph 4.3.4. In the next paragraph, we discuss the inability of LN_2 to provide information on the extent of pore blocking by the deposited IL layers and we also highlight the potential of SANS as a pore bulk sensitive method to provide an insight on this issue.

4.3.2 Extent of pore coverage

Complete pore coverage or blocking by the deposited IL phase may be detrimental for a catalytic process where the high pore surface must be exploited to the maximum. On the contrary, it may be a requirement for a gas separation application, especially when a task specific IL (i.e. amino functionalized for CO_2 sorption) is involved as surface modifier. The results of LN_2 porosimetry (Figure 47) cannot by themselves lead to safe conclusions about the pore coverage extent for two reasons. LN_2 porosimetry is a pore mouth sensitive technique and as an example, the almost zero adsorption capacity observed for the MCM-41 (2.3 nm) modified with the silylated IL (Figure 47a) and for the SBA-15 (5.6 nm) modified with the non-functionalised IL (Figure 47e), might be the result of pore blocking due to accumulation of the deposited IL close to the pore entrance. Consequently a zero N_2 adsorption capacity does not mean complete coverage of the pore surface by the IL. On the other hand, there is uncertainty on whether the observed in some cases gas uptake, is the result of adsorption in the interparticle voids or the pore voids or both.

Besides the cases of the Vycor modified with the silylated IL, the CPG modified with both kinds of IL and the SBA-15 modified with the silylated IL, where it is evident that the pore cores have remained open, for all the other samples it is unsafe to discriminate between the contribution of open pores and interparticle voids. Evidence for the above statements is provided by the LN_2 adsorption curve of a non-porous fumed silica (red line in Figure 47b) that converges with that of the MCM-41 (2.9 nm) sample modified with the non-functionalized IL.

Small-angle neutron scattering (SANS) was obtained for the impregnated with [bmim][PF6-] samples of ordered mesoporous silica MCM-41 and SBA-15. The results were in agreement with those of LN_2 absorption suggesting that the pores of SBA-15 are completely filled with IL where as a small fraction of the pore volume, the pore "core" of MCM-41 2.9 nm is empty.

a

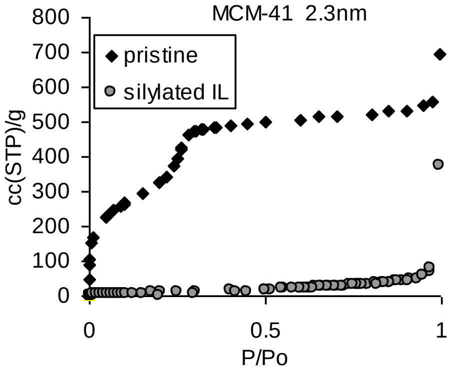

b

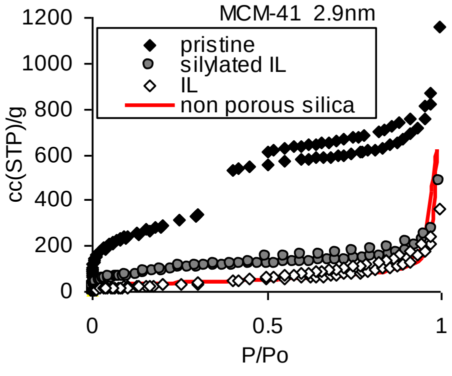

c

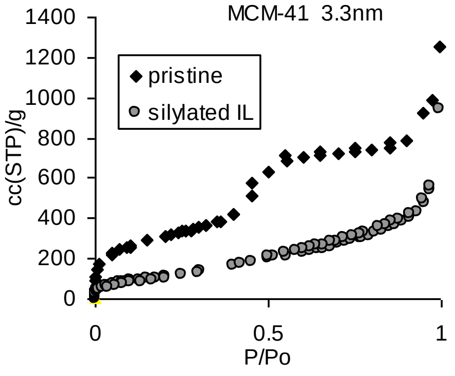

d

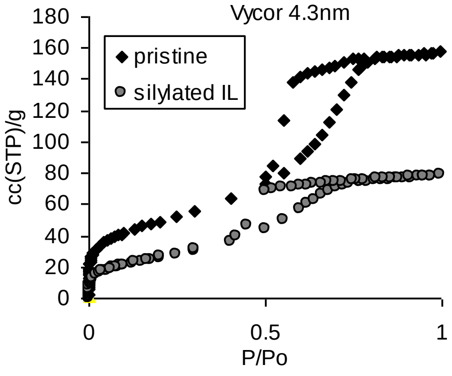

e

f

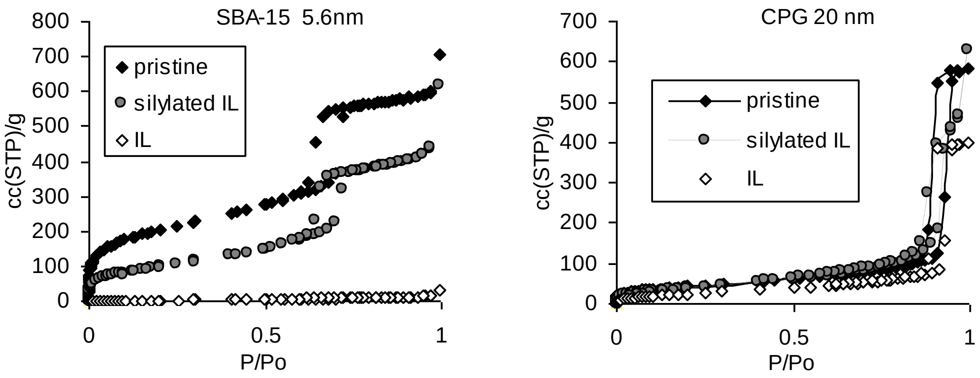

Figure 47. LN_2 porosimetry of the porous supports and the relevant SILPs

4.3.3 Structure formation in IL layers confined into pores

Due to the high loading of the IL phase, it was possible to monitor liquid crystalline ordering in the supported phase with typical analytical methods such as X-ray diffraction (XRD).

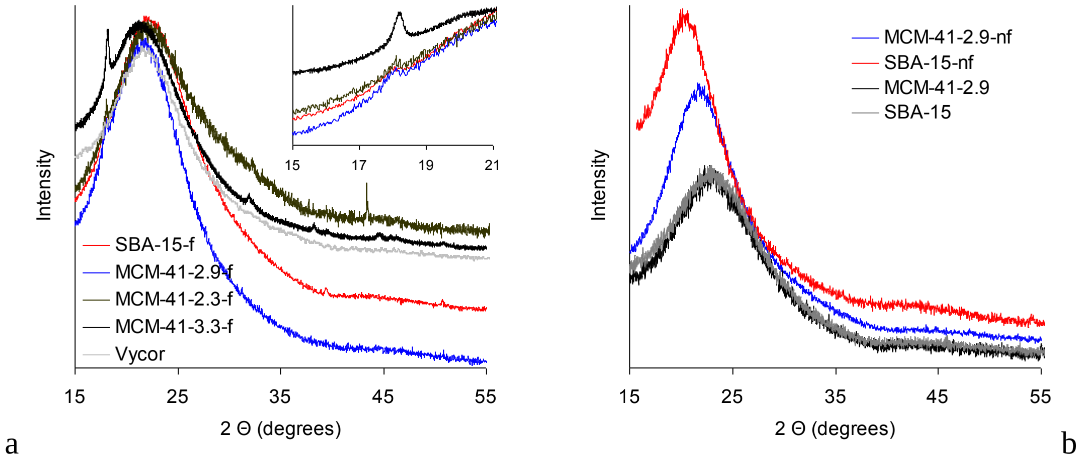

Figure 48. a) XRD spectra of SILPs developed with the functionalised IL, b) XRD spectra of the supports and relevant SILPs developed with the non-functionalised IL.

In all XRD spectra, the broad reflection located at about 22^o is due to silica. The SILPS developed with the functionalized IL (Figure 48a), exhibited a diffraction peak at around 18.2^o, a feature revealing ordering of the silylated IL molecules in the grafted layer. The only exception was the SILP developed using the Vycor$^®$ as the support. The reason was the low surface area of Vycor$^®$ compared to the SBA and MCM that led to moderate IL loading. The samples MCM-41-3.3-f and MCM-41-

2.3-f, presented the higher degree of ordering as indicated by their intense Bragg peak at 18.2° and the additional diffraction peaks appearing at $2\theta = 32.5, 38.5, 39.6, 43.5, 44.9, 46.3$, which should correspond to the different crystal planes of the silylated IL inside the pores. Comparing between the samples developed on several MCM-41 and SBA-15 supports, there is no evidence of a correlation between the intensity and number of their Bragg peaks and the pore structural characteristics such as the pore surface, size and volume. In this regard, we can conclude that ordering of the functionalized IL molecules in the grafted monolayer is a function of the density of the surface silanol groups, which however may differ even between portions of the same sample, depending on the thermal treatment and regeneration conditions. On the other hand, Bragg peaks had never been observed for the SILPs loaded with the non-functionalised IL (Figure 48b).

4.3.4 Orientation aspects

Oriented layering of the deposited IL phase is discussed in relation to CO_2 diffusivity at 35 °C only for the SILP samples which, as evidenced by the liquid nitrogen porosimetry and SANS analysis, underwent complete pore blockage upon IL deposition. The concept was to exclude the contribution of open porosity on the overall diffusion mechanism and focus on the characteristics of the IL phase.

We have chosen CO_2 as the probe gas molecule, since the system [bmim][$PF6^-$]/CO_2 is the most studied one and the mechanism of CO_2 absorption and diffusion in the bulk IL phase has already been elucidated by many research groups through absorption, molecular simulation and spectroscopic studies. Simulations indicate that CO_2 organizes strongly around the [$PF6^-$] anion in a “tangent-like” configuration that maximizes favourable interactions, but is more diffusely distributed around the imidazolium ring. Kazarian and co-workers investigated mixtures of CO_2 with [bmim][$PF6^-$] and [bmim][$BF4^-$] using ATR-IR spectroscopy. They found evidence of a weak Lewis acid-base interaction between the CO_2 and the anions of the ILs. In the case of a SILP system, CO_2 dissolves into the pores of immobilized ionic liquid through the IL/gas interface close to the mouth of the pores and becomes ionized through its interaction with the anions. The ionized species diffuse along the length of the pore by successive jumps between the anions of the deposited IL. As shown in the schematic of Figure 49, a possible orientation of the deposited IL phase with the anions towards the core of the pore (case A) may considerably enhance diffusivity when compared to a completely random orientation that leads to a random walk of the diffusing species between the anions (case B).

The use of a functionalised (silylated) IL, in our case the 1-(3-silylpropyl)-3-methylimidazolium hexafluorophosphate, which can be grafted on the surface of the support through covalent bonding between the alkoxy groups and the surface silanol groups, certainly enhances the possibility of a deposition orientation like the one presented in Figure 49 (case A).

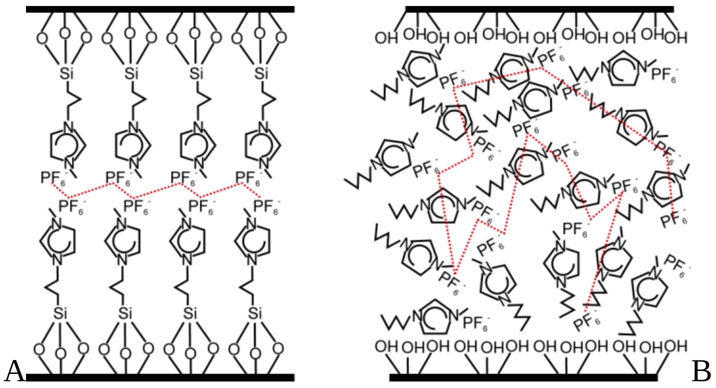

Figure 49. (A) Orientation of the silylated IL under confinement into the pores (B) Random accommodation into the pores of a non-functionalised IL.

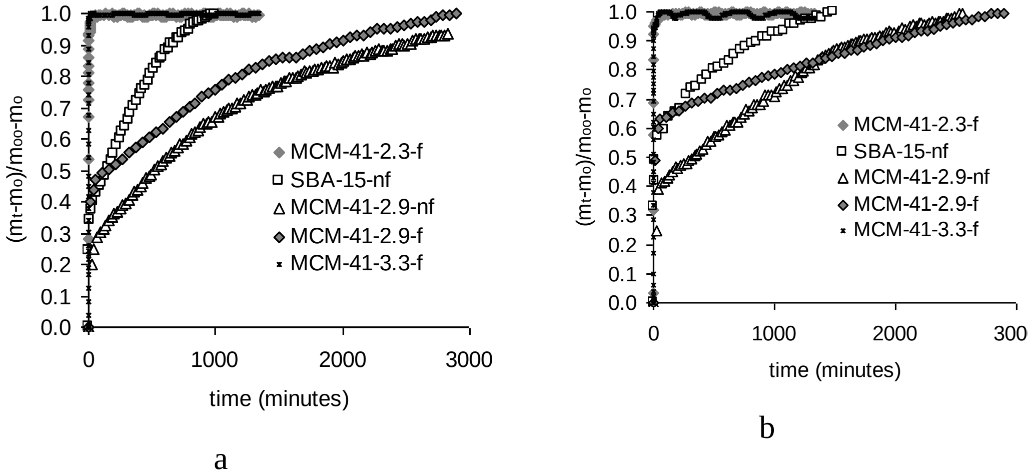

Figure 50. Transient curves of CO_2 adsorption of the several SILPs a) pressure step 0-250 mbar, b) pressure step 250-500 mbar.

The transient curves of CO_2 adsorption of two successive pressure steps (0-250 mbars, 250-500 mbars) presented in Figure 50 verify the proposed orientation. By fitting the kinetic results with the appropriate solution of the transient diffusion equation for spherical particles, it was possible to derive the diffusivity constants (D/r^2 (1/min) where r = the radius of sphere). The values of the highly ordered samples MCM-41-2.3-f and MCM-41-3.3-f were 100 to 600 times higher than those of the less ordered samples like MCM-41-2.9-f as well as of the non ordered at all samples such as the MCM-41-2.9-nf and SBA-15-nf.

It is interesting to note that correlation of the high CO_2 diffusivity with the degree of the IL layer ordering, also holds between the two most crystallized SILPs. Indeed the MCM-41-3.3-f sample, presenting a very intense Bragg peak at 18.2^o and a plurality of reflections of significant intensity (Figure 48a) exhibited a double diffusivity constant (D/r^2 = $0.057 min^{-1}$) compared to the MCM-41-2.3-f (D/r^2 = $0.026 min^{-1}$).

5 CONCLUSIONS

Hybrid materials of IL/Vycor® were prepared with the "grafting to" method. A method was developed based on the gravimetric technique in order to elucidate the extent of coverage on the modified material. SAXS and N_2 (77K) physisorption in conjunction with the aforementioned method provided important information on the morphology of the modified material. From this analysis, we concluded that the presence of water either in the solvent or on the material's surface plays a crucial role in the silanization process and the pore morphology of the hybrid material prepared after the SN2 type reaction with the imidazole. For samples prepared in toluene where residual water was present in the solvent, we observed the highest pore volume reduction in the hybrid material prepared while surface coverage of the silanol groups was only limited to 51% maximum. For samples prepared in dry $CHCl_3$ and thermally pretreated in high vacuum, the highest surface coverage obtained was 94% while the sample's pore volume was insignificantly affected: the combination of these findings suggests the formation of a monolayer of grafted silanes.

In view of the fact that CO_2 diffusion in the hybrid materials with open pores proceeds through a combined mechanism of diffusion in nanopores and dissolution/diffusion in the IL phase, a new methodology was developed in order to define the extent of the organic phase loading on the inorganic material.

SILP of MCM-41 2.3 nm revealed that excellent CO_2/CO separation capacity is obtained when pore is totally blocked by the ionic liquid phase. Moreover XRD analysis from the SILP sample developed in the MCM-41 support with 3.3 nm pore size revealed, for first time, the liquid crystalline phase transition of silylated IL at room temperature due to its confinement and orientation within the pores. Similarly, on the basis of DSC and XRD analysis, this phase transition also occurs, to a lesser extent, in the case of the confined IL developed on the MCM-41 with the smaller pore sizes (2.3 and 2.9 nm) as well as on the SBA-15 (8 nm). On the other hand, no evidence for crystallization was detected for the IL encapsulated into the pores of the Vycor sample. Signs of liquid crystalline phase ordering were not obtained for the samples prepared via the physical imbibition method. Liquid crystalline phase formation was attributed to the ordering induced by the parallel arrangement of the IL units grafted to the pore walls. The latter structural arrangement is also compatible with the transient CO_2 adsorption curves of the corresponding diffusivity measurements. Diffusivities for the grafted-derived SILPs were more than one order of magnitude larger than those obtained for the physically impregnated ones.

In addition, a novel pressure-assisted imbibition/reaction method was proposed for the chemical stabilization of silane functionalized imidazolium based ionic liquids into the pores of ceramic nanofiltration membranes. Stabilization is for the first time achieved via chemical bonding between the solid surface hydroxyls and the alkoxy group of the silane part of the functionalized ionic liquid molecule, rather than with the help of capillary forces and ionic interactions. The membranes exhibit high permeability (750 Barrer), considerable CO_2/CO separation capacity (25 at 80 ^oC) and excellent stability at temperatures up to 250 ^oC. The method was proved efficient and reproducible in the case of membranes with 1 nm pore size and ionic liquids functionalized with the chloromethyltrimethoxysilane.

6. FUTURE PROSPECTS – FURTHER RESEARCH

- Grafting of separation specific ionic liquids on the pore surface of nanoporous membranes, exploiting the stronger interaction of these ILs with CO_2. Possible synthetic routes and IL molecules are presented in Figure 51.

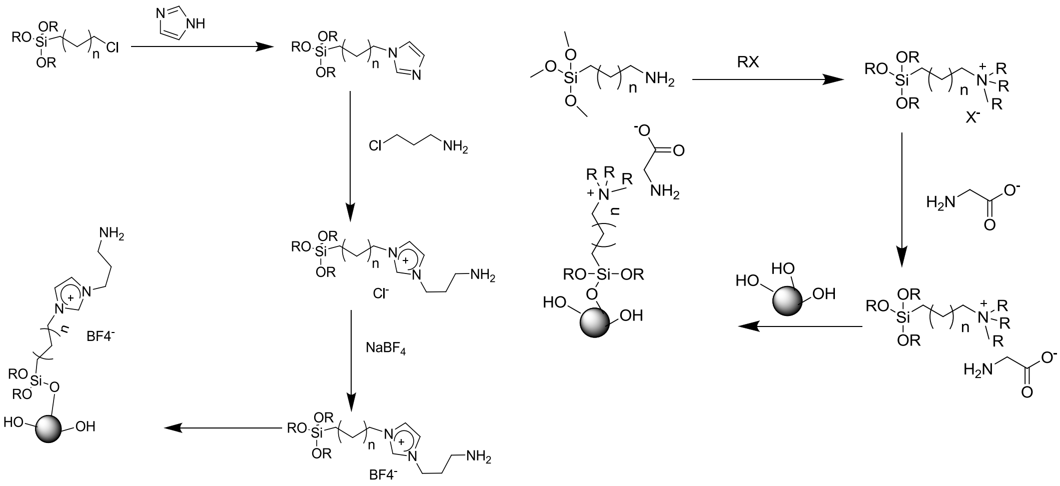

a b

Figure 51. Possible chemical reaction routes for grafting amino functionalized ILs on the silica surface

Figure 51a describes the synthesis of an alkyl amine functionalized imidazolium based IL which can be further grafted on the pore surface. Figure 51b describes the synthesis of an alkyl ammonium functionalized IL where the halide anion can be exchanged with amino acids. This silylated ammonium based–amino acid IL can be further grafted to the pore surface of the membranes.

- Improve the performance characteristics of the membranes by confining the grafting of ILs solely into the pores of the nanofiltration layer of the membrane. The permeability-selectivity performances reported in the present work (750 Barrer, CO_2/CO 25), are still far from those defined by recent Robenson plots (Figure 52), concerning the performance of CO_2 separating membranes.

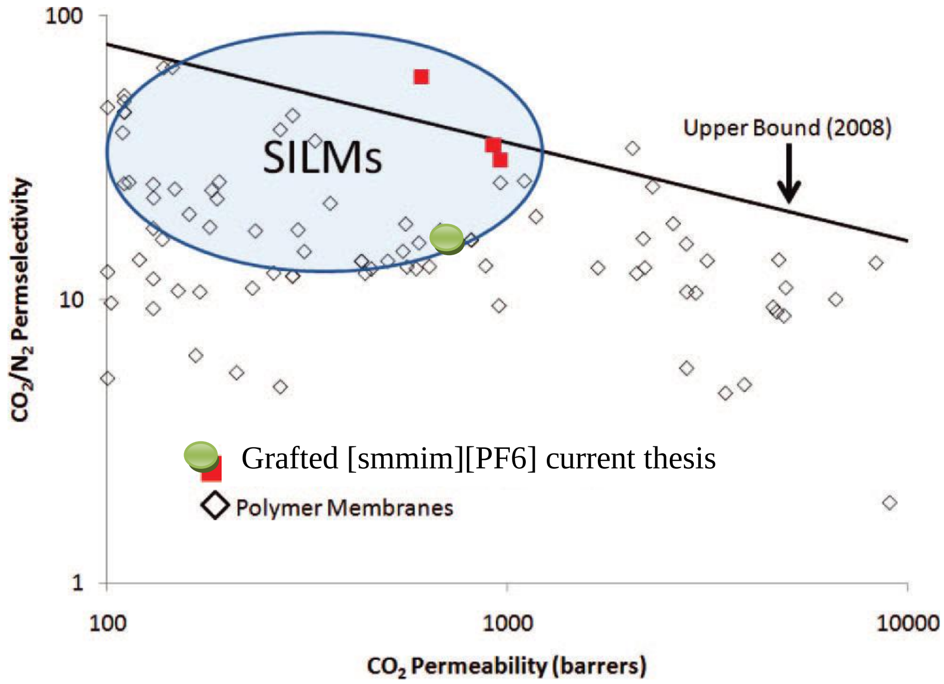

Figure 52. “Robenson Plot” for CO_2/N_2 annotated to include SILM data

- Trying to reduce the cost of the membrane separation process by involving cheaper supports e.g. carbon fibers instead of ceramics (Silica, Alumina). In this case, surface modification of the carbon membranes will be necessary to graft the silylated Ionic Liquids (Figure 53).

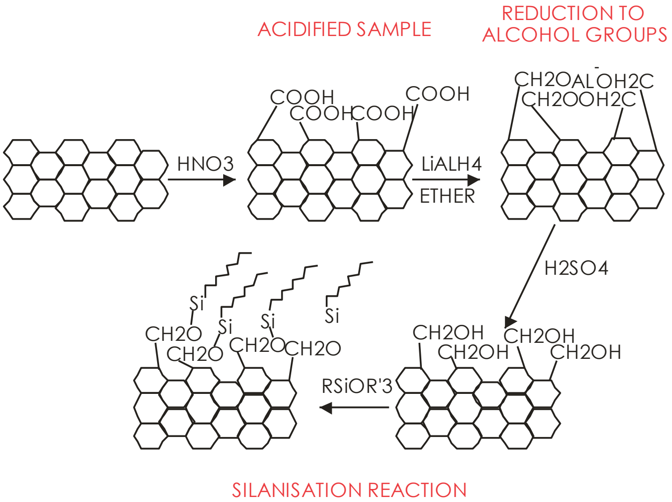

Figure 53. Modification steps for the development of IL/carbon fibers

7 REFERENCES

1. Ionic Liquids Database Merck, Ionic Liquids: New Materials for New Applications, http://ildb.merck.de/ionicliquids/en/startpage.htm
2. Walden, P. *Bull. Acad. Sci.* **1914**, 405-422.
3. Gale, R. J. *et. al. Inorg. Chem.* **1978**, *17*, 2728-2729.
4. Wilkes, J. S. *et. al. Inorg. Chem.* **1982**, *21*, 1263-1264.
5. Boon, J. A. *et. al. J. Org. Chem.* **1986**, *51*, 480-483.
6. Wilkes, J. S. *et. al. Chem. Commun.* **1992**, 965-967.
7. Earle, M. J. *et. al. Pure Appl. Chem.* **2000**, *72*, 1391-1398.
8. Earle, M. J. *et. al. Nature* **2006**, *439*, 831-834.
9. Buzzeo, M. C. *et. al. Chem. Phys. Chem.* **2004**, *5*, 1106-1120.
10. Olivier-Bourbigou, H. *et. al. J. Mol. Cat.* A **2002**, 419-437.
11. Welton, T. *Coord. Chem. Rev.* **2004**, *248*, 2459-2477.
12. Hagiwara, R. *et. al. J. Fluorine Chem.* **2000**,*105*, 221-227.
13. Bellina, F. *et. al. Molecules* **2010**, *15*, 2211-2245.
14. Sheldon, R.A. *et. al. Green Chem.* **2002**, *4*, 147-151.
15. Jain, N. *et. al. Tetrahedron* **2005**, *61*, 1015-1060.
16. Muzart, J. *Adv. Synth. Catal.* **2006**, *348*, 275-295.
17. Quijano, G. *et. al. Bioresource Technol.* **2010**, *101*, 8923–8930.
18. Larachi, F. *et. al. Chem. Eng. Process.* **2010**, *49*, 313–322.
19. Hou, Y. *et. al. Ind. Eng. Chem. Res.* **2007**, *46*, 8166–8175.
20. Peters, C. J. *et. al. Fluid Phase Equilib.* **2007**, *260*, 19–22.
21. Haan, A. B. *et. al. Chem. Eng. Res. Des.* **2007**, *85*, 31–39.
22. Kumełan, J. *et. al. J. Chem. Eng. Data* **2010**, *55*, 165–172.
23. Condemarin, R. *et. al. Chem. Eng .J.* **2009**, *147*, 51–57.
24. a) Heintz, Y.J. *et. al. Energ. Fuel.* **2009**, *23*, 4822–4830. b) Goodrich B. F. *et. al. Ind. Eng. Chem. Res.* **2011**, *50*, 111–118.
25. Baltus, R. E. *et. al. Sep. Sci. Technol.* **2005**, *40*, 525–541.
26. Lee, S. H. *et. al. Desalination* **2006**, *200*, 21–22.
27. Park, Y. I. *et. al. Desalination* **2009**, *236*, 342–348.
28. Tang, J. *et. al. J. Polym. Sci. Polym. Chem.* **2005**, *43*, 5477–5489.
29. Simons K. *et. al. J..Membr. Sci.* **2010**, *360*, 202–209.
30. Koros W. J. *et. al. Ind. Eng. Chem. Res.* **2002**, *41*, 6139-6148.

31. Long J. R. *et. al. Angew. Chem. Int. Ed.* **2010**, *49*, 6058–6082.

32. Feng, B. *et. al. Energ. Fuel.* **2007**, *21*, 426-430.

33. Jones C. W. *et. al. ChemSusChem* **2009**, *2,* 796-799.

34. Poston, J. A. *et. al. Energ. Fuel.* **2001**, *15*, 279-283.

35. Yang, R.T *et. al. Ind. Eng. Chem. Res.* **1995**, *34*, 591-594.

36. Zhang, S. *et. al. J. Chem. Eng. Data* **2005**, *50*, 1582-1586.

37. Shiflett, M. B. *et. al. Ind. Eng. Chem. Res.* **2005**, *44*, 4453-4459.

38. Kuhne, E. *et. al. J. Supercrit. Fluids* **2008**, *45*, 27-31.

39. Kim, Y. S. *et. al. Fluid Phase Equilibr.* **2005**, *228–229*, 439-442.

40. Kresge, C. T. *et. al. Nature* **1992**, *359*, 710-713.

41. Monnier, A. *et. al. Science* **1993**, *261*, 1299-1302.

42. Beck, J. S. *et. al. J. Am. Chem. Soc.* **1992**, *114*, 834-838.

43. Gusev V. *et. al. J. Phys. Chem.* **1996**, *100,* 1985-1989.

44. Kruk, M. *et. al. Chem. Mater.* **2000**, *12,* 1961-1968.

45. Liu, W. *et. al. Mater. Chem. Phys.*, **2008,** *109*, 257-261.

46. S. Lowell, J. B. Shields, *Powder surface area and porosity,* 3rd edition, Chapman and Hall, London, **1992**, 72-76

47. Blanchard, L. A. *et. al. J. Phys. Chem. B* **2001**, *105,* 2437-2444.

48. Anthony, J. L. *et. al. J. Phys. Chem. B* **2002**, *106*, 7315-7320.

49. Kamps, A. *et. al. J. Chem. Eng. Data* **2003**, *48*, 746-749.

50. Husson-Borg, P. *et. al. J. Chem. Eng. Data* **2003**, *48*, 480-485.

51. Brennecke J. F. *et. al. J. Am. Chem. Soc.* **2004**, *126*, 5300–5308.

52. Kazarian S. G. *et. al. Chem. Commun.* **2000**, 2047–2048.

53. Bhargava, B. L. *et. al. J. Phys. Chem. B* **2007**, *111*, 4477-4487.

54. Brennecke, J. F. *et. al. J. Am. Chem. Soc.* **2004**, *126,* 5300-5308.

55. Bates, E. D. *et. al. J. Am. Chem. Soc.* **2002**, *124*, 926–927.

56. Brennecke J. F. *et. al. J. Am. Chem. Soc.* **2010**, *132*, 2116–2117.

57. Holik, M. *et. al. J. Chromatogr.* **1981**, *213*, 33-37.

58. Landmesser, H. *et. al. Solid State lonics* **1997**, *101-103*, 271-274.

59. Benjelloun, M. *et. al. Phys. Chem. Chem. Phys.* **2001**, *3*, 127-131.

60. Kocherbitov, V. *et. al. J. Phys. Chem. C* **2007**, *111*, 12906-12909.

61. Großmann, F. *et. al. J. Chromatogr. A*, **2001**, *910*, 223-227.

62. Kumar, D. *et. al. Colloid. Surface. A* **2001**, *187*, 109-113.

63. Brennecke J. F. *et. al. J. Phys. Chem. B* **2004**, *108*, 20355-20359.

64. Janowski, F. *et. al. Porose Glaser*, VEB Deutscher Verlag fur Grundstoffindustrie, Leipzig, **1982**.

65. Ying Z. *et. al. Phys. Rev. B* **2004**, *69,* 33404-33409.

66. Mitropoulos, A. *et. al. J. Colloid Interf. Sci.* **1997**, *193,* 137-141.

67. Romanos G. *et. al. J. Colloid Interf. Sci.* **1998**, *206,* 605–606.

68. Beltsios, K. *et. al. J. Porous Mater.* **1999**, *6,* 25–31.

69. Bale, H. D. *et. al. Phys. Rev. Lett.* **1984**, *53,* 596-601.

70. Mitropoulos, A. C. *et. al. Phys. Rev. B* **1995**, *52*, 10035-10039.

71. Schaefer, D. S. *et. al. Phys. Rev.Lett.* **1987**, *58*, 284-289.

72. Wiltzius, P. *et. al. Phys. Rev. A* **1987**, *36*, 2991-2995.

73. Höhr, A. *et. al. Phys. Rev. B* **1988**, *38,* 1462-1667.

74. Levitz, P. *et. al. J. Chem. Phys.* **1991**, *95,* 6151-6155.

75. Ross, D. K. *et. al. Phys. Rev. B* **1994**, *49*, 5911-5914.

76. Brennecke, J. F. *et. al. J. Phys. Chem. B* **2002**, *106*, 7315-7320.

77. J. Karger and D. M. Ruthven, *Diffusion in Zeolites and Other Microporous Solids,* A Wiley Interscience Publication, New York, **1991**, pp. 239-243.

78. Grimmett, M. R. *et. al. Aust. J. Chem.* **1977**, *30,* 2005-2013.

79. Ohtani, H. *et. al. Anal. Sci.* **2008**, *24,* 1335-1340.

80. Choudhury, A. R. *et. al. J. Am. Chem. Soc.* **2005**, *127*, 16792-16796.

81. Xu, W. *et. al. J. Phys. Chem. B* **2003**, *107*, 11749-11753.

82. Brennecke, J. F. *et. al. J. Phys. Chem. B* **2002**, *106*, 7315-7319.

83. Brennecke, J. F. *et. al. J. Am. Chem. Soc.* **2004**, *126*, 5300-5304.

84. Yuhuan C. *et. al. Thermochim. Acta* **2006**, *441*, 42-46.

85. Brennecke J. F. *et. al. J. Phys. Chem. B* **2004**, *108*, 20355-20359.

86. Kumelan, J. *et. al. Fluid Phase Equilibr.* **2005**, *228- 229*, 207-213.

87. Jacquemin, J. *et. al. Fluid Phase Equilibr.* **2006**, *240*, 87-91.

88. Chen, S. *et. al. J. Am. Chem. Soc.* **2007**, *129*, 2416-2419.

89. Brennecke, J. F. *et. al. J. Phys. Chem. B* **2002**, *106,* 7315-7320.

90. Maginn, E. J. *et. al. J. Am. Chem. Soc.* **2004**, *126,* 5300-5308.

91. Yuhuan C. *et. al. Thermochim. Acta* **2006**, *441,* 42-44.

92. Brennecke, J. F. *et. al. J. Phys. Chem. B* **2004**, *108,* 20355-20365.

93. Kumelan, J. *et. al. Fluid Phase Equilibr.* **2005**, *228-229*, 207-211.

94. Jacquemin, J. *et. al. Fluid Phase Equilibr.* **2006**, *240*, 87-95.

95. W. R. Vieth, *Diffusion In and Through Polymers*, Principles and Applications, Hansen Publishers, Munich, **1991**.

96. Hou Y. *et. al. Ind. Eng. Chem. Res*. **2007**, *46*, 8166–8175.

97. Scovazzo, P. *et. al. J. Membr. Sci.* **2009**, *327*, 41–48.

98. Kapteijn, F. *et. al. J. Membr. Sci.* **1998**, *144*, 87-104.

99. Romanos, G. E. *et. al. Micropor. Mesopor. Mat.* . **2008**, *110*, 11–24.

100. Ohlin, C. A. *et. al. Chem.Commun.* **2004**, 1070–1071.

101. Maginn, E. J. *et. al. J. Am. Chem. Soc.* **2004**, *126*, 5300-5308.

102. Zhao, X. S. *et. al. J. Phys. Chem. B* **1997**, *101*, 6525–6531.

103. Widenmeyer M. *et. al. Chem. Mater.* **2002**, 14, 1827-1831.

104. Nozaki, C. *et. al. J. Am. Chem. Soc.* **2002**, *124*, 13194-13203.

105. Zhuravlev, L. T. *Langmuir* **1987**, *3*, 316-318.

106. Vangeli, O. C. *et. al. J. Phys. Chem. B* **2010**, *114*, 6480–6491.